COMBUSTION HEAT RELEASE EFFECTS ON ASYMMETRIC VORTEX SHEDDING FROM BLUFF BODIES

A Dissertation
Presented to
The Academic Faculty

by

Caleb Nathaniel Cross

In Partial Fulfillment
of the Requirements for the Degree
Doctor of Philosophy in
Mechanical Engineering

Georgia Institute of Technology
December 2011

COMBUSTION HEAT RELEASE EFFECTS ON ASYMMETRIC VORTEX SHEDDING FROM BLUFF BODIES

Approved by:

Dr. Ben T. Zinn, Advisor
School of Aerospace Engineering
Georgia Institute of Technology

Dr. Jerry Seitzman
School of Aerospace Engineering
Georgia Institute of Technology

Dr. Timothy Lieuwen
School of Aerospace Engineering
Georgia Institute of Technology

Dr. Eugene Lubarsky
School of Aerospace Engineering
Georgia Institute of Technology

Dr. Marc Smith
School of Mechanical Engineering
Georgia Institute of Technology

Date Approved: August 24, 2011

To my loving wife, Amely

Not to us, O Lord, not to us,
but to your name goes all the glory
for your unfailing love and faithfulness.
Psalm 115:1 (NLT)

ACKNOWLEDGEMENTS

I would like to express my deepest gratitude to my advisor, Dr. Ben T. Zinn, for his invaluable guidance throughout the course of my graduate studies. I owe Dr. Eugene Lubarsky many thanks, as well, for his mentoring during the last five years. I would also like to thank the other members of my thesis reading committee for their many helpful comments and willingness to evaluate this research: Dr. Timothy Lieuwen, Dr. Jerry Seitzman, and Dr. Marc Smith.

This thesis would not have been possible without the help of others at the Ben T. Zinn Combustion Laboratory. I would especially like to thank Dmitriy Shcherbik and Oleksandr Bibik for their technical expertise, patience and willingness to help. I thank all of the graduate students at the lab for their help and encouragement. Notably, I thank Aimee Williams, Alex Klusmeyer, Keary Bonner and John Cutright who provided invaluable assistance at various times during the course of this research. Thanks are also due to Ben Emerson, Charlie Tyndall, Jacqueline O'Connor, Bobby Noble, David Scarborough, Yogish Gopala, Matt Quinlain, Jim Cornacchio, Ben Wilde, Shai Birmaher, Yedidia Neumeier, Jon Reichel, Jack Crawford, Chris Foley, Andrew Marshall, Prabhakar Venkateswaran and Dmitriy Plaks for their help, encouragement and many enlightening conversations.

I wish to thank Dr. Suresh Menon and Andy Smith from the Computational Combustion Laboratory for providing the LES data to compare to the experimental results of this study. I would also like to thank Glenda Duncan and Cathy Valero for providing assistance with many tasks over the years and for their kindness.

Many thanks are due to Dr. Larry Banta from West Virginia University and Dr. Christopher Johnson from the U.S. Department of Energy's National Energy Technology Laboratory (NETL) for their mentorship during my undergraduate years and their encouragement to attend Georgia Tech for graduate school. I would also like to thank Chad Schaeffer and Rich Pineault, as well, for their help and friendship during my time at WVU and NETL.

This research was funded, in part, by Pratt & Whitney. I thank Dr. Jeffery Lovett, Dr. Ben Bellows, and Karen Teerlinck for their technical guidance and interest in this research. I would also like to thank Creare Inc., especially Dr. Darin Knaus and Dr. Scott Phillips, for allowing the use of the high-speed camera used in this study.

Finally, I thank my friends and family for all of their love, support, and encouragement during my time at Georgia Tech. I especially thank my mother, father and brother for always being there for me. Most importantly, I thank my wife, Amely, for her endless patience, unfailing love, and wonderful sense of humor. Without her encouragement I would not have completed this journey.

TABLE OF CONTENTS

LIST OF TABLES

LIST OF FIGURES

Page

NOMENCLATURE

Symbols

C_p	Specific Heat of a Fluid [J/kg-K]
E	Total Energy of a Fluid [J]
f	Frequency of oscillations [Hz]
h	Transverse displacement of vortex sheet [non-dimensional]
k	Complex wave number [non-dimensional]
k^0	Absolute wave number [non-dimensional]
$\dot{m}$	mass flow rate [kg/s]
MW	Molecular weight [kmol/kg]
O_2%	Oxygen concentration by volume (expressed as a percentage)
p	Static pressure [non-dimensional]
P	Experimentally measured static pressure [psia]
$p`$	Dynamic pressure [non-dimensional]
$P`_i$	Dynamic pressure transducer ("i" indicates measurement location)
p_o	Stagnation pressure [non-dimensional]
Pr	Prandtl number
$Q`/Q_{mean}$	Measured oscillatory heat release normalized by mean value
Re	Reynolds Number
R_u	Universal Gas Constant [kJ/kmol-K]
S	Density ratio between products and reactants streams [non-dimensional]
St	Strouhal Number
t	Time [s or μs, where specified]
T	Temperature [°C or K, where specified]
u	Normalized axial velocity [non-dimensional]

$\vec{u}$	Velocity vector [m/s]
U	Axial velocity [m/s]
u_i	Component of velocity vector ("i" denotes tensor index)
v	Normalized transverse velocity [non-dimensional]
V	Velocity magnitude [m/s]
W	Width of bluff body [m or cm, where specified]
x	Axial distance from bluff body trailing edge [m or mm, where specified]
y	Transverse distance from combustor centerline [dimensions as specified]
y	Transverse distance from combustor centerline [non-dimensional]
δ_{ij}	Dirac Delta function
ζ_i	Flame edge location [cm]
κ	Thermal conductivity [non-dimensional]
λ	Wavelength [nm]
μ	Fluid viscosity [non-dimensional]
ρ	Gas density [kg/m^3]
ρ	Gas density [non-dimensional]
τ	Characteristic time interval [ms]
Φ	Equivalence Ratio = $\frac{\text{measured fuel-air ratio}}{\text{stoichiometric fuel-air ratio}}$ [non-dimensional]
ϕ	Velocity potential [non-dimensional]
ω	Complex frequency [non-dimensional]
ω^0_i	Absolute growth rate [non-dimensional]
$\vec{\omega}$	Vorticity vector [1/s]

Abbreviations

a.u.	Arbitrary units

BVK	Bénard-von Kármán
DFT	Discrete Fourier Transform
FFT	Fast Fourier Transform
LES	Large Eddy Simulation
PMT	Photomultiplier tube

Subscripts

air, tot	Total air flow: pre-burner exhaust plus diluting air
b	Burned (products) gases
D	Bluff body diameter
global	Global flow parameter
in	Inlet flow parameter
L	Lower flame edge
local	Local flow parameter
u	Unburned (reactants) gases
U	Upper flame edge
∞	Free-stream flow parameter

Superscripts and Overscore

`	Oscillatory flow parameter
–	Time-averaged or average flow parameter
→	Denotes a vector quantity

SUMMARY

This thesis describes an investigation of oscillatory combustion processes due to vortex shedding from bluff body flame holders. The primary objective of this study was to elucidate the influence of combustion process heat release upon the Bénard-von Kármán (BVK) instability in reacting bluff body wakes. For this purpose, spatial and temporal heat release distributions in bluff body-stabilized combustion of liquid Jet-A fuel with high-temperature, vitiated air were characterized over a wide range of operating conditions. Two methods of fuel injection were investigated. In the first method, referred to as close-coupled fuel injection, the fuel was supplied via discrete liquid jets injected perpendicular to the cross-flowing air stream just upstream of the bluff body trailing edge, thereby limiting fuel and air mixing prior to burning. The fuel was introduced well upstream (~0.5 m) of the bluff body in the second fuel injection mode, resulting in a well-evaporated and mixed reactants stream. The resulting BVK heat release dynamics were compared between these fuel injection modes in order to investigate their dependence upon the spatial distributions of fuel-air ratio and heat release in the reacting wake.

When close-coupled fuel injection was used, the BVK heat release dynamics increased in amplitude with increasing global equivalence ratio, reaching a maximum just before globally rich blow out of the combustion process occurred. This was due to a decrease in fuel entrainment into the near-wake as the fuel spray penetrated further into the cross-flow, which reduced the local heat release and equivalence ratio (indicated by CH* and C_2*/CH* chemiluminescence, respectively). As a result, the density gradient

across the near-wake reaction zone decreased, resulting in less damping of vorticity due to dilatation. In addition, unburned reactants were entrained into the recirculation zone due to the injection of discrete liquid fuel jets in close proximity to the wake. This reduced the temperature of the recirculating gases further, resulting in large (i.e., near-unity) products-to-reactants density ratios in the near-wake.

When the fuel was introduced upstream of the bluff body, the BVK heat release dynamics significantly decreased in amplitude. In this case the fuel was, in all likelihood, fully evaporated and well-mixed with the air prior to burning, resulting in greater amounts of fuel entrainment and subsequent heat release in the near-wake than in the close-coupled fuel injection case. In addition, the heat release was distributed more uniformly across the combustor span, which led to stronger density gradients across the near-wake reaction zone than in close-coupled-fuelled flames due to a lack of reactants entrainment into the recirculation zone. This enhanced the damping of vorticity due to dilatation, which inhibited the formation and shedding of the large-scale, coherent vortices. When the local density gradient was large enough, the BVK instability was completely suppressed.

A parallel, linear stability analysis was performed in order to further understand the influence of the near-wake combustion process heat release upon the wake instability characteristics. The results of this analysis indicate that the products-to-reactants density and velocity ratios in the near-wake are the primary parameters controlling the onset of local absolute instability (a necessary condition for the global, BVK instability) in reacting wakes. Upon comparing these results to the measured data, absolute instability was predicted for all operating conditions in which relatively high-amplitude BVK heat

release dynamics were observed. This was the case for close-coupled fuel injection at all global equivalence ratios, as well as upstream fuel injection at lean equivalence ratios, due to the low temperature rise across the reacting shear layers in these cases. Only upstream fuel injection at near stoichiometric fuel-air ratios resulted in local products-to-reactants density ratios low enough to suppress absolute instability and, thus, BVK vortex shedding.

The results of this study support the postulate that sinuous heat release fluctuations due to BVK vortex shedding are the result of local absolute instability in the near-wake, which is eliminated only if the temperature rise across the reacting shear layers is sufficiently high. Furthermore, this thesis demonstrates that non-uniform fuelling of the near-wake reaction zone increases the likelihood of absolute instability due to the possibility of near-unity products-to-reactants density ratios locally, as was the case for close-coupled fuel injection at high global equivalence ratios. In fact, high-amplitude BVK heat release dynamics were observed in close-coupled-fuelled flames at global operating conditions in which premixed flames were stable. Therefore, knowledge of the local thermal-fluid properties in the near-wake reaction zone is necessary to predict the onset of the absolutely unstable, BVK mode in reacting bluff body wakes. This is particularly true of partially-premixed and liquid-fuelled systems, in which spatial variations in fuel-air ratio and heat release are likely.

CHAPTER 1

INTRODUCTION

1.1 Motivation

This thesis describes an investigation of bluff body-stabilized combustion dynamics due to Bénard-von Kármán (BVK) vortex shedding. Bluff bodies have been extensively used to stabilize high-speed reacting flows due to their ability to produce stable, efficient and low pressure loss combustion over wide ranges of operating conditions (e.g., pressures and inlet velocities) and system scales [1-5]. Common applications include propulsion systems, such as gas turbine engine thrust augmentors and ramjet engines, and supplementary burning in stationary power generation systems and industrial boilers. The relative simplicity, low cost and light weight of bluff body flame holders make them an appealing method of flame stabilization in such systems.

Despite their advantages, bluff body-stabilized combustion processes are inherently unsteady. Flow separation from the bluff body produces an unsteady wake containing a wide range of vortical length scales from fine-scale turbulent structures to large-scale coherent vortices. The interactions between these vortical structures and combustion processes have been linked to the onset of combustion instabilities, which is the occurrence of large-amplitude pressure oscillations in the combustion chamber created by the feedback between a natural acoustic mode and an oscillatory combustion process [6-9]. Coherent vortex structures can distort a flame and cause its surface area to oscillate, thereby producing unsteady heat release which can add energy to a natural acoustic mode if the heat release and pressure oscillations are in phase [10]. The impingement of convected vortices on chamber walls and exit nozzles can excite acoustic waves which propagate back to the reaction zone and perturb the flame, causing heat release fluctuations [10-11]. These vortex-wall interactions can also lead to breakdown

of the coherent structure to fine-scale turbulence, which can result in sudden heat release [7].

In addition to driving combustion instabilities, coherent vortical structures can adversely affect the static stability of the combustion process. The presence of large-scale vortices can inhibit molecular mixing necessary to initiate combustion, though it can be advantageous to bulk mixing of fuel and oxidizer streams when they are introduced separately [7]. Fluctuations in velocity and flow curvature due to vortex shedding can cause excessive fluid mechanic strain which, if it exceeds the extinction strain rate of the combustion process, can cause the flame to extinguish (or blow off) [12-14]. In the case of bluff body-stabilized combustion processes, researchers have shown BVK vortex shedding to be a precursor and possible contributor to flame blow off [12-15].

These acoustic-flame-vortex interactions are complex, which contributes to a lack of proper understanding of the fundamental fluid mechanic and chemical processes controlling bluff body-stabilized combustion. An improved understanding of these interactions is critical, as it may prevent the onset of such detrimental effects as flame flashback or blow off, increased heat transfer to the system walls and large-amplitude structural vibrations in practical combustion systems [6, 10].

1.2 Background

1.2.1 Dynamics of Non-Reacting Bluff Body Flow

Figure 1.1 depicts two-dimensional, isothermal flow around a bluff body [12], illustrating four key regions: boundary layers, separated shear layers, the recirculation zone, and the wake. Boundary layers form on the bluff body surface and persist until the flow separates from the bluff body. Shear layers form downstream of the flow separation points, which are characterized by strong velocity gradients in the transverse direction

and, consequently, high-magnitude vorticity. As shown in Figure 1.1, the shear layers enclose the recirculation zone and separate it from the free-stream flow. The recirculation zone is a region of fluid just downstream of the bluff body in which the time-averaged axial velocity is reversed, the length of which depends upon various properties of the flow (such as Reynolds number and turbulence intensities) and bluff body geometry. The recirculation zone ends at the axial location in which the shear layers merge, and where a time-averaged stagnation point exists. Beyond this point, a wake flow develops, with the mean axial velocity at all transverse locations having the same direction (or sign). This wake flow persists throughout the remainder of the flow field.

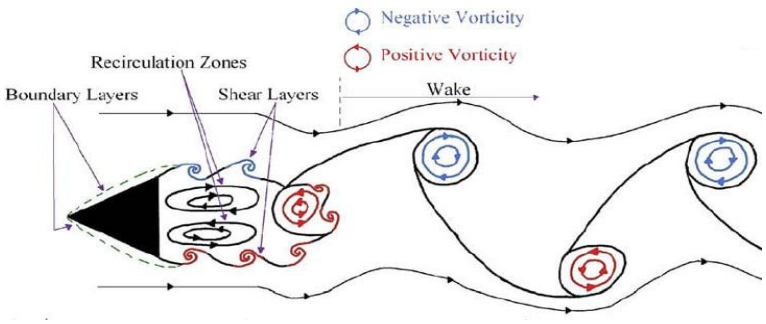

Figure 1.1: Fluid mechanics of isothermal bluff body flow, showing Bénard-von Kármán vortex shedding (reproduced with permission from [12]).

Each of the characteristic flow regions described above experience a variety of hydrodynamic instabilities. For high Reynolds number flow (i.e., Re > 1000), the separated shear layers experience a Kelvin-Helmholtz instability, which manifests itself in the form of coherent vortices that roll up and are shed simultaneously (symmetrically) from each side of the bluff body, as shown in Figure 1.1. Beyond a critical Reynolds number (approximately 50 for a cylinder) the wake is dominated by the BVK instability. When this instability occurs, large-scale, coherent vortices of opposite sign are shed alternately from either side of the bluff body, creating the sinuous wake depicted in

Figure 1.1. The BVK vortices shed at a frequency that is proportional to the inlet velocity and inversely proportional to the bluff body width. This frequency is usually represented as a non-dimensional Strouhal number of the form:

$$St = \frac{fD}{U} \tag{1.1}$$

where f is the instability frequency, U is the approach velocity, and D is the bluff body diameter. The Strouhal number at which the BVK instability occurs varies with Reynolds number and is dependent upon bluff body geometry, with typical values ranging between 0.20 and 0.29. For flow around a cylinder, the Strouhal number is nearly constant, St~0.21, in the Reynolds number range $1000 < Re_D < 100{,}000$ [12].

The alternately shed von Kármán vortices are formed by the interaction between the two separated shear layers of oppositely-signed vorticity [16-20], as illustrated in the dye traces of Figure 1.2 (reproduced from [16]). According to Gerrard, vortex shedding occurs when circulation in one shear layer is of sufficient magnitude that it pulls fluid from the other side, producing a growing vortex which ultimately sheds when its supply is "cut-off" by the fluid it is pulling [17]. This shear layer interaction must take place over some critical distance downstream of the bluff body (Gerrard's formation length). Thus, most methods for suppressing vortex shedding ultimately prevent this interaction over the formation length; e.g., by inserting a splitter plate that is two bluff body widths long into the wake [20].

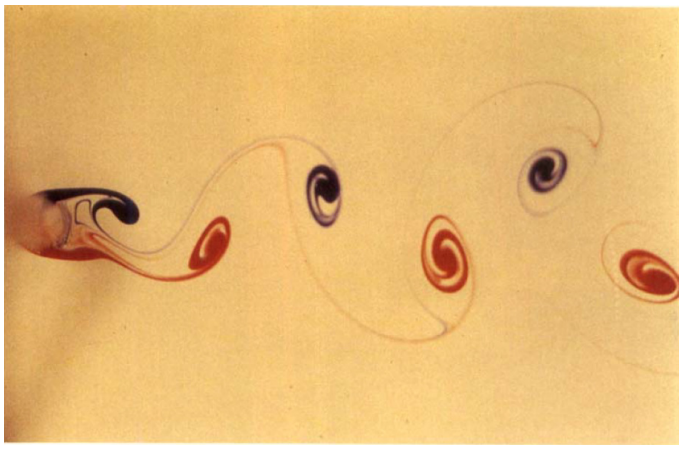

Figure 1.2: Dye traces in the wake of a cylinder at Re_D=80, with red and blue dye corresponding to positive and negative vorticity, respectively (reproduced with permission from Ref. [16]).

Recent studies have linked the onset of the BVK instability, which is a global oscillation of the wake, to the occurrence of local instabilities in the near-wake. Before proceeding with a more detailed explanation of this process, a brief description of the two general classifications of linear hydrodynamic instability, convective and absolute, is necessary. Following Huerre and Monkewitz [21], the stability characteristics of the flow are determined by its behavior following an infinitesimal impulse at a particular time and location. If the flow is unstable, this disturbance will be amplified. If the amplified disturbance is convected away from the location of the impulse and ultimately leaves the entire flow field undisturbed, the flow is convectively unstable. If, however, the amplified disturbance spreads upstream and downstream (even though the fluid particles are convected out of the system), the flow is absolutely unstable. In absolutely unstable flows, the perturbations grow in amplitude at a fixed location, and the entire flow field eventually becomes disturbed.

Convective instabilities are not self-excited but require continuous excitation to persist [21]. In practical situations, broadband turbulence and/or acoustic waves provide the continuous excitation source needed for convectively unstable shear flows to remain

disturbed. Due to their sensitivity to low levels of forcing, various scales of natural white noise are differentially amplified in convectively unstable flows, and their velocity spectra exhibit a relatively broad response distributed around the preferred frequency of excitation [23]. In contrast, absolute instabilities are self-excited, growing in amplitude until limit cycle saturation occurs. Absolutely unstable flows do not respond to low-level external forcing, therefore their spectra display a narrowband response at the natural frequency, with amplitudes typically several orders of magnitude above the background noise [18].

Both convective and absolute instabilities occur in bluff body flows. The Kelvin-Helmholtz instability in the separated shear layers is convectively unstable, as these disturbances are convected downstream with the flow and the shear layers respond to external forcing [23]. On the other hand, the onset of the BVK instability has been linked to local absolute instability occurring in the near-wake [24-25]. The connection between the globally unstable BVK mode and local absolute instability has been made by several authors who noted the following behavior. First, the BVK instability is a self-excited limit cycle oscillation of the wake, resulting from a time-amplified global instability [25]. As described in [21], global instabilities are only possible if a region of local absolute instability exists in the flow field. Strykowski and Sreenivasan show that, near the onset of vortex shedding, disturbances grow temporally with the same growth rates at all locations in the flow field [18]. Second, velocity fluctuations due to BVK vortex shedding produce a sharp spectral response at the natural frequency, the amplitude of which is significantly higher than the background noise. Finally, background noise and low-level external forcing do not alter the saturation amplitude or frequency of the BVK instability.

The BVK instability can be suppressed by a number of methods, including the insertion of splitter plates [20], control cylinders [18], and by adding base bleed [21]. One of the most effective methods of suppressing the BVK instability in gaseous flows is

to heat the near-wake fluid. For example, Lecordier et al. delayed the onset of vortex shedding to Reynolds numbers higher than the critical value by directly heating the cylinder with electric current [19]. The authors attributed this suppression to the increased gas viscosity due to heating, which reduced the vorticity magnitude in the near-wake, thereby preventing the shear layers from interacting to produce the von Kármán vortex street.

Others have shown this suppression to be due to the flow transitioning from absolutely to convectively unstable when the heating is sufficiently high. In a parallel linear stability analysis, Yu and Monkewitz investigated wake flow with varying gas density in the transverse direction [22]. In the case of a heated wake, the density in the low velocity region (i.e., toward the wake centerline) is lower than that in the free-stream. The authors show that absolute instability is suppressed as the centerline-to-free stream gas density ratio decreases beyond a critical value. This critical density ratio depends upon the ratio of the centerline to free-stream velocity, with flows having strong flow reversal being more susceptible to absolute instability. These results have important implications to reacting bluff body wakes, as combustion heat release will significantly reduce the recirculation zone gas density. This idea will be discussed extensively in Chapter 5 of the current work, in which the results of the stability analysis described in [22] will be compared with data measured in reacting flow experiments.

1.2.2 Influence of Combustion Heat Release upon the Flow Field

The presence of exothermic reactions significantly alters the flow field characteristics described above for non-reacting bluff body wakes. Notably, combustion heat release substantially reduces turbulence intensities and vorticity magnitudes in the flow [26-27]. In fact, the von Kármán vortex street, one of the most prominent features of isothermal bluff body wakes, is typically not observed for reacting bluff body flow.

Instead, the flame is often stabilized in two distinct, symmetric shear layers downstream of the bluff body, as shown in the spark-Schlieren photograph of Figure 1.3 [28].

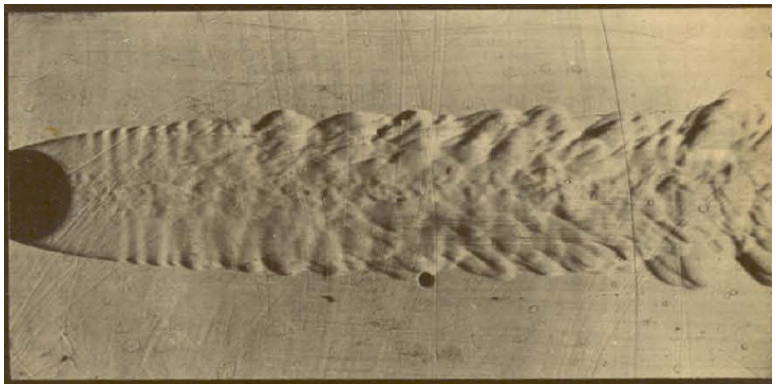

Figure 1.3: Schlieren photograph of a high dilatation ratio (ρ_u/ρ_b) bluff body-stabilized flame, showing wake symmetry (reproduced from [28]).

To understand how combustion heat release affects the flow field, consider the vorticity transport equation, Equation 1.2, which describes the evolution of vorticity in the flow. Combustion results in gas expansion (i.e., dilatation) and baroclinic vorticity generation at the flame front, which are described by the second and third terms on the right-hand-side of Equation 1.2, respectively. The magnitudes of both terms are proportional to the density ratio across the reaction zone, ρ_u/ρ_b, often referred to as the dilatation ratio [12]. Dilatation is a vorticity sink, whereas the baroclinic term is a vorticity source. In the case of a confined bluff body-stabilized flame, baroclinic torque generates vorticity of opposite sign to the bluff body-generated vorticity which exists in the boundary and shear layers [12]. Thus, both dilatation and baroclinic torque decrease the magnitude of vorticity in the shear layers in confined, reacting bluff body flows. As the temperature (and, thus, the density) ratio across the reaction zone increases, these two terms increase in magnitude and reduce the vorticity in the bluff body flow field further.

Furthermore, the high gas temperatures resulting from the combustion process increases the gas viscosity, which increases viscous dissipation of the vorticity (represented by the fourth term in the right-hand-side of Equation 1.2).

$$\frac{D\vec{\omega}}{Dt} = (\vec{\omega}\cdot\nabla)\vec{V} - (\nabla\cdot\vec{V})\vec{\omega} + \frac{\nabla\rho\times\nabla p}{\rho^2} + \nu\nabla^2\vec{\omega} \tag{1.2}$$

The effect of premixed combustion upon the vorticity in the reacting shear layers was investigated in an experimental study by Nair and Lieuwen [29]. The authors used Particle Image Velocimetry (PIV) to measure the instantaneous vorticity in the reacting wake for two equivalence ratios: one near lean blow off (Φ~0.6) and one at a higher, more stable (i.e., further from blow out) equivalence ratio (Φ~0.72). The authors show that the vorticity magnitude in the reacting shear layers was higher for the leaner (Φ~0.6) case, due to the reduction in baroclinic vorticity generation and dilatation resulting from the lower temperature rise across the flame. For both cases, the vorticity magnitude decreased along the flame front with increasing axial distance from the flame holder, until the vorticity switched sign (direction) at a certain distance downstream. This sign reversal occurred sooner for the richer (Φ~0.72) case due to its stronger density gradient. Shanbhogue et al. note that the time-averaged flow field switches from a wake to a jet at this location [12].

A computational study by Mehta and Soteriou provided additional insight into the effects of combustion upon the bluff body vorticity field [30]. The authors were able to isolate the influence of each of the vorticity sink and source terms in equation 1.2 upon the reacting flow field. Their results show that dilatation due to combustion has the most significant damping effect on vorticity in the near-field (i.e., x/W < 4-5), whereas baroclinic generation plays a secondary role. Further downstream, the baroclinic term was found to be the dominant damping mechanism.

Due to the damping mechanisms described above, bluff body-stabilized reacting flows resulting in sufficiently high temperature increase do not possess the coherent vortical structures observed in the non-reacting case. Consequently, the BVK instability is not observed in high dilatation ratio, bluff body-stabilized combustion processes operating away from extinction limits. Mehta and Soteriou postulate that the reduction in vorticity due to combustion prevents the separated shear layers from interacting to produce coherent von Kármán vortices when the dilatation ratio (ρ_u/ρ_b) is sufficiently high [30].

However, significant changes in the reacting flow dynamics occur as blow off limits are approached. Notably, sinusoidal flame oscillations due to asymmetric vortex shedding have been observed for premixed flames operating near lean and rich blow out [12-15, 31], likely due to a decrease in magnitude of the suppressing mechanisms described above. The earliest documented detection of such flame oscillations was by Thurston who observed a sinuous flame structure near lean blow off using Schlieren photography. An example of his results is reproduced in Figure 1.4 [31].

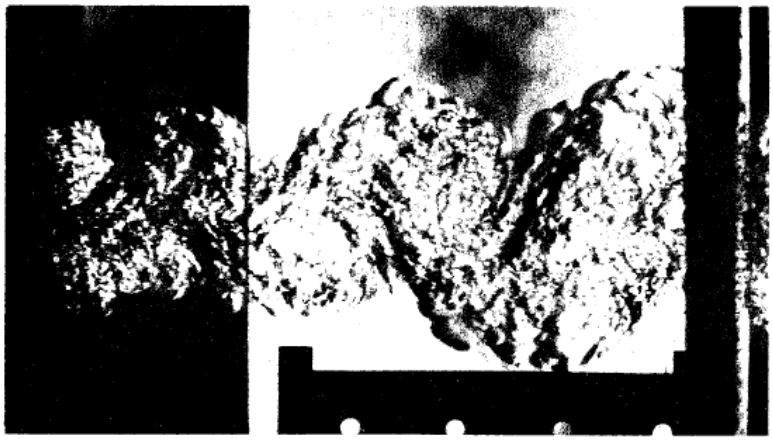

Figure 1.4: Schlieren photograph of a bluff body-stabilized flame near lean blow out, showing asymmetric vorticity (reproduced from [31]).

More "quantitative" evidence of vortex shedding in lean, premixed bluff body-stabilized flames was reported by Hertzberg et al. [32]. The authors used Laser Doppler Anemometry to measure velocity fluctuations for open, reacting flow stabilized by a thin cylinder. Velocity power spectra revealed a sharp, narrowband response for flames operating near lean blow out, which suggested the flow had transitioned to absolute instability. A linear stability analysis performed in a later study by the authors confirmed that absolute instability could occur for premixed flames operating near lean blow out [33]. It is worth noting that the measured velocity fluctuation frequency for the lean reacting flow was lower than that resulting from isothermal flow at the same incoming velocity and cylinder diameter, creating uncertainty as to whether the reacting flow fluctuations were due to BVK vortex shedding or another mode of instability. The reacting flow velocity fluctuations occurred with a Strouhal number of approximately 0.09, whereas the non-reacting case resulted in fluctuations at St~0.17.

Recent studies have used high-speed imaging to further investigate the dynamics of premixed bluff body-stabilized flames operating near lean blow off [14-15]. Nair and Lieuwen observed sinuous flame oscillations reminiscent of von Kármán vortex shedding near lean blow out, but the authors point out that these fluctuations were not as organized as the coherent structures observed in non-reacting bluff body flows [29]. Acoustic power spectra revealed these heat release fluctuations occurred at St~0.3, which is in the range of reported Strouhal numbers corresponding to the BVK instability. Recall that the authors found the vorticity in the reacting shear layers to increase in magnitude as the equivalence ratio was reduced toward lean blow off [29]. This result supports the postulates of Mehta and Soteriou [30] and Gerrard [17], who suggested this increase in vorticity strongly influences the formation of the von Kármán vortex street.

Von Kármán vortex shedding can also occur for a wider range of fuel-air ratios when the incoming reactant temperature is high, as the density ratio across a flame, ρ_u/ρ_b, decreases with increasing reactants temperature. This was demonstrated in a numerical

study by Erickson et al. who investigated the influence of the burned to unburned gas temperature ratio, T_b/T_u, upon the wake vortex dynamics [34]. The authors show a complete transition in flame stabilization and wake structure from asymmetric vortex shedding at global temperature ratios less than 1.5 to flame stabilization in two distinct shear layers at T_b/T_u~2. Examples of their results are reproduced in Figure 1.5, clearly showing the difference in flame symmetry for two temperature ratios. Recent experimental studies by Emerson et al. show this transition is marked by intermittency in wake symmetry, with the flame spending more time in the asymmetric, BVK mode as the global temperature ratio decreases [35-36]. A parallel, linear stability analysis performed by the authors demonstrated that this transition in flame/wake symmetry was due to the flow transitioning from convective to absolute instability as the temperature ratio was reduced [36].

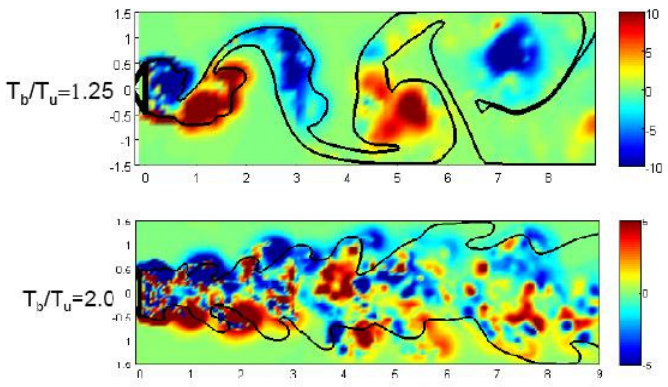

Figure 1.5: Computed instantaneous vorticity and flame sheet location (black lines) for premixed bluff body-stabilized flames with varying temperature ratio, T_b/T_u (reprinted from [34] with permission of the American Institute of Aeronautics and Astronautics).

These results have important implications for the design and performance of practical bluff body-stabilized combustors used in, e.g., turbofans and ramjets. Due to the high reactants temperatures in such systems, the burned-to-unburned temperature

ratios, T_b/T_u, can be relatively low. If operating at fuel-lean conditions, the resulting flame temperature can be less than twice the reactants temperature if the reactants are sufficiently preheated. Thus, the BVK instability is likely to occur in such practical combustion systems due to the low temperature rise across the flame.

1.2.3 Research Needs

Though previous studies have shown that combustion heat release can alter bluff body wake dynamics, the problem of BVK vortex shedding in reacting wakes is not fully understood because it has not been sufficiently investigated to date. More detailed investigations over wider ranges of operating conditions are needed to better understand how these interactions affect various aspects of the combustion process, including mixing, blow off and dynamic stability. Such understanding could lead to improvements in the static and dynamic stability of practical bluff body-stabilized combustion systems.

All current understanding of vortex shedding in reacting bluff body wakes has been established in terms of global flow properties. Specifically, it is known that for premixed flames, the BVK instability can appear as the global temperature ratio, T_b/T_u, approaches unity or if the combustor is operating near blow off. In premixed combustion processes the flame temperature (and therefore, T_b/T_u) is assumed to be uniform throughout the flow field. However, many practical combustion systems (e.g., aircraft engines) employ liquid fuel injection, and spatial non-uniformities in fuel-air ratio and products gas temperature are likely to exist throughout the reaction zone. The influence of spatial non-uniformities in local thermodynamic properties, such as density ratio, upon the onset and amplitude of the BVK instability is unknown and needs to be determined. That is, the understanding of the problem needs to be re-cast in terms of local properties of the flow instead of global ones.

1.3 Thesis Objectives and Overview

The primary objective of this thesis is to elucidate the fundamental processes controlling the BVK instability in bluff body-stabilized combustion processes. In particular, the influence of spatial non-uniformities in fuel-air ratio and heat release upon the onset and amplitude of this instability will be determined. In light of this objective, this thesis will address the following questions:

1.) What are the fundamental processes controlling BVK-associated heat release oscillations in liquid-fuelled, bluff body-stabilized flames, in which spatial non-uniformities in fuel-air ratio and heat release are likely? Are such systems more or less susceptible to the BVK instability than premixed combustion systems?
2.) How do the spatial distributions of fuel-air ratio and subsequent heat release affect BVK vortex shedding in reacting bluff body wakes? Is there a region of the reacting wake in which the local combustion processes influence the BVK instability more than other regions?
3.) Can the onset and amplitude of BVK heat release fluctuations be correlated to local thermodynamic properties of the flow field (e.g., local density ratio, ρ_u/ρ_b)? If so, are such criteria applicable for all methods of fuel injection?

This thesis will demonstrate that knowledge of global flow properties alone is insufficient to determine when the transition to an absolutely unstable, von Kármán wake structure occurs. Instead, the spatial distributions of thermodynamic properties such as gas temperature need to be known in order to predict the onset of absolute instability in reacting wakes.

A secondary objective of this thesis is to characterize the spatial and temporal distributions of combustion process heat release in bluff body-stabilized combustion

systems employing "close-coupled" fuel injection [37-38]. In this configuration, the fuel is supplied via discrete liquid jets that are injected into the cross-flow a short distance upstream of the flame stabilization point. While this method of fuel injection is used in some gas turbine engines, the characteristics of the combustion process have not been studied adequately. Thus, there is a need to improve understanding of the fundamental processes controlling bluff body-stabilized combustion with this method of fuel injection.

The remainder of this thesis is organized as follows. Chapter 2 describes the experimental methods employed to meet the above objectives. The experimental results are presented in Chapters 3 and 4. Chapter 3 describes the measured dependence of the BVK heat release dynamics upon operating conditions and fuel injection mode, while Chapter 4 describes the time-averaged, spatially-resolved measurements of heat release and fuel-air ratio at these conditions. Chapter 4 closes by correlating the measured flame dynamics with the spatial fuel-air ratio and heat release distributions in order to identify the fundamental processes controlling the BVK instability in reacting bluff body wakes.

A parallel, linear stability analysis is presented in Chapter 5 which supplements the experimental results. The objective of this analysis is to elucidate the influence of the spatial heat release distribution upon the hydrodynamic instability characteristics of reacting bluff body wakes. Finally, Chapter 6 summarizes the key findings and contributions of this work and provides recommendations for future studies.

CHAPTER 2

EXPERIMENTAL METHODOLOGY

This chapter describes the experiments carried out to investigate the interaction between combustion process heat release and von Kármán vortices shed from bluff bodies. A description of the test facility is given first, followed by the optical diagnostics employed to measure the spatial and temporal distributions of the combustion process heat release. Finally, a description of the experimental procedure is given.

2.1 Description of Test Facility

2.1.1 Test Rig and Instrumentation

Experiments were performed in the single flame holder combustor shown schematically in Figure 2.1. The three primary sections of the test rig are the pre-burner, flow conditioning and bluff body test sections. Natural gas was burned with heated air (350°C) in the pre-burner to supply a high-temperature, vitiated gas stream (consisting primarily of air, H_2O and CO_2) to the bluff body test section. Diluting air was added to the pre-burner exhaust to lower the temperature and increase the oxygen concentration of the vitiated gas stream. A perforated plate installed 0.65 m upstream of the bluff body flame holder "straightened" the flow and reduced its turbulence intensity prior to reaching the bluff body test section. Downstream of the perforated plate (~0.23 m), the rig geometry transitioned from a 20 cm diameter circular cross-section to the 7.62 by 15.24 cm rectangular bluff body test section. Thermocouples, a Pitot tube, and an oxygen sensor installed just upstream of the bluff body flame holder measured the temperature, pressure, and oxygen concentration of the incoming gas stream. Inlet gas conditions ranged from a velocity between 65 and 250 m/s, temperature from 400°C to 875°C, and

oxygen content between 13 and 21% by volume. The static pressure of the incoming gas stream was just above atmospheric, with typical values ranging from 15.5 to 18 psia.

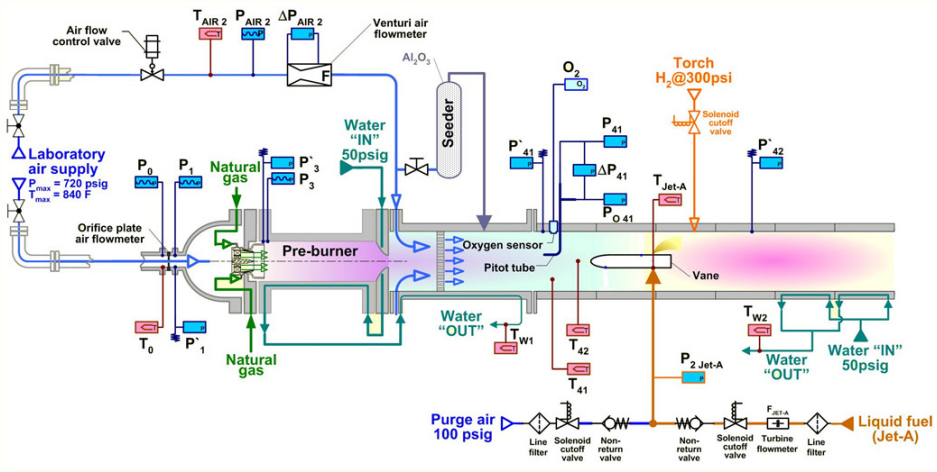

Figure 2.1: Schematic of the single flame holder combustor test rig.

A bluff body flame holder stabilized combustion of Jet-A fuel with the vitiated air stream. This combustion process was ignited by a hydrogen torch installed approximately 4.5 cm downstream of the bluff body trailing edge. The bluff body test section is ~1.5 m long and has a 0.9 m transparent section that provides optical access to the combustion process. The 15.24 cm square windows (six on each side) are supported by a structural frame that is water cooled to reduce thermal expansion and prevent window cracking during operation. Cooling air jets distributed along the length of the transparent section impinged onto the outside surface of the windows to minimize their temperature during operation.

Dynamic pressure sensors were installed at several axial locations along the combustor. Pressure transducers labeled $P`_{41}$ and $P`_{42}$ in Figure 2.1 monitored the dynamic pressure upstream and downstream of the bluff body flame holder, respectively. Two data acquisition systems were used to record these and other sensors outputs during

the tests. The first of which operated at 100 Hz to record mean flow data such as air and fuel flow rates, inlet gas temperature and velocity, and static pressure. The other system (Sony SIR-1000i) operated at 48,000 Hz to monitor the dynamic behavior of the combustion process, including oscillatory pressure measurements. LABVIEW, a graphical programming language by National Instruments, was used for data acquisition.

2.1.2 Description of Flame Holder and Fuel Injection Configurations

Two different bluff body geometries were investigated, schematics of which are shown in Figure 2.2. The first bluff body design, which will be referred to as the "vane", had an elliptical leading edge and a rectangular trailing edge (see Fig. 2.2a). Two vane widths were tested: 3.18 and 4.75 cm. The second bluff body geometry consisted of the 3.18 cm vane with two rectangular plates attached to its trailing edge, as shown in Figure 2.2b. These plates were inclined at a 46° angle with respect to the axial coordinate. This configuration will be referred to as the "V-gutter" throughout this thesis, although it should be noted that its geometry is not like that of a classical V-gutter. The use of detachable plates allowed the bluff body blockage ratio to be readily varied. Four V-gutter widths were tested: 5.72, 5.08, 4.75 and 4.45 cm.

For each flame holder configuration, liquid Jet-A fuel was injected across the vitiated gas stream via 4 simple-orifice fuel injectors integrated within the bluff body (2 on each side), located 2.5 cm upstream of the vane's trailing edge (see Figure 2.2c). The diameter of each fuel injector integrated within the 4.75 cm vane was 0.635 mm, whereas the 3.18 cm vane (and thus, the V-gutter configurations) used four 0.560 mm fuel injectors. The proximity of the fuel injectors to the reacting wake limited fuel and air mixing prior to burning. For this "close-coupled" fuel injection configuration, the fuel distribution in the reaction zone is highly dependent on the fuel jet penetration into the cross-flow, which increases with increasing fuel jet to cross-flow momentum flux ratio, i.e., $(\rho V^2)_{liq} / (\rho U^2)_{air}$ [37-38].

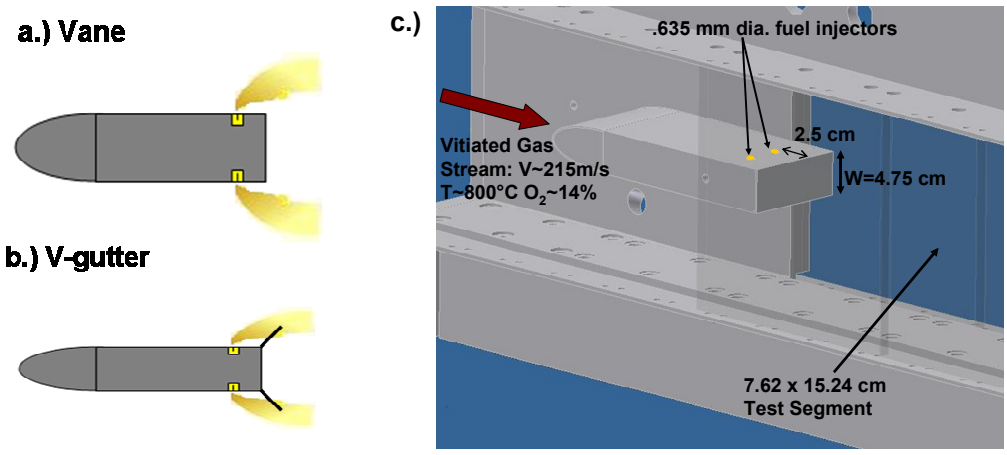

Figure 2.2: Schematics of (a.) Vane and (b.) V-gutter flame holder geometries; c.) 3D drawing of 4.75 cm Vane installed in the test rig, showing fuel injector locations.

Experiments were also performed with Jet-A fuel injection occurring well-upstream of the bluff body. This provided more time for the fuel to evaporate and mix with the incoming air stream prior to burning, resulting in a presumably well-mixed reactants stream (though the uniformity of the reactants fuel-air ratio is not known). The fuel was injected via a cylindrical fuel bar installed upstream of the bluff body. Two different upstream fuel injection configurations were used, as shown in Figure 2.3.

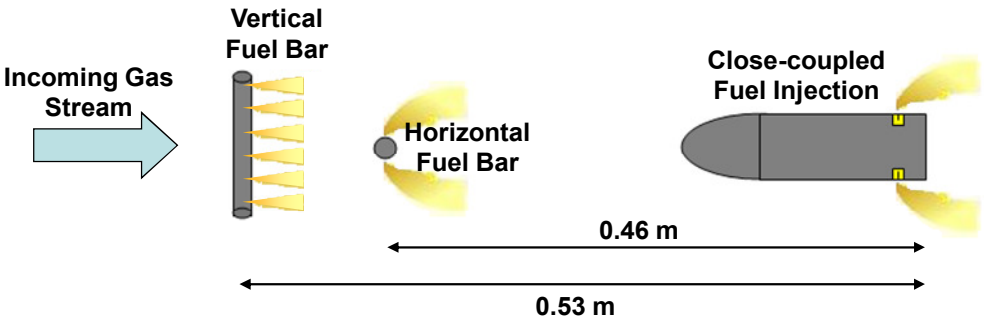

Figure 2.3: Illustration of fuel injection configurations utilized in this study, comparing upstream and close-coupled fuel injection modes (not drawn to scale).

The first cylindrical fuel bar was 6.35 mm in diameter and located 0.46 m upstream of the bluff body trailing edge. Its axis was oriented in the span-wise direction, extending the entire span of the combustor along the transverse center plane. This configuration is referred to as the "horizontal fuel bar" in Figure 2.3 and throughout the remainder of this thesis. This fuel bar configuration injected Jet-A perpendicular to the incoming flow through six simple-orifice injectors (3 on each side) which were 0.51 mm in diameter and spaced 19 mm apart from one another.

The other cylindrical fuel bar was oriented in the transverse direction, which is referred to as the "vertical fuel bar" in Figure 2.3 and for the remainder of this thesis. This fuel bar was installed 0.53 m upstream of the bluff body trailing edge and consisted of 16 simple-orifice injectors (8 on each side) which were 0.46 mm in diameter and spaced ~19 mm apart. The injectors were oriented 30° with respect to the combustor axial coordinate, injecting Jet-A "against" the incoming flow stream instead of perpendicular to it. This was done in order to prevent the fuel spray from impinging upon the combustor side walls during operation.

It should be noted that for tests investigating close-coupled fuel injection, no fuel was injected upstream of the bluff body flame holder. When experiments requiring upstream fuel injection were performed, only one fuel bar was installed at a time. Such tests were performed only when direct comparisons of the heat release distributions between upstream and close-coupled fuel injection modes were desired. The fuel supply system was set up in a manner which allowed the fuel injection location to be altered between the upstream fuel bar and the flame holder during testing, thus helping to reduce the discrepancy in global operating conditions for such comparisons.

2.2 Characterization of Oscillatory Heat Release using High-speed Photography

High-speed photography was used to characterize the oscillatory combustion heat release over a wide range of operating conditions. These movies were recorded using a NAC GX-1 high-speed camera at frame rates of 10 and 24 kHz, with exposure times of 12 and 10 μs, respectively. The amplitudes and frequencies of the oscillatory heat release were obtained by processing the movies using the methods described below.

A flame luminosity time history was created for each axial location in the combustor using the methodology illustrated in Figure 2.4. For each frame in the movie sequence (marked N), a thin vertical strip (1 pixel wide) was extracted from the flame image at the given axial location. These strips were then "stacked" in chronological order to produce the time dependence of the light intensity at the given axial cross-section, as shown in the figure. The red color signal was rejected from these time histories so that only light intensity recorded by the blue and green color channels of the camera, which contain contributions from CH* and C_2* chemiluminescence, would be considered for oscillatory heat release measurements (see Appendix A for a comparison of data obtained using this method to that obtained with a CH* band-pass filter installed). The blue and green signals were then averaged to produce a monochromatic flame emission time history.

A two-dimensional Discrete Fourier Transform (DFT) was performed on each flame emission time history in order to obtain the amplitudes and frequencies of the oscillatory heat release at that particular axial location. The resulting transform is a two-dimensional image in the frequency domain, with horizontal axes representing the frequency of flame oscillations in Hz, while vertical axes have units of 1/length and represent the variation in light intensity in the transverse direction. The pixel intensity at each location in the Fourier image is the spectral amplitude of the flame dynamics at the corresponding frequency.

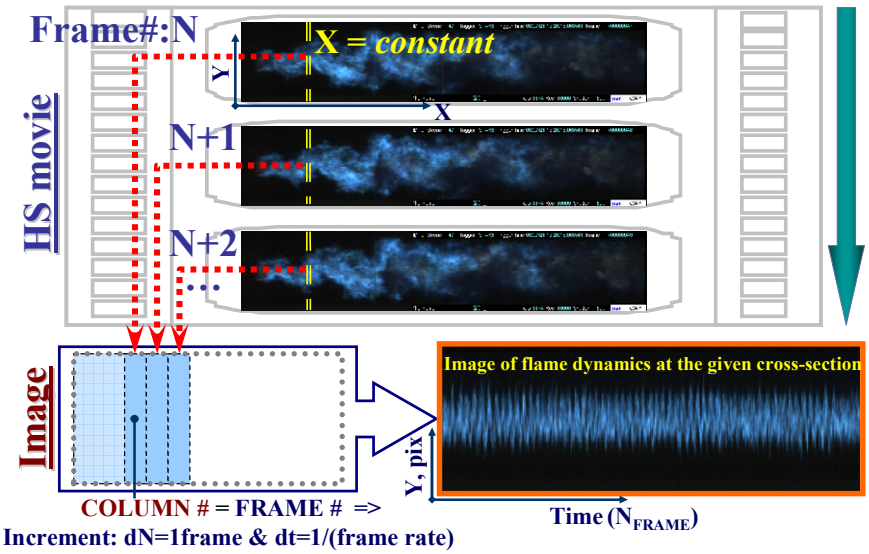

Figure 2.4: Method for recording flame dynamics at a given axial location.

An example of this 2D Fourier analysis is shown in Figure 2.5, which reveals two dominant frequencies of heat release oscillations. The first one is just over 230 Hz and has its peak intensity along the centerline of the Fourier image, shown in Figure 2.5b. This corresponds to a ¾-wave longitudinal acoustic mode of the combustor. The second dominant mode was around 1287 Hz and was due to asymmetric vortex shedding from the bluff body (i.e., the BVK instability). Its maximum intensities were shifted 1 - 2 pixels above and below the Fourier image center line, distinguishing it from the longitudinal mode. This shift reflects the transverse nature of the BVK heat release oscillations due to the alternate shedding and subsequent convection of the coherent structures at a small angle relative to the combustor axial coordinate. In contrast, the longitudinal fluctuations were present over the entire cross-section and propagated parallel to the axial coordinate. Thus, its peak intensities lied on the Fourier image centerline.

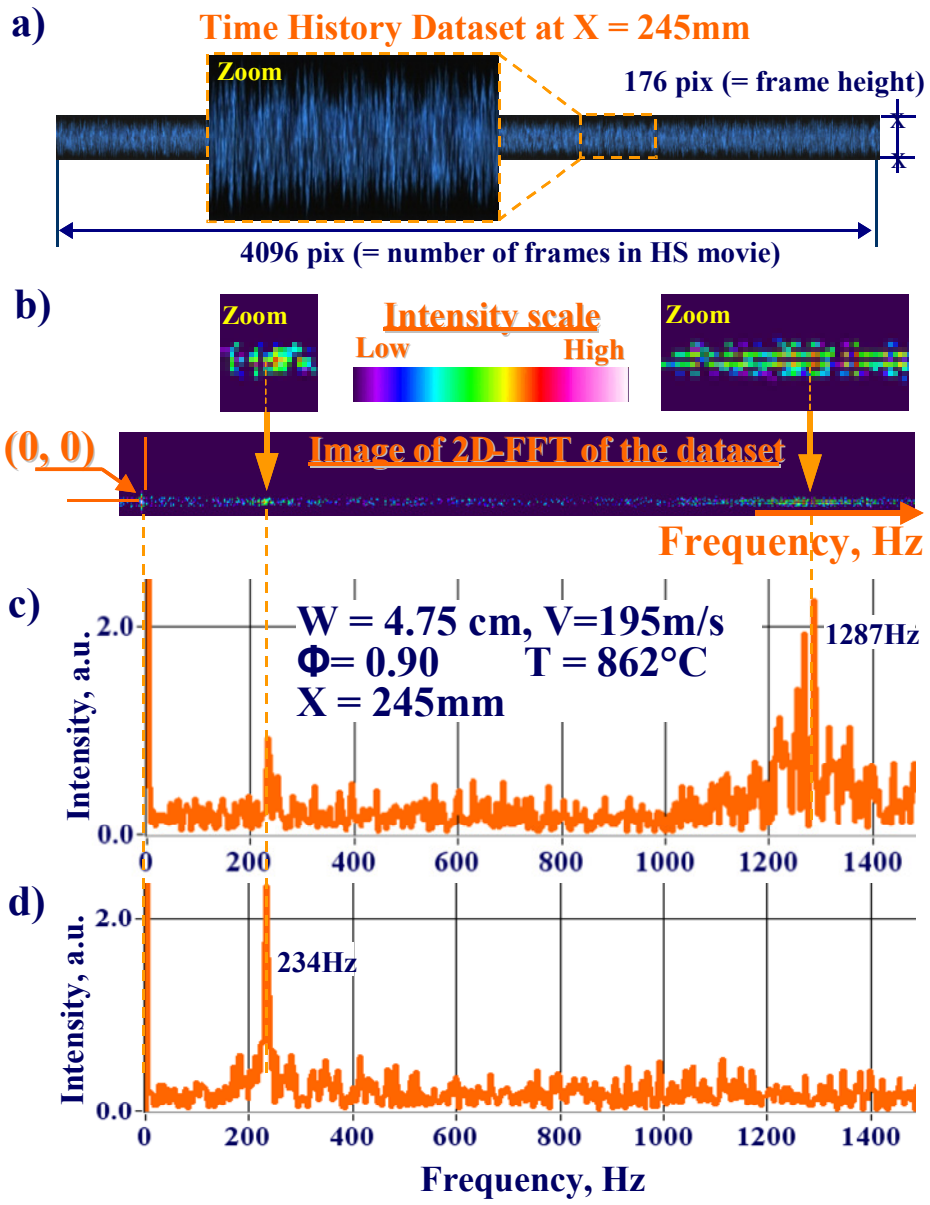

Figure 2.5: Example of time history (a), two-dimensional FFT (b), and extracted power spectra of flame oscillations at: (c) y=1 pixel above combustor centerline, and (d) along combustor centerline.

The Fourier images can be readily "transformed" into more conventional power spectra by extracting horizontal cross-sections of pixel intensity at different vertical coordinates in the image, examples of which are shown in Figures 2.5-c and –d. The flame spectrum obtained along the centerline of the Fourier image is shown in Figure 2.5d, which reveals only the presence of the 234 Hz longitudinal instability. The spectrum obtained at 1 pixel above the centerline is shown in Figure 2.5c, showing a strong peak at the BVK frequency of 1287 Hz, as well as smaller amplitude oscillations of the longitudinal instability. The maximum amplitude in the transformed power spectra at frequencies typical of the BVK instability (i.e., $0.20 < St < 0.29$) were used as a measure of the "strength" (or amplitude) of the heat release oscillations due to vortex shedding. This amplitude was normalized by the mean (DC) component of the 2D DFT at each particular cross-section in order to eliminate the influence of changes in overall luminosity as operating conditions were varied. For example, movies recorded for two flames of equal global fuel-air ratio but with different inlet velocities will have different flame emission intensities due to the differences in the amount of fuel burned. Normalizing the spectral amplitudes by the average luminosity (represented by the DC component) resulted in a measurement of the oscillatory motion of the flame in the transverse direction.

The high-speed movies were also processed using flame edge tracking methods, which are described in Appendix B. The flame edge tracking analyses produced results that were very similar to those obtained using the 2D DFT method described above (see Appendix B for comparisons of the two methods). Thus, only the results obtained using the 2D DFT method will be described in the body of this thesis (i.e., Chapters 3-6).

2.3 Stationary Heat Release Measurements using Chemiluminescence Imaging

Spatial distributions of the time-averaged heat release were characterized by imaging flame chemiluminescence, which is the naturally-occurring radiative emission by electronically-excited radicals in the reaction zone. These radicals emit light in the ultraviolet and visible spectra, the intensity of which is directly related to the concentration of the emitting species [39]. In hydrocarbon-air combustion, OH*, CH* and C_2* chemiluminescence are extensively used to gain information about the state of the reaction, since the characteristic lifetimes of these radicals are much shorter than typical residence times in combustors [40]. CH* and OH*, in particular, have been extensively used as measures of heat release, as previous studies have shown the amount of light emitted from these radicals to be proportional to the amount of fuel consumed, though there is some dependence upon equivalence ratio, pressure and temperature [39-42].

The chemiluminescence imaging system used in this study is shown schematically in Figure 2.6. This system contains three Foculus FO531 cameras (1600 x 1200 pixel spatial resolution) which take wavelength-specific images of the flame with a field of view covering the entire 0.9 x 0.15 m transparent section of the combustor. Two of the cameras are monochromatic and are equipped with band-pass filters to collect emission only in wavelengths containing C_2* ($503 < \lambda < 519$ nm) and CH* ($422 < \lambda < 432$ nm) chemiluminescence, respectively. The third camera is a color camera equipped with two triple-band pass filters (see Figure 2.6) to collect flame radiation in three specific bands for subtraction of background radiation (due to CO_2* broadband emission and thermal emission) from the CH* and C_2* images. These "pedestal" bands are shown in the Jet-A flame emission spectrum of Figure 2.7, with wavelengths of 442-459, 520-539, and 600-617 nm.

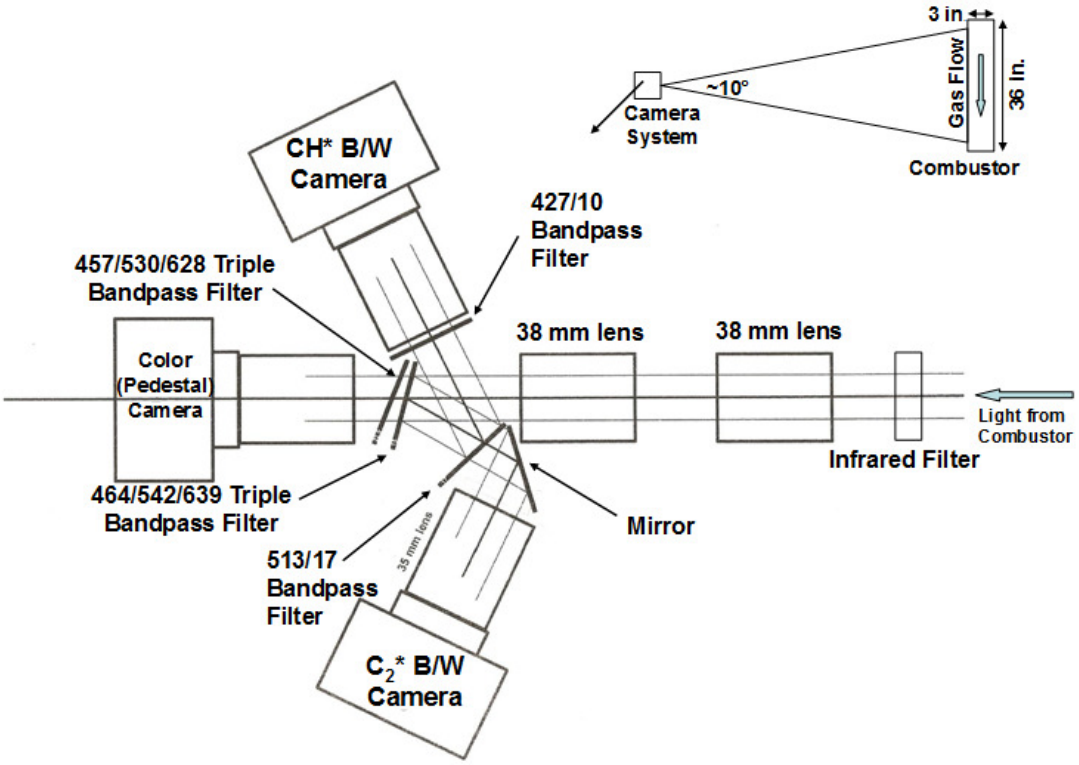

Figure 2.6: Schematic of the Three-camera Chemiluminescence Imaging System.

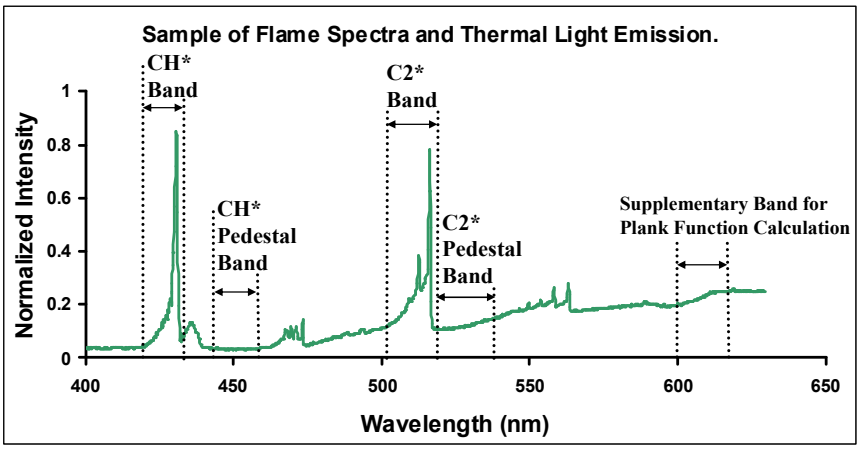

Figure 2.7: Measured Jet-A and air flame emission spectrum, showing bands collected by each camera.

In order to correct for background radiation, the emission occurring in the "pedestal" bands of Figure 2.7 were subtracted from the CH* and C_2* images using the following procedure. First, the three color components (red, green and blue) of the background image were separated into three individual gray-scale images, each one corresponding to a different color component. The blue and green component background images were then multiplied by a correction factor and subtracted from the CH* and C_2* images, respectively. These coefficients were determined by comparing images collected by the three-camera system to background-corrected CH* and C_2* emission measured by a scanning spectrometer. Transverse and axial cross-sectional profiles of chemiluminescence intensity were extracted from the images at locations corresponding to points in which the optical probe collected flame emission. The coefficients which produced the best match between the digitally-extracted profiles and the spectrometer scans were chosen as the correction factors for all subsequent image processing. An example of this comparison is shown in Figure 2.8, which compares transverse CH* profiles measured by these two techniques at an axial location of 1.4 bluff body widths downstream of the flame holder trailing edge. Figure 2.9 shows the resulting spectrum measured by the CH* and C_2* images after background correction.

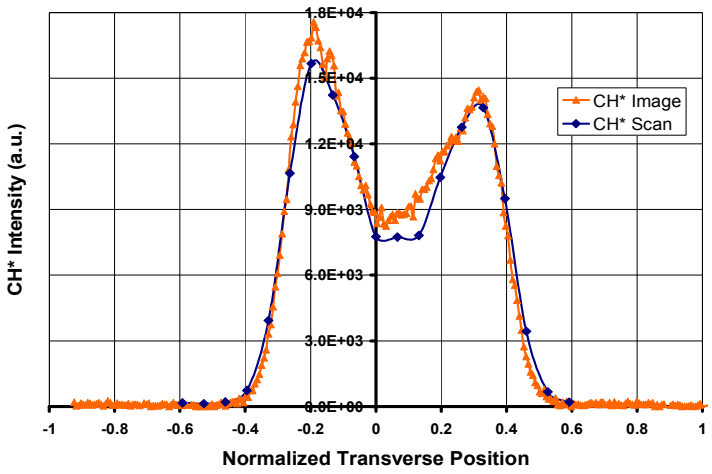

Figure 2.8: Transverse CH* profiles at x=1.4W, comparing background-corrected image profiles with spectrometer scan (V_{in}=180 m/s, Φ_{global}=0.7).

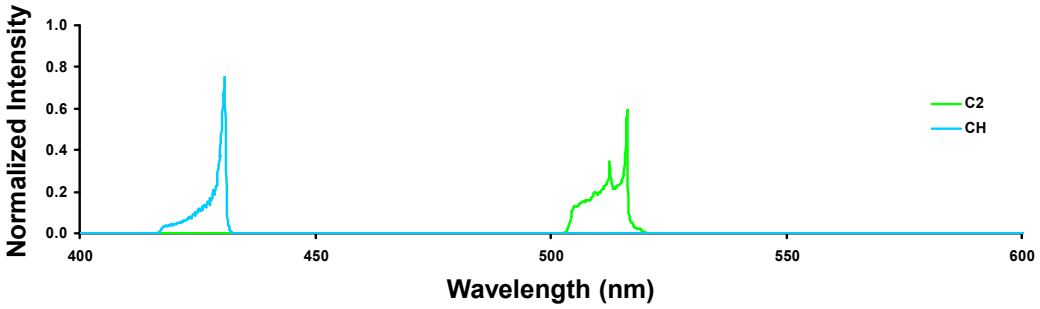

Figure 2.9: Resulting CH* and C_2* emission bands collected by cameras after background subtraction.

For each measurement, 10 images of the flame were recorded by each camera with an exposure time of approximately 10 ms. The delay time between images was approximately 0.8 seconds. An image processing algorithm was developed to subtract the background radiation from the CH* and C_2* images (according to the procedure described above), correct for fixed pattern noise, and average the ten background-corrected images into one characteristic image for each operating condition. The resulting time-averaged CH* and C_2* images were used to characterize the spatial heat

release distribution. In addition, ratios of C_2* to CH* emission intensity were used to estimate the local equivalence ratio in the flame, as previous studies have demonstrated this ratio to be proportional to fuel-air ratio in hydrocarbon flames [40, 42-45]. Upon post-processing of the images, "false color" maps were applied to the images to facilitate visual comparisons of the heat release and fuel-air ratio distributions.

2.4 Experimental Procedure

The spatial and temporal distributions of the combustion process heat release were characterized over a wide range of inlet gas velocities, temperatures, global equivalence ratios and bluff body geometries using the diagnostic techniques described in Sections 2.2 and 2.3. The measured global equivalence ratio accounted for the reduced oxygen content of the vitiated air stream and was defined based on the following formula:

$$\phi_{global} = 14.6 \frac{\dot{m}_{jet-A}}{\dot{m}_{air,tot}} \frac{21\%}{O_2\%} \tag{2.1}$$

where $\dot{m}_{jet-A}$ is the measured Jet-A flow rate, $\dot{m}_{air,tot}$ is the combined flow rate of both air streams (i.e., the air entering and leaving the pre-burner and the diluting air added to the pre-burner exhaust), 14.6 is the stoichiometric air-to-fuel ratio for Jet-A and air combustion, and the factor 21% divided by the measured oxygen concentration accounts for vitiation effects.

For each inlet gas temperature and velocity, sweeps of the global equivalence ratio from lean to rich static stability limits were performed. High-speed movies and chemiluminescence images were recorded at certain increments of the global equivalence ratio during each sweep. These Φ_{global} sweeps were performed for each bluff body and fuel injection configuration described in Figures 2.2 and 2.3. Blow out points were determined by viewing the static pressure data recorded by the 100 Hz data recorder, as extinction of the combustion process resulted in a sharp decrease in static pressure.

Table 2.1 summarizes the ranges of operating conditions investigated for each bluff body geometry and fuel injection configuration. The results of these tests are described in subsequent chapters. The BVK heat release dynamics are described in Chapter 3, whereas the time-averaged spatial distributions of fuel-air ratio and heat release are presented in Chapter 4.

Table 2.1: Summary of operating conditions and flame holder / fuel injection configurations tested.

Flame Holder Width (cm)	Shape	Fuel Injection Mode	Approach Velocity (m/s)	Φ_{global}	T_{in} (°C)	O_2%
4.75	Vane	Close-coupled	65 - 250	0.20 - 1.30	400 - 865	13.2 - 21
5.72	V-gutter	Close-coupled	175 - 225	0.20 - 1.00	850 - 860	14.4 - 15.5
5.08	V-gutter	Close-coupled	175 - 230	0.20 - 1.00	855 - 860	14.2 - 15.1
4.75	V-gutter	Close-coupled	155 - 225	0.20 - 1.20	760 - 865	14.1 - 15.9
4.45	V-gutter	Close-coupled	180 - 210	0.20 - 1.00	855 - 860	14.1 - 14.6
4.75	Vane	Upstream (horiz. fuel bar)	125 - 150	0.30 - 1.20	790 - 830	13.6 - 14.0
3.18	Vane	Upstream (horiz. fuel bar)	165 - 220	0.35 - 1.15	810 - 830	15.4 - 15.8
3.18	Vane	Upstream (vert. fuel bar)	170 - 225	0.45 - 1.10	820 - 830	15.7 - 15.9

CHAPTER 3

HEAT RELEASE DYNAMICS

Oscillatory heat release due to BVK vortex shedding was characterized by recording high-speed movies of the flame for a wide range of operating conditions (i.e., fuel-air ratios, approach gas velocities and temperatures, fuel injection modes and bluff body geometries). These movies were processed using the methodologies described in Section 2.2. The results of these measurements and data analyses are presented in this chapter.

3.1 Characteristics of Heat Release Oscillations due to BVK Vortex Shedding

A sequence of five high-speed images representing one period (~0.8 ms) of BVK heat release oscillations is shown in Figure 3.1. These frames were extracted from a 10 kHz high-speed movie with an exposure time of 12 μs. The time increment between the frames shown is 0.2 ms, with "time stamps" labeled on each image. This movie was recorded for a flame operating near globally rich blow out (V_{in}=180 m/s, Φ_{global}=0.95, T=860°C) for the 4.75 cm vane with close-coupled fuel injection. Figure 3.1 shows that high amplitude transverse heat release oscillations due to vortex shedding occurred at this near-blow out operating condition. The alternate shedding and subsequent convection of the von Kármán vortices gives the flame a sinuous wave-like structure due to the vortex-flame interactions. The vertical dashed line crossing these images and coinciding with the first "crest" of this undulating flame structure on the first and last frames illustrates the convection of the vortices along the combustor.

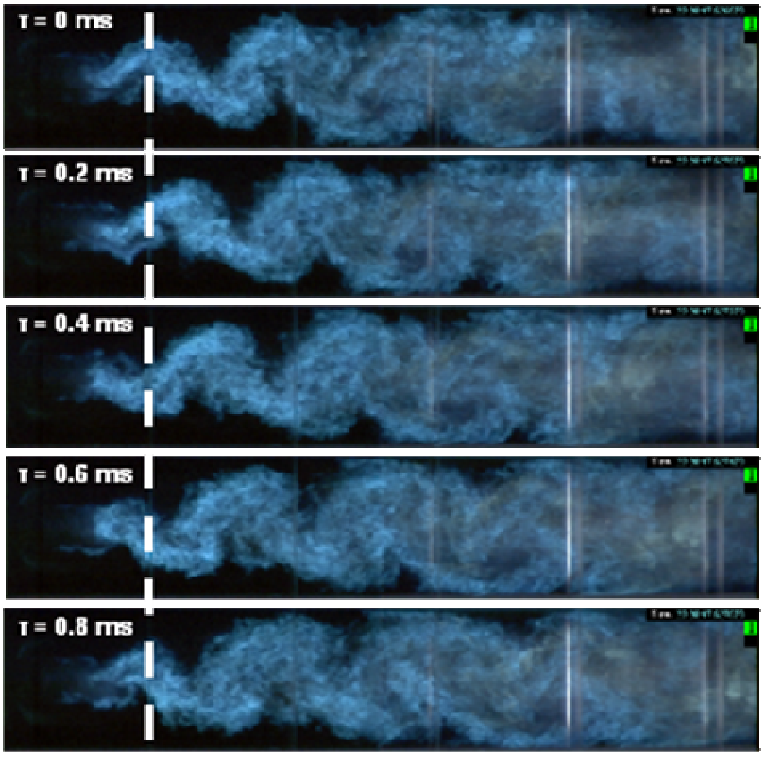

Figure 3.1: Sequence of high-speed images representing one period of BVK heat release oscillations (V_{in}=180 m/s, Φ_{global}=0.95, T=860°C, 4.75 cm Vane).

The axial distribution of the BVK heat release dynamic amplitude is shown in Figure 3.2a for the full movie sequence described above. This data was obtained using the 2D DFT method described in Section 2.2. Figure 3.2a shows that the amplitude of heat release oscillations due to vortex shedding increased with axial distance, peaking at ~ 155 mm (or ~3.25 bluff body widths) downstream of the bluff body trailing edge before gradually decaying further downstream. These heat release fluctuations occurred at a frequency of 1211 Hz for this inlet velocity and flame holder geometry. This corresponds to a Strouhal number of approximately 0.21 if the bluff body width is taken as the characteristic length and the estimated lip velocity of 277 m/s is used as the reference velocity. Note that this Strouhal number equals that occurring in an isothermal flow around a cylinder at high Reynolds numbers [12].

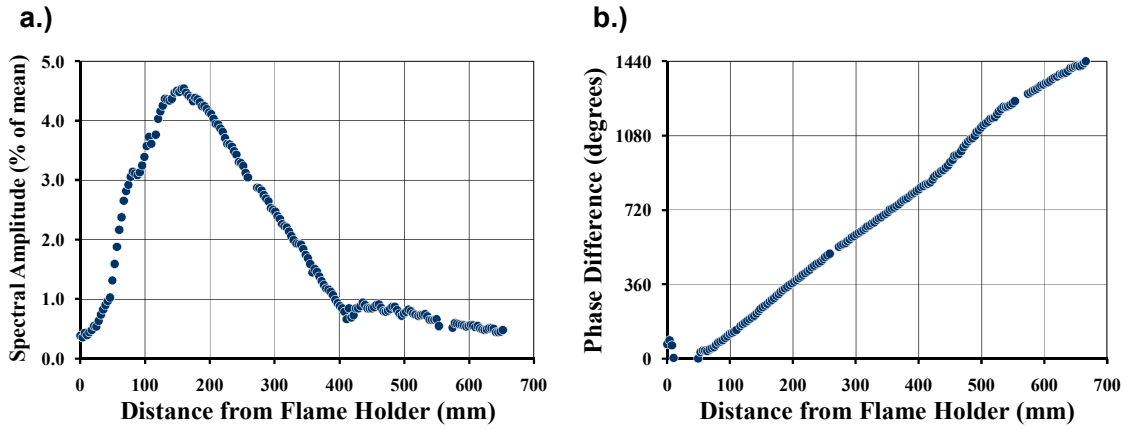

Figure 3.2: Axial variation of (a.) BVK heat release oscillation amplitude, and (b.) phase difference between dynamic heat release and pressure (V_{in}=180 m/s, Φ_{global}=0.95, T=860°C, 4.75 cm Vane).

Also shown in Figure 3.2 (part b) is the downstream variation of the phase difference between heat release and pressure oscillations at the BVK frequency (1211 Hz). Pressure transducer $P`_{42}$ (installed 19.3 cm behind the bluff body, see Figure 2.1) was used as the reference for determining this phase difference. Figure 3.2b shows a linear increase in phase with distance, indicating convection of the BVK vortices at a constant velocity of ~ 186 m/s, which is slightly higher than the measured approach gas velocity of 180 m/s. Deviation in this linear phase dependence was not observed until approximately 400 mm (i.e., x/W~8.5) downstream of the bluff body trailing edge, where the reacting vortices interacted with the test section walls. A similar discontinuity can be seen at the same axial location in the heat release dynamic amplitude plot in Figure 3.2a.

A flame luminosity power spectrum taken at x=185 mm (just downstream of the peak amplitude in Fig. 3.2a) is shown in Figure 3.3, which reveals the absolute nature of the BVK instability. As discussed in Chapter 1, absolute instabilities are characterized by narrowband velocity spectra, with amplitudes at the natural frequency generally being several orders of magnitude greater than the background noise. Figure 3.3 shows a sharp peak at the BVK frequency much greater in amplitude than the background noise,

presumably due to such narrowband velocity oscillations. This supports the postulate that the global, BVK instability in reacting flows is due to the existence of a region of local absolute instability in the flow. In addition, Figure 3.3 shows moderate amplitude fluctuations (~1% of the mean) at the first harmonic (~2422 Hz). Note that Figure 3.3 has been high-pass filtered above 350 Hz.

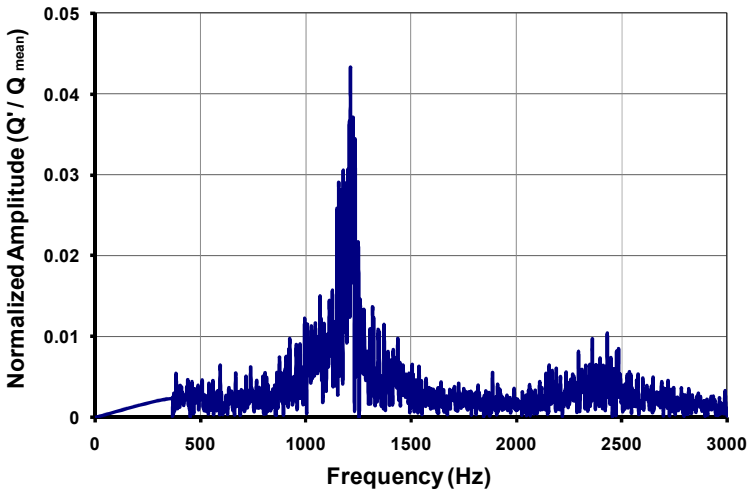

Figure 3.3: Flame luminosity power spectrum obtained at x=185 mm downstream of the 4.75 cm. Vane trailing edge (V_{in}=180 m/s, Φ_{global}=0.95).

Despite the high-amplitude heat release fluctuations shown in Figures 3.1-3, the combustion chamber acoustics at the BVK frequency were negligible. In fact, dynamic pressure amplitudes at these frequencies never exceeded twice the background noise for all operating conditions tested, indicating a lack of coupling between BVK heat release oscillations and combustion chamber acoustics. It is possible that this result is specific to this particular test rig due to its relatively small transverse dimension. That is, it is expected that resonant transverse modes in this particular combustor (with a 15.24 cm height) would have a much higher frequency than the observed BVK heat release oscillations. Other confined, bluff body-stabilized combustion systems may produce a

vortex shedding frequency matching a resonant acoustic mode, which could lead to coupling between BVK-associated heat release oscillations and chamber acoustics. However, absolutely unstable flows do not typically respond to low levels of external forcing, so it is unclear whether or not BVK heat release oscillations can participate in a linear feedback loop with combustion chamber acoustics. This topic is outside the scope of the current research but should be addressed in a future study.

3.2 BVK Heat Release Dynamics with Close-coupled Fuel Injection

In this section, observed trends in BVK-associated heat release dynamics when close-coupled fuel injection was employed are discussed. This section is divided into two parts. First, the dependence of the BVK heat release oscillations upon the global equivalence ratio will be presented, as this was found to be the primary factor influencing the flame dynamics. The second part will describe additional factors observed to influence the heat release dynamics when close-coupled fuelling was used. Specifically, the influence of inlet gas temperature and velocity will be discussed.

3.2.1 Dependence upon Global Equivalence Ratio

The axial dependence of the BVK heat release oscillation amplitude was plotted for each operating condition using the 2D DFT method described in Section 2.2. Figure 3.4 shows examples of such plots, comparing flame dynamic amplitudes for varying Φ_{global} at a fixed inlet gas velocity and temperature (V_{in}=180 m/s and T=860°C) and flame holder geometry (4.75 cm vane). It can be seen that the heat release dynamics increased in amplitude with increasing global equivalence ratio for a fixed inlet velocity and temperature. This same general result was obtained for all incoming gas conditions (i.e., inlet velocity and temperature) and flame holder geometries, demonstrating the strong dependence of the BVK flame dynamics upon global equivalence ratio when close-

coupled fuel injection was employed. Recall that the amplitudes shown in Figure 3.4 have been normalized by the mean luminosity, so this result is not due to the increasing mean luminosity as more fuel was burned. Instead, the y-axis of Figure 3.4 is a measure of the transverse flame "movement" across the combustor (this is verified in Appendix B using flame edge tracking). The fuel jet penetration into the cross-flow (which increased with increasing Φ_{global} at a fixed V_{in}) and subsequent distribution in the reaction zone is believed to be the primary factor controlling the BVK heat release dynamics, which will be further analyzed in subsequent chapters.

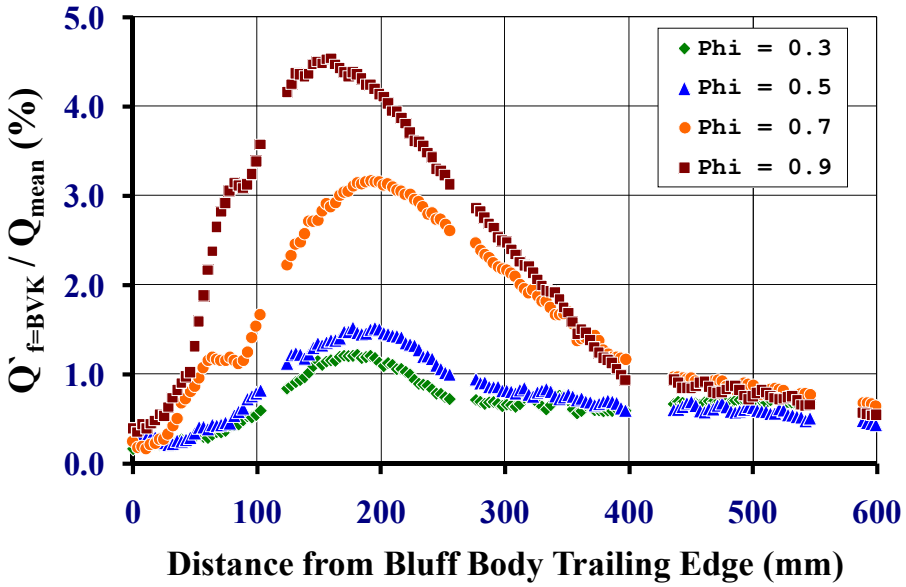

Figure 3.4: Axial distribution of the BVK heat release oscillation amplitude for varying Φ_{global} with close-coupled fuelling (V_{in}=180m/s, T_{in}=860°C, 4.75cm Vane).

Figure 3.4 shows that the axial distributions of the BVK heat release dynamic amplitudes were qualitatively similar for each global equivalence ratio (although the maximum amplitude increased with increasing Φ_{global}). For each operating condition, the amplitude increased with axial position before peaking at approximately 3-4 bluff body widths downstream of the trailing edge. Beyond this point, the amplitude of the

instability decayed likely due to several processes, including breakdown of the coherent vortical structures to finer-scale turbulence, gas expansion, and interactions of the coherent vortical structures with the combustor walls [46].

Maxima from plots like those in Figure 3.4 were used as a measure of the overall intensity of the BVK heat release oscillations for each operating condition. Figure 3.5 describes the dependence of these maxima upon global equivalence ratio for the 4.75 cm vane (left) and V-gutter (right). For each inlet gas condition and flame holder geometry, the overall intensity of BVK heat release oscillations did not vary considerably with Φ_{global} for $\Phi_{global} < 0.5$ but increased significantly with increasing global fuel-air ratio beyond this point. Operating conditions near globally rich blow out are marked "RBO" in Figure 3.5. It can be seen that heat release oscillations due to asymmetric vortex shedding were maximized just before blow out of the combustion process occurred. This result is similar to those of previous studies with premixed reactants in which asymmetric vortex shedding was demonstrated to be strong near lean and rich blow out [13-15, 31].

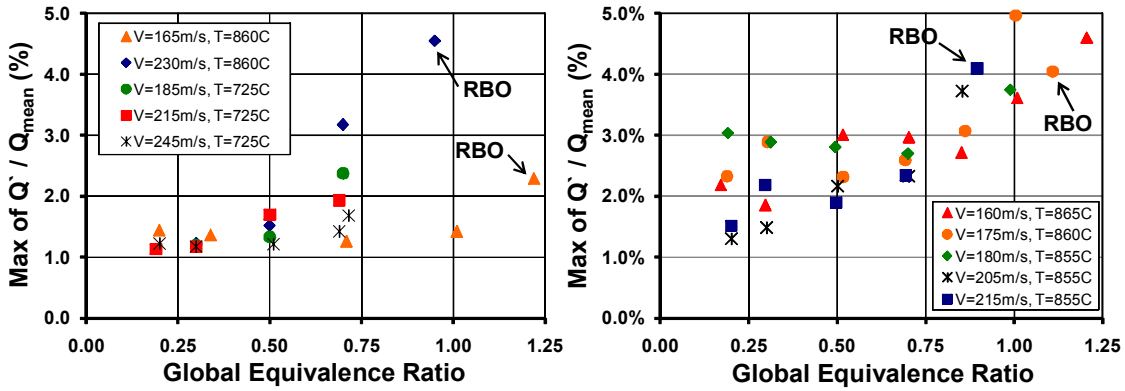

Figure 3.5: Maximum amplitude of BVK-associated heat release oscillations vs. global equivalence ratio for 4.75 cm Vane (left) and V-gutter (right).

However, the results of this study differ from those obtained in previous studies in that BVK-associated heat release oscillations were observed for most operating

conditions tested, not just those near blow out. This is attributed primarily to the high inlet temperatures that were tested, which resulted in significantly lower dilatation ratios (T_b/T_u) than in previous studies that employed room temperature reactants. For example, stoichiometric combustion of Jet-A with 1100K vitiated air (which also contains significant amounts of CO_2 and H_2O) results in an adiabatic flame temperature slightly more than twice the reactants temperature. Contrast this with combustion of hydrocarbon fuels with room temperature, non-vitiated air, which results in adiabatic flame temperatures no less than five times the reactants temperature, even when the equivalence ratio is near the lean extinction limit. Also, recall that the computations of Erickson et al. showed the BVK instability to appear in reacting flows when T_b/T_u dropped below two [34]. Thus, the occurrence of the BVK instability over a wide range of fuel-air ratios (as demonstrated in Figures 3.4-5) is not surprising.

The strong dependence upon global fuel-air ratio demonstrated in Figures 3.4 and 5 suggests that the fuel distribution in the reaction zone also strongly influences the BVK flame dynamics. This influence will be investigated further in Section 3.3 and Chapter 4.

3.2.2 Additional Factors Influencing Heat Release Dynamics

In addition to the global fuel-air ratio, the temperature and velocity of the inlet gas stream significantly influenced the BVK heat release dynamics when close-coupled fuel injection was used. In order to investigate the temperature dependence, the incoming gas temperature was reduced to 400°C by turning off the primary combustor, resulting in a significant increase in the global dilatation ratio, T_b/T_u. Figure 3.6 compares instantaneous frames extracted from high-speed movies of flame emission for inlet temperatures of 850 and 400°C, showing a dramatic difference in the flame structure. The image taken for the lower inlet temperature shows the flame stabilized in two distinct shear layers, whereas the image from the higher inlet temperature case clearly shows a sinuous flame structure, apparently caused by BVK vortex shedding. These images

suggest the changes in dilatation caused a transition in heat release dynamics from an absolutely unstable, asymmetric mode to a convectively unstable, symmetric mode.

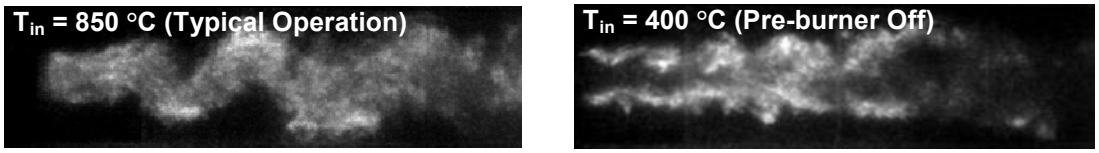

Figure 3.6: Comparison of instantaneous frames from high-speed movies recorded at T_{in}=850°C (left) and T_{in}=400°C (right), showing transition in vorticity from asymmetric to symmetric modes.

The approach velocities and fuel flow rates for the two images shown above were nearly the same (the global equivalence ratio differed due to the increase in oxygen concentration for the low temperature case). Therefore, the fuel penetration into the cross-flow and subsequent distribution in the reaction zone was likely similar between the two cases, as the penetration distance is proportional to the velocity ratio between the fuel and air streams [47]. Thus, it may be inferred that the difference in flame structure shown in Figure 3.6 was primarily caused by changes in dilatation due to the large difference in reactants temperature. This result is in agreement with the CFD simulations of Erickson et al. and the experiments of Emerson et al. which showed the BVK instability to grow in magnitude as T_b/T_u was reduced in premixed reacting flows [34-35].

The velocity of the incoming gas stream was also found to influence the BVK heat release dynamics when close-coupled fuel injection was used. Figure 3.7 compares axial distributions of BVK flame oscillations amplitude for varying inlet gas velocities at a fixed global equivalence ratio of Φ_{global}~0.64 (T_{in}~850°C, 4.75 cm vane). From the figure, it can be seen that the BVK flame fluctuations increased in magnitude with

increasing inlet velocity for a fixed fuel-air ratio. This result is in agreement with LES simulations of premixed bluff body-stabilized flames performed by Fureby, which showed that a sinuous flame structure was more likely at high approach velocities [48].

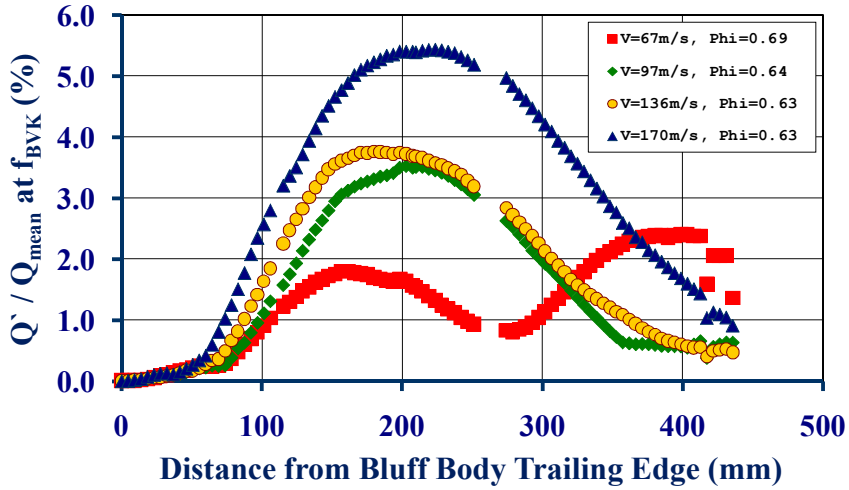

Figure 3.7: Dependence of BVK heat release oscillations amplitude upon inlet velocity with close-coupled fuel injection (Φ_{global}~0.64, T_{in}~850°C, 4.75 cm Vane).

The results presented thus far demonstrate the strong connection that exists between BVK flame dynamics and blow out of the combustion process. Figures 3.4 and 3.5 show that, for a fixed inlet gas velocity and temperature, the BVK heat release dynamics increased in amplitude with increasing global equivalence ratio (and thus, fuel jet penetration into the cross-flow) until blow out occurred. Similarly, Figure 3.7 shows that the BVK-associated flame dynamics increased in amplitude with increasing inlet velocity when the global fuel-air ratio was fixed. Though not shown, the flame dynamics were the strongest just before blow off occurred by increasing V_{in}. Thus, with close-coupled fuel injection, bluff body-stabilized reacting flows are most susceptible to BVK vortex shedding when operating near blow out. The amplitudes of such heat release oscillations will increase as this limit is approached, either by increasing the fuel flow

rate (i.e., Φ_{global}) or the inlet velocity. Note that premixed reacting wakes are also most susceptible to the BVK instability near blow out [13-15, 31].

3.3 Influence of Fuel Injection Mode

In the previous section, variations in fuel distribution in the reacting wake were postulated to be the primary reason the BVK heat release dynamics increased in amplitude with increasing global equivalence ratio. In order to investigate its dependence upon fuel-air mixing and subsequent distribution in the reaction zone, the BVK heat release dynamics were characterized and compared between close-coupled and upstream fuel injection modes at nearly-identical operating conditions. The 4.75 cm vane flame holder and the horizontal fuel bar configuration (see Fig. 2.3) were used for these tests.

Two approach velocities were tested: 125 and 150 m/s. The temperature of the incoming vitiated gas stream was approximately 815°C for each test. The global equivalence ratio was varied from 0.30 to 1.20 in increments of approximately 0.15 at each inlet velocity. For each increment of Φ_{global} the fuel injection location was switched between the upstream fuel bar and close-coupled fuel injectors, and the spatial and temporal heat release distributions were characterized at each Φ_{global} increment and fuel injection configuration (the stationary data will be shown in the next chapter). Alternating the fuel injection location at each Φ_{global} increment reduced the discrepancy in global operating conditions between the tests with different fuel injection modes, allowing for more accurate comparisons of the stationary and dynamic heat release.

Figure 3.8 compares high-speed images of flame emission obtained with the two fuel injection modes at Φ_{global}=0.61 and V_{in}=125 m/s. These images reveal distinct differences in flame structure. The combustion process was stabilized in two distinct, symmetric shear layers when the fuel was introduced upstream of the bluff body, as seen in the top image of Figure 3.8. These reacting shear layers persist with a very shallow

angle (practically horizontal) several bluff body widths downstream before minor perturbations are seen. The movie recorded with upstream fuel injection revealed the presence of sinuous flame oscillations (presumably due to BVK vortex shedding) only intermittently, with the majority of frames showing no clear evidence of BVK vortex-flame interactions.

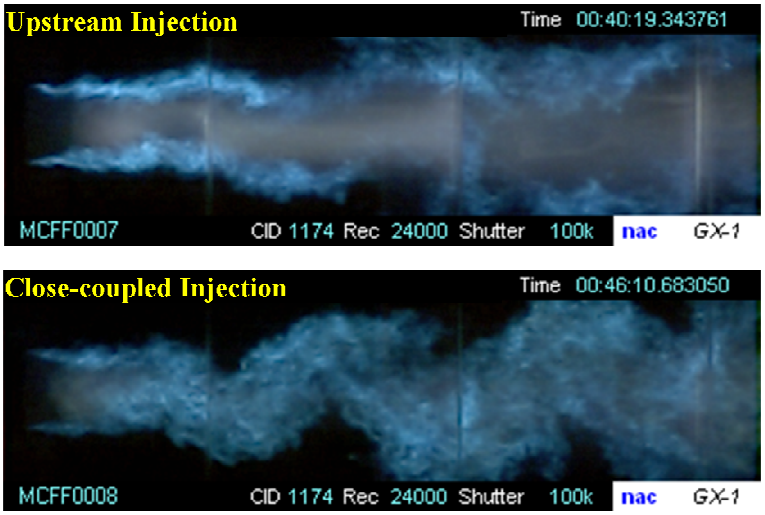

Figure 3.8: Comparison of high-speed movie frames recorded for upstream (top) and close-coupled (bottom) fuel injection at Φ_{global}=0.61 and V_{in}=125 m/s (4.75 cm Vane, T=815°C).

In contrast, the high-speed image obtained for close-coupled fuel injection (bottom image of Figure 3.8) shows clear evidence of heat release fluctuations due to von Kármán vortex shedding. A sinuous flame shape first appears approximately 2 bluff body widths downstream, and this undulating flame structure persists throughout the remainder of the camera field of view. These sinuous flame fluctuations were evident for almost the entire movie sequence.

Other key differences in flame structure can be seen in Figure 3.8. For upstream fuel injection, high intensity flame luminescence is observed in the near-wake shear

layers, indicating the presence of large combustion heat release there. However, the light intensity emitted from the near-wake region between the shear layers was low and had higher intensities in the red color component of the image than the blue component. This suggests that, in this case, practically all of the fuel reaching the shear layers was consumed there with practically no fuel burning in the recirculation zone. The lower intensity, gray light emitted between the shear layers was likely due to infrared emission from combustion products and broadband emission from thermal sources, such as soot.

In contrast, when close-coupled fueling was used, the reaction zone appeared distributed throughout the near-wake. The presence of blue flame luminescence just behind the bluff body (along the combustor centerline) could be due to a fraction of the fuel "bypassing" the shear layers and entering the recirculation zone, where it subsequently reacted. However, it could also be indicative of the flame sheets being wrapped around the large-scale, BVK vortical structures. Due to three-dimensional effects, oblique vortex shedding likely occurred [25]. The wrapping of the flame around such three-dimensional vortical structures would cause the blue flame luminescence to appear broadly distributed in such line-of-sight integrated images as those shown in Figure 3.8. Whether the centerline luminescence was due to fuel entrainment and subsequent burning in the wake or strong three-dimensional, spatio-temporal flame fluctuations should be investigated in future studies using planar imaging techniques.

While images such as those shown in Figure 3.8 provide qualitative information about instantaneous flame structures, more quantitative analyses of the BVK-associated heat release oscillations were performed using the previously described high-speed movie processing methodologies (see Section 2.2). The axial variation of the BVK heat release oscillation amplitude is plotted in Figure 3.9, comparing upstream and close-coupled fuel injection at Φ_{global}=0.61 and V_{in}=125 m/s (i.e., the cases corresponding to the movie frames shown in Figure 3.8). This figure shows that the BVK heat release dynamics were significantly higher in amplitude for close-coupled fuel injection than upstream

injection at this global equivalence ratio. The maximum amplitude for the close-coupled case was ~ 3.75% of the mean luminosity, which occurred at 178 mm downstream of the bluff body. In contrast, the upstream fuel injection case had maximum amplitude of 1.25% of the mean at x~127 mm. This shift in axial location of maximum intensity suggests that the BVK instability decayed earlier for the low-amplitude flame dynamics resulting from upstream fuel injection.

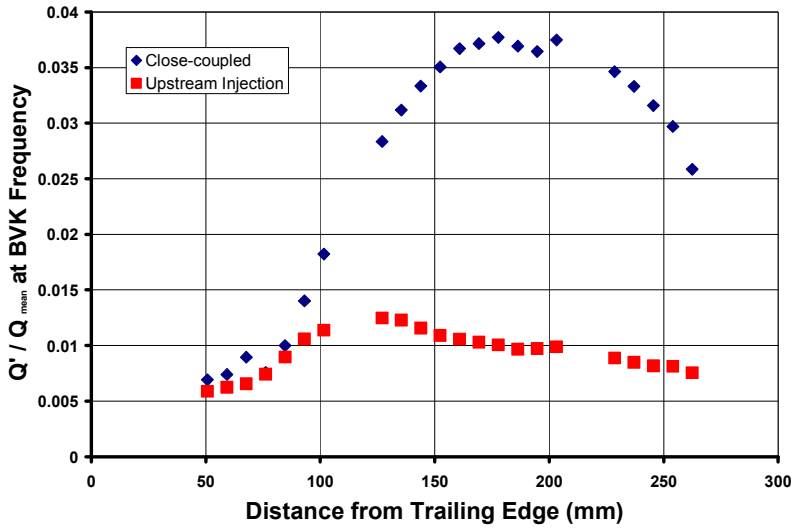

Figure 3.9: Axial variation of BVK heat release oscillation amplitude for Φ_{global}=0.61 and V_{in}=125 m/s, comparing fuel injection modes.

Flame luminosity power spectra taken at the axial locations of maximum intensity further reflect the strong differences in BVK heat release dynamics between the two fuel injection modes, see Figure 3.10. Upstream fuel injection at Φ_{global}=0.61 resulted in a coherent peak in the resulting power spectrum at ~ 1000 Hz, but its amplitude was small, being only a few times greater than the background noise. In contrast, close-coupled fuelling at the same global equivalence ratio resulted in a well-pronounced peak at the BVK frequency (961 Hz) many times greater than the background. These differences in flame dynamics demonstrate the strong dependence of the BVK instability upon the

mode of fuel injection, and therefore, the manner in which the fuel-air ratio is spatially distributed in the reaction zone.

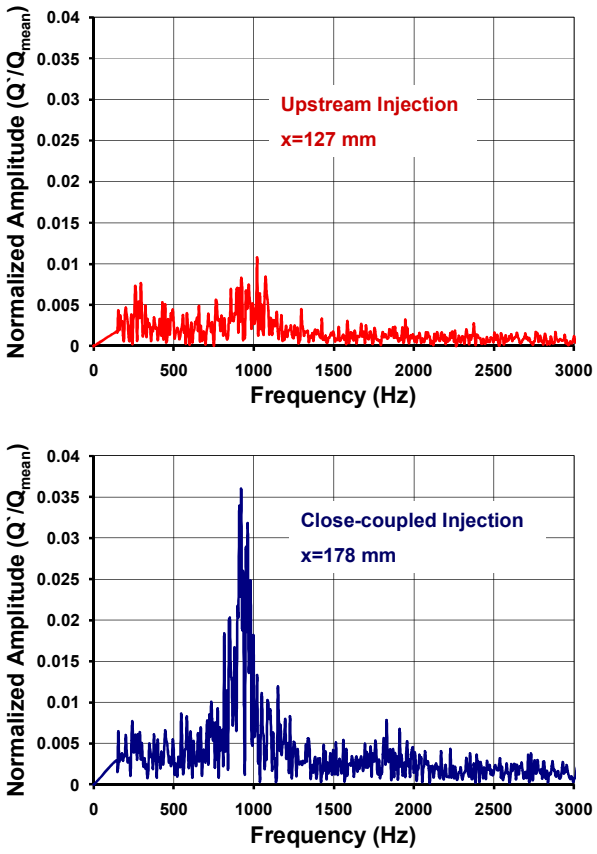

Figure 3.10: Flame luminosity spectra extracted from the maxima of Figure 3.9, comparing upstream (top) and close-coupled (bottom) fuel injection modes.

Maxima from plots like those in Figure 3.9 were used in this study as a measure of the overall intensity of BVK heat release oscillations for each operating condition. Figure 3.11 plots these maxima versus global equivalence ratio (along with best-fit trend lines), comparing the two fuel injection modes. This graph shows that heat release oscillations due to BVK vortex shedding were significantly higher in amplitude for close-coupled fuel injection than for upstream injection for all but the leanest global equivalence ratio. Figure 3.11 shows that the intensity of BVK-associated heat release

oscillations increased with increasing global equivalence ratio for close-coupled fuel injection, reaching a maximum just before globally rich blow out of the combustion process, which occurred at $\Phi_{global} \sim 1.25$ for this inlet velocity. At this condition, the spectral amplitude at the BVK frequency was very high, exceeding 7% of the mean luminosity.

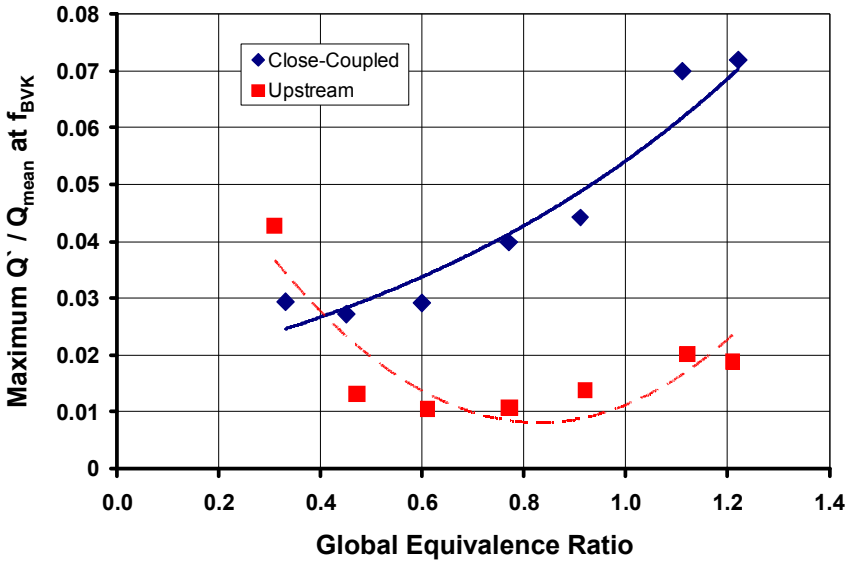

Figure 3.11: Maxima of BVK heat release oscillation amplitudes vs. global equivalence ratio, comparing fuel injection modes (V_{in}=125 m/s, T_{in}~815°C).

The dynamics resulting from upstream fuel injection exhibited different trends, with the highest intensities occurring for overall lean and rich operation. The BVK flame dynamics were practically negligible in the middle of the operating range (i.e., $0.5<\Phi_{global}<1.0$). Some possible reasons for this trend are discussed in the next chapter. For now, it is worth noting that BVK heat release oscillations were particularly strong (~4.5% of mean luminosity) near lean blow out (i.e., $\Phi_{global}=0.31$) when the fuel was introduced well upstream of the bluff body. This result is in agreement with previous

studies of premixed bluff body-stabilized flames which demonstrated vortex shedding to be prominent near lean blow out [13-15]. It is worth noting that rich blow out did not occur for upstream fuel injection at the highest global equivalence ratio tested: Φ_{global}=1.25. Thus, it is unknown whether or not the BVK flame dynamics would be particularly strong near rich blow out with upstream fuel injection, as they were near lean blow out. This should be investigated in future studies.

Figure 3.11 demonstrates that large differences in BVK flame dynamics can occur by altering the mode and location of the fuel injection, even if the global flow conditions are identical. For example, a drastic difference in dynamic amplitude between fuel injection modes occurred at a global equivalence ratio of 1.1. Close-coupled fuelling resulted in strong BVK-associated heat release oscillations, with a spectral amplitude exceeding 7% of the mean luminosity. When the fuel was introduced upstream of the bluff body, the amplitude reduced to 2% of the mean. If only global properties were considered, the two cases would have similar global dilatation ratios (T_b/T_u~2.0), a parameter that has been strongly correlated to the intensity of vortex shedding in reacting bluff body wakes [34-35]. Yet, Figure 3.11 shows that drastic differences in flame dynamics occurred for a "globally identical" dilatation ratio.

Based on the discussion above, global flow conditions alone do not adequately describe the fundamental processes controlling asymmetric vortex shedding in reacting bluff body wakes. Instead, it is believed that local properties must be considered. Large differences in fuel and heat release distribution in the reaction zone likely occurred between the two fuel injection modes, which are believed to be the primary reason for the observed differences in flame dynamics. The spatial distributions of fuel-air ratio and heat release will be described in the next chapter, and their influence on the BVK flame dynamics will be examined.

CHAPTER 4

SPATIAL HEAT RELEASE AND FUEL-AIR RATIO DISTRIBUTIONS

Two key observations were described in the previous chapter. First, the amplitude of BVK-associated heat release oscillations increased with increasing global equivalence ratio when close-coupled fuel injection was used. Second, this amplitude was significantly reduced by introducing the fuel well upstream of the flame holder. These results indicate that the manner in which the fuel is introduced and distributed in the reaction zone strongly influences the BVK flame dynamics.

In order to investigate this further, time-averaged spatial distributions of heat release and fuel-air ratio were characterized using the chemiluminescence imaging system described in Section 2.3. This chapter describes the results of these measurements and is divided into four sections. The dependence of the spatial heat release and fuel-air ratio distributions upon global equivalence ratio with close-coupled fuel injection is described in Section 4.1. This section will also provide insight into the fundamental processes controlling blow out in close-coupled-fuelled systems. Section 4.2 compares the results obtained for close-coupled fuel injection to those obtained with upstream fuel injection in order to determine the dependence of the heat release and equivalence ratio distributions upon the fuel injection mode. The chemiluminescence data is then used to estimate local equivalence ratio and products gas temperatures in section 4.3, with emphasis on estimating these quantities in the near-wake reaction zone. These estimates will be compared to Large Eddy Simulations (LES) performed in a separate study. Finally, Section 4.4 compares the measured flame dynamic amplitudes to time-averaged spatial distributions of heat release, equivalence ratio, and estimated near-

wake gas temperatures in order to identify the fundamental processes controlling the BVK instability in reacting bluff body wakes.

4.1 Heat Release and Equivalence Ratio Distributions with Close-coupled Fuel Injection

Figure 4.1 compares time-averaged CH* (left) and C_2*/CH* (right) distributions for varying Φ_{global} with close-coupled fuel injection. Also shown (on the far left) are images of the fuel spray recorded by a 30 Hz camera. These images were taken at a constant inlet velocity and temperature (i.e., V_{in}=180 m/s and T=860°C) using the 4.75 cm vane flame holder (see Figure 2.2). The left edges of the chemiluminescence images in Figure 4.1 coincide with the bluff body trailing edge. False color maps were applied to the images to facilitate visual comparisons of the heat release and fuel-air ratio distributions, the palettes of which are shown in the figure.

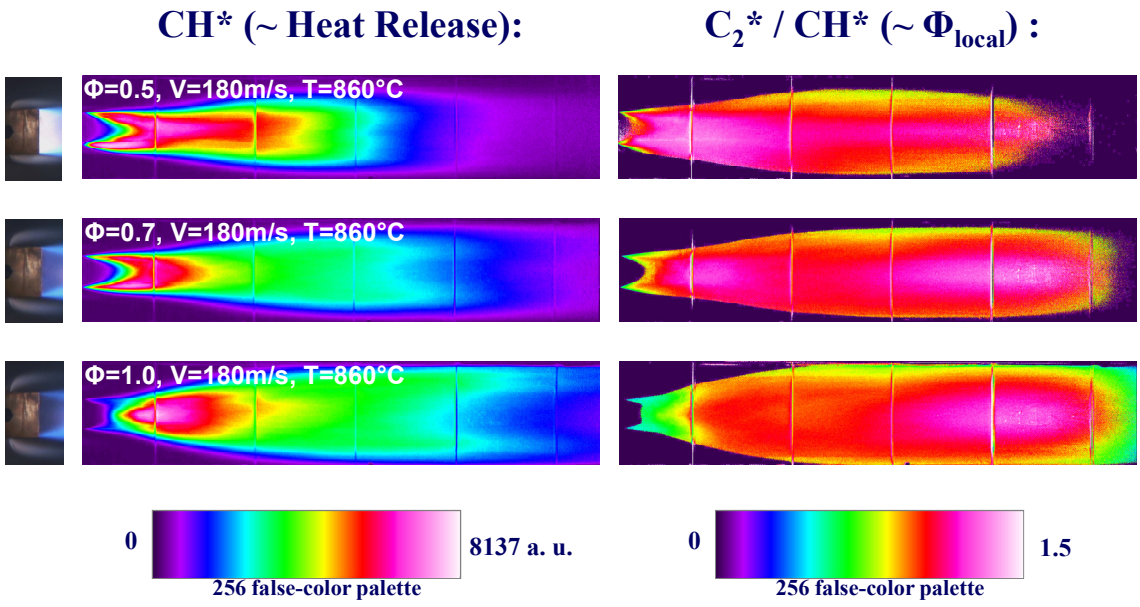

Figure 4.1: CH* (left) and C_2*/CH* (right) images for varying global equivalence ratio with close-coupled fuel injection. Fuel spray images also shown (far left).

Comparing the CH* images of Figure 4.1, it can be seen that the biggest differences in spatial heat release distribution occurred in the near-wake shear layers as Φ_{global} was varied. Operation at low to moderate global fuel-air ratios resulted in large amounts of heat release in the shear layers surrounding the recirculation zone, as shown in the CH* image for Φ_{global}=0.5. This is attributed to the relatively low fuel spray penetration into the cross-flowing gas stream (due to the low fuel jet to cross-flow momentum flux ratio), resulting in strong fuel entrainment into the near-wake. This can be seen in the instantaneous fuel spray image corresponding to Φ_{global}=0.5, which shows low fuel jet penetration and a luminous wake due to fuel entrainment and subsequent burning in the recirculation zone.

As the fuel flow rate and momentum flux ratio were increased, the fuel jet penetrated further into the cross-flow, and less fuel was entrained into the near-wake shear layers. Consequently, the amount of heat release occurring in the shear layers reduced as Φ_{global} was increased. However, the CH* images indicate that more fuel was entrained and burned along the near-wake centerline at high Φ_{global}. This can be seen by comparing the CH* images in Figure 4.1, which shows that the CH* intensity along the centerline was higher for Φ_{global}=1.0 than Φ_{global}=0.7. In addition, note that most of the fuel was burned in the far-wake for high Φ_{global} operation, in contrast to the lower Φ_{global} cases where substantial amounts of heat release occurred in the near-wake.

The C_2*/CH* images of Figure 4.1 show that the biggest differences in local equivalence ratio also occurred in the near-wake (i.e., at x<2W), which became progressively leaner as the overall fuel-air ratio, and therefore the fuel spray penetration, was increased. Interestingly, the local equivalence ratio at locations further downstream (i.e., x>2W) did not vary significantly as the global equivalence ratio was increased. This result will be described more quantitatively in the next section.

The images of Figure 4.1 also provide insight into the physical processes controlling the static stability of bluff body-stabilized combustors employing close-

coupled fuel injection. As the global equivalence ratio was increased, both the heat release and local equivalence ratio in the near-wake decreased as the fuel jets penetrated further into the cross-flow. Yet, sufficient amounts of fuel were still supplied to the shear layers by the small droplets stripped from the fuel jets by aerodynamic shear, where they reacted and anchored the flame to the bluff body. As the fuel flow rate was further increased, insufficient amounts of fuel were entrained into the near-wake shear layers, and blow out occurred. For the inlet gas velocity and temperature shown in Figure 4.1, blow out occurred at Φ_{global}=1.05. While this extinction event may be considered a rich blow out in a global sense, the C_2*/CH images of Figure 4.1 show that the local equivalence ratio in the near-wake was significantly leaner than the other global fuel-air ratios. Consequently, it is presumed that globally rich blow out in bluff body-stabilized combustion processes that use close-coupled fuelling is caused by local lean blow out in the near-wake reaction zone. This postulate will be investigated further in Section 4.3.

4.2 Influence of Fuel Injection Mode

4.2.1 CH* Distributions

Spatial heat release and fuel-air ratio distributions were also characterized for fuel injection occurring upstream of the bluff body (see Fig. 2.3 for configurations). Examples of CH* chemiluminescence images are shown in Figure 4.2, comparing results obtained for upstream fuel injection (using the horizontal fuel bar configuration) to those obtained for close-coupled fuel injection for three global equivalence ratios: 0.31, 0.61 and 0.92. All images shown were taken at an inlet velocity of 125 m/s. Figure 4.2 reveals notable differences in spatial heat release distributions between the two fuel injection modes. For example, upstream fuel injection typically resulted in stronger CH* intensities in the near-wake shear layers than close-coupled fuelling. This is most evident

by comparing the CH* images at Φ_{global}=0.61. However, the intensity of light emitted by CH* radicals is a strong function of equivalence ratio [39, 42], and it is unclear how much of the differences in CH* intensity were due to local equivalence ratio variations and how much were due to increases in fuel entrainment and subsequent burning.

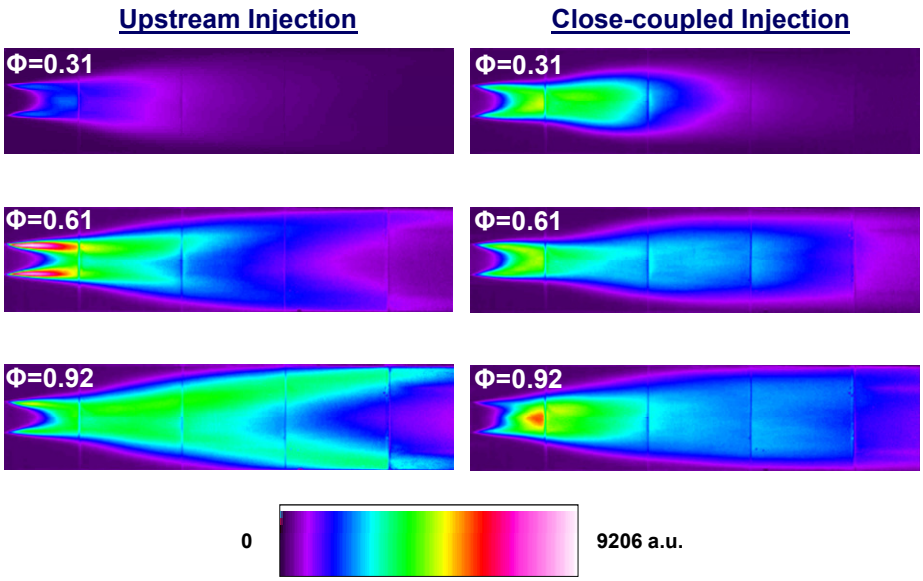

Figure 4.2: Comparison of CH* images between upstream (left) and close-coupled (right) fuel injection modes for varying global equivalence ratio (V=125m/s, T=815°C, 4.75 cm Vane).

In order to provide more quantitative comparisons of near-wake heat release between fuel injection modes, the CH* intensity was integrated along the first two bluff body widths downstream of the trailing edge. This control volume was chosen for analysis because the local combustion processes in this region were believed to strongly influence the static and dynamic stability of the overall combustion process (e.g., see the discussion at the end of §4.1). Figure 4.3 outlines the area of integration for these comparisons. The left edge of the rectangular area shown in Figure 4.3 coincides with the bluff body trailing edge, and its height extends the entire transverse dimension of the

combustor. This area was used for all subsequent analyses of near-wake heat release and local equivalence ratio in this thesis.

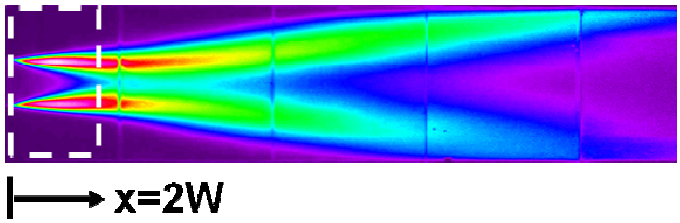

Figure 4.3: Area of integration for near-wake heat release evaluation.

Transverse profiles of the near-wake heat release were obtained by integrating the CH* intensity across the width (i.e., in the axial direction) of the region shown in Figure 4.3. Examples of these profiles are shown in Figure 4.4, comparing upstream and close-coupled fuel injection modes at Φ_{global}=0.77. From this plot, it can be seen that the near-wake heat release was significantly higher (approximately 54%) for upstream fuel injection than its close-coupled counterpart at this global equivalence ratio. Note the large difference in CH* intensity which occurred in the shear layers surrounding the recirculation zone. This disparity reflects the differences in fuel-air mixing, entrainment, and subsequent reaction in the near-wake between the fuel injection modes.

The large variation in near-wake CH* intensity shown in Figure 4.4 also reflects the differences in flame structure between the fuel injection modes. When the fuel was introduced well upstream of the bluff body, it had sufficient time to evaporate and mix with the incoming vitiated gas stream prior to burning. In fact, it is likely that the mixture was fully vaporized by the time it reached the reaction zone, as autoignition occurred upstream of the bluff body trailing edge when the inlet air temperature was increased by ~15°C. This enhanced fuel vaporization and the distribution of injection points along the combustor span likely resulted in a nearly uniform fuel distribution

across the span-wise coordinate by the time the reactants reached the wake. The resulting mixture is believed to have burned as a premixed flame which extended the span of the combustor, as illustrated in the cartoon of Figure 4.5b.

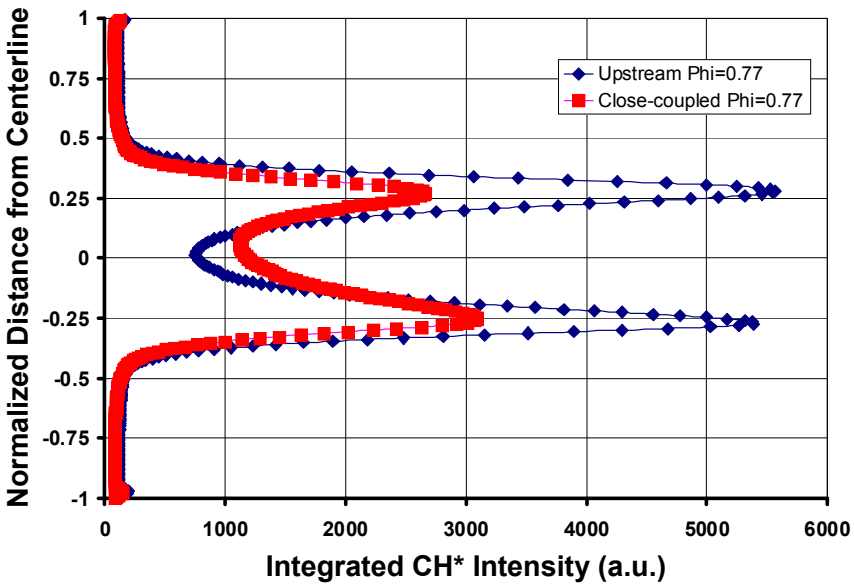

Figure 4.4: Transverse CH* intensity profiles integrated along the first two bluff body widths downstream of the trailing edge, comparing upstream and close-coupled fuel injection modes at Φ_{global}=0.77 (V=125m/s, T=815°C).

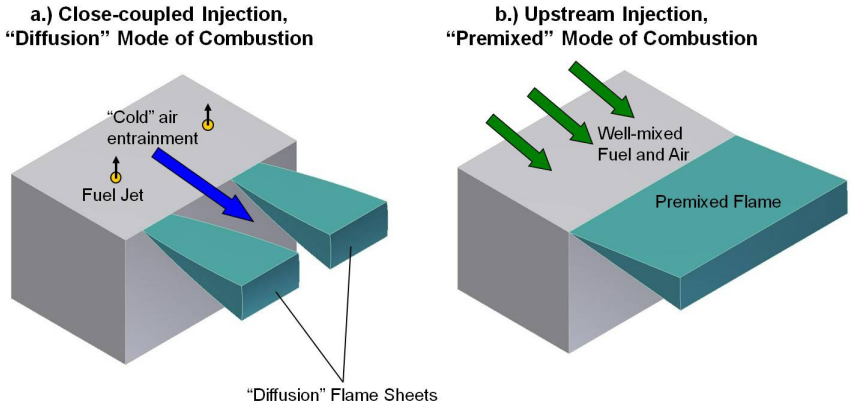

Figure 4.5: Illustration of hypothesized near-wake flame structures for (a.) close-coupled and (b.) upstream fuel injection.

In contrast, close-coupled fuel injection provided little time for the fuel to mix with the vitiated air stream before burning, due to the proximity of the injection points to the reaction zone. This, along with the use of only two injectors on either side of the flame holder, resulted in a non-uniform fuel distribution across the combustor span in the near-wake. The span-wise dispersion of droplets emanating from each orifice is estimated to have been approximately 1.25 cm by the time the fuel reached the bluff body trailing edge, based on empirical correlations given in [47]. Consequently, it is believed that combustion occurred in two distinct reaction zones (or "flame sheets") anchored to the bluff body trailing edge, as illustrated in Figure 4.5a. The "broken" reaction zone illustrated in Figure 4.5a would have allowed for passage of unburned vitiated air between the flame sheets and into the recirculation zone. Further downstream, it is likely these flame sheets merged and the fuel was fully vaporized and dispersed across the combustor span, producing a reaction zone that extended across the combustor span.

The differences in reaction zone distributions illustrated in Figure 4.5 would partially explain the large disparities in near-wake CH* intensity that were observed between the two fuel injection configurations (see Figure 4.4), as the line-of-sight integrated flame emission would have been higher for the upstream fuel injection flame if it extended the entire span of the combustor. Other factors likely to have contributed to the differences in heat release distributions become more evident when the remainder of the combustor (i.e., x>2W) is considered. Figure 4.6 plots axial distributions of the CH* intensity integrated in the transverse direction, comparing heat release distributions between the two fuel injection modes at two global equivalence ratios: 0.31 and 0.92. This figure demonstrates the strong dependence of the CH* distribution upon global equivalence ratio and fuel injection mode. For Φ_{global}=0.31, the CH* intensity resulting from close-coupled fuel injection was much higher than the "premixed" case. This will be shown, in the next section, to be due to the large differences in local equivalence ratios between the two fuel injection modes at this Φ_{global} value. In contrast, for Φ_{global}=0.92,

the upstream fuel injection case had higher CH* intensities than close-coupled fuel injection for all axial locations.

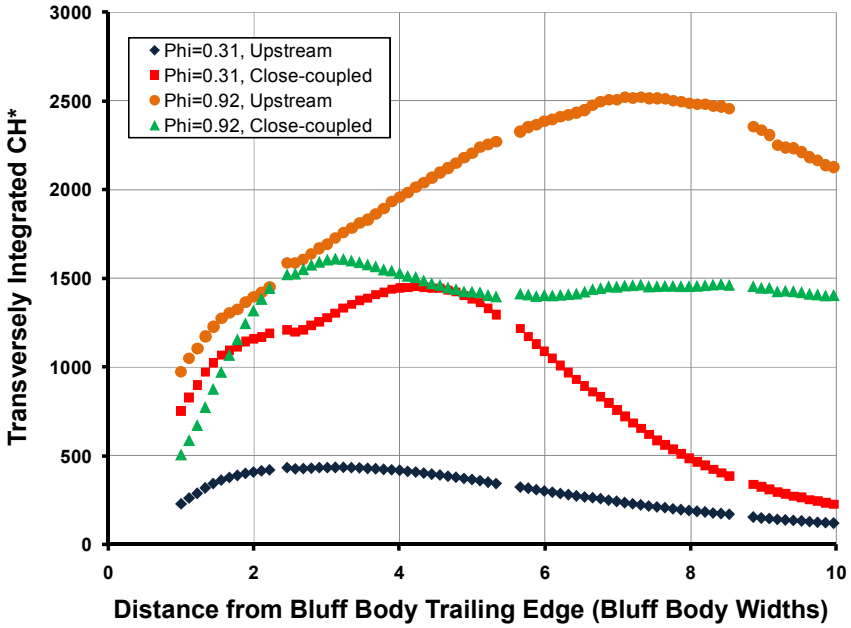

Figure 4.6: Axial variation of the transversely integrated CH* intensity, comparing close-coupled and upstream fuel injection modes at Φ_{global} = 0.31 and 0.92.

The dependence of the heat release distribution upon fuel injection mode becomes more evident by integrating the total CH* intensity throughout the reacting wake, which is plotted as a function of global equivalence ratio in Figure 4.7 for the two fuel injection modes. With the exception of the two leanest global equivalence ratios, fuel injection upstream of the bluff body resulted in a greater overall CH* intensity than close-coupled injection at identical operating conditions. This is attributed primarily to an increase in combustion efficiency due to the fuel being vaporized and well-mixed prior to burning for upstream injection, whereas the combustion process was limited by fuel-air mixing for close-coupled fuelling. However, the integrated CH* intensities for Φ_{global}=0.31 and 0.45 with upstream fuel injection were lower than their close-coupled counterparts, which will be shown to be due to differences in local equivalence ratio in the next section.

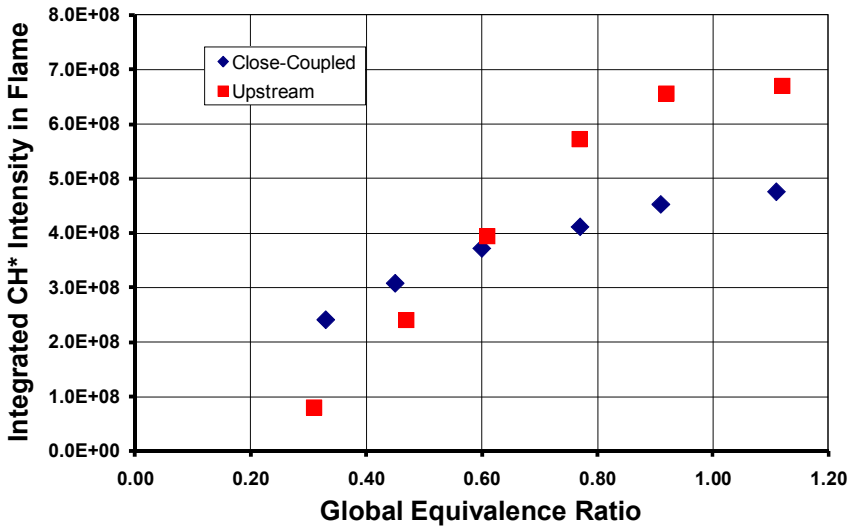

Figure 4.7: Integrated CH* intensity vs. global equivalence ratio, comparing upstream (horizontal fuel bar) and close-coupled fuel injection.

4.2.2 C_2*/CH* Distributions

Figure 4.8 compares C_2*/CH* images obtained for fuel injection upstream of the bluff body (left) to those obtained for close-coupled injection (right) for the same operating conditions presented in Figure 4.2. These images indicate that significant differences in local equivalence ratio distributions occurred between the two fuel injection modes. For fuel injection upstream of the bluff body, the C_2*/CH* values increased throughout the reaction zone with increasing Φ_{global}, as is expected when the fuel is well-mixed prior to burning [43-44]. However, the C_2*/CH* distribution became more non-uniform as the global equivalence ratio was increased. This is most evident in the Φ_{global}=0.92 image, where a pocket of high C_2*/CH* ratios occurred in the near-wake, whereas further downstream the mixture appears to have burned at leaner local fuel-air ratios. The high C_2*/CH* value in the near-wake is believed to be the result of locally rich combustion due to non-uniform fuel-air mixing. Due to the fuel bar being positioned along the combustor centerline, the local equivalence ratio approaching the bluff body

likely varied in the transverse direction, being richer near the centerline and leaner near the top and bottom walls. Thus, the locally rich reactants near the centerline are believed to have been entrained in the near-wake, whereas the leaner reactants near the walls convected further downstream, burning in the far-wake.

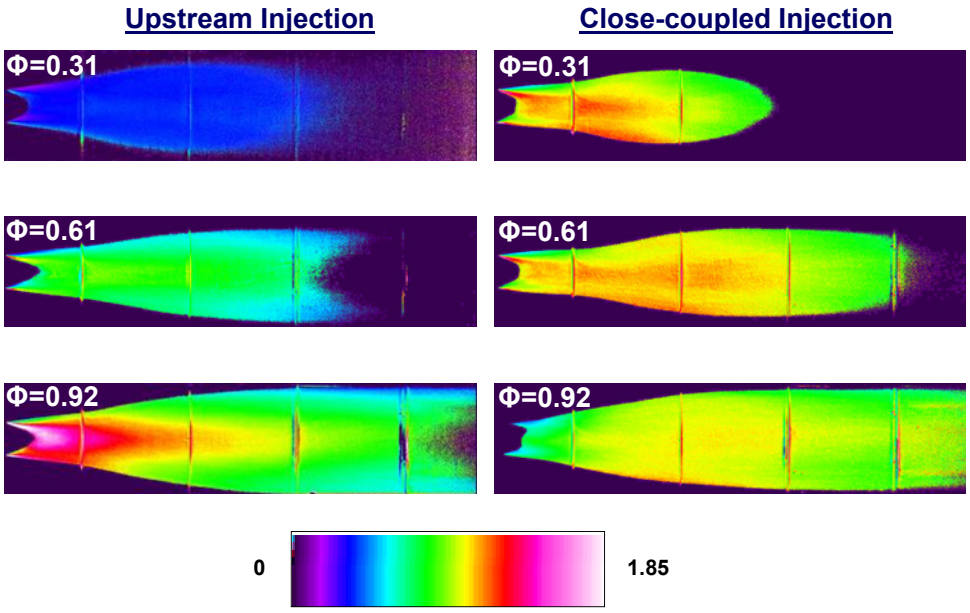

Figure 4.8: Comparison of C_2*/CH* images between upstream (left) and close-coupled (right) fuel injection modes for varying global equivalence ratio.

In order to verify the cause of the C_2*/CH* non-uniformities described above, chemiluminescence images were taken with the vertical fuel bar configuration installed (see Fig. 2.3). With this configuration, the fuel distribution was likely more uniform in the transverse direction due to the injectors being evenly distributed along the combustor height. Figure 4.9 compares C_2*/CH* distributions between the two upstream fuel injection configurations (i.e., horizontal vs. vertical fuel bars) at nearly identical operating conditions (Φ~0.84, V_{in}=220m/s, T~825°C). This figure shows that the spatial equivalence ratio distribution was more uniform for the vertical fuel bar configuration, which is attributed to more uniform fuel-air mixing prior to combustion. Hence, the high

C_2*/CH* ratio in the near-wake with the horizontal fuel bar configuration was, in all likelihood, due to locally rich combustion.

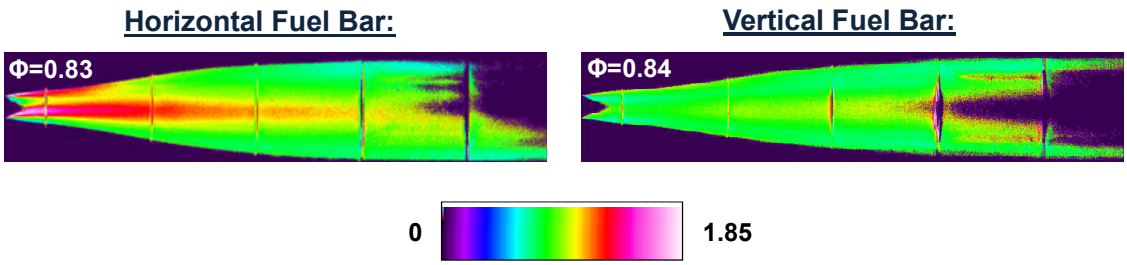

Figure 4.9: C_2*/CH* images with upstream fuel injection at Φ~0.84, comparing horizontal (left) and vertical (right) fuel bar configurations.

The spatial C_2*/CH* distributions varied less with Φ_{global} for close-coupled fuel injection than upstream fuel injection. This is demonstrated in Figure 4.10, which plots the axial distributions of the transversely integrated C_2*/CH* ratio for the two fuel injection modes at two global equivalence ratios: 0.31 and 0.92. This figure shows that, for close-coupled fuel injection, the C_2*/CH* ratio in the first two bluff body widths downstream of the trailing edge was higher for Φ_{global}=0.31 than Φ_{global}=0.92, due to the differences in fuel penetration and entrainment (see the discussion in §4.1). Further downstream, the transversely integrated C_2*/CH* ratios became more similar, having the same value at approximately five bluff body widths downstream. Beyond this point, the C_2*/CH* ratios were higher for Φ_{global}=0.92 than Φ_{global}=0.31. In contrast, when the fuel was introduced upstream of the bluff body, the C_2*/CH* values for Φ_{global}=0.92 were more than twice those of Φ_{global}=0.31 at all axial locations, as shown in Figure 4.10.

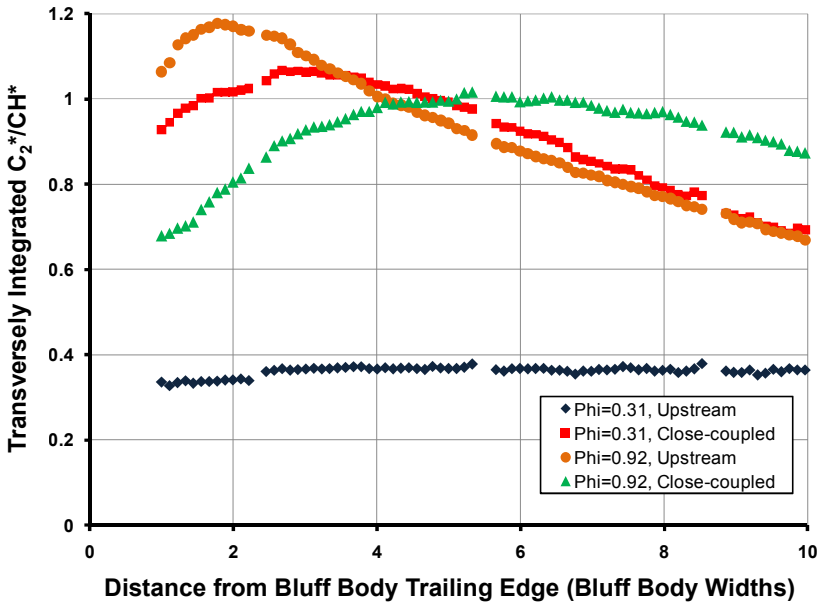

Figure 4.10: Axial distribution of the transversely integrated C_2*/CH* ratio, comparing close-coupled and upstream fuel injection modes at Φ_{global} = 0.31 and 0.92.

In order to provide more quantitative comparisons, the average C_2*/CH* value in the reaction zone was calculated for each global fuel-air ratio and fuel injection configuration. The procedure for determining this value was as follows. First, the original CH* and C_2* images were filtered by setting any pixel intensity less than a threshold value to zero. The threshold for each image was chosen to be 10% of its maximum pixel intensity (thus varying between images due to differences in overall luminosity). Next, the filtered C_2* image was divided by the filtered CH* image, and the resulting C_2*/CH* pixels were summed throughout the image (if CH*=0 at a particular pixel after applying the threshold, C_2*/CH* was set to zero at that location). Finally, this sum was divided by the number of pixels in the filtered image with nonzero C_2*/CH* values. The result was the average C_2*/CH* value in the reaction zone which did not include contributions from locations in which the chemiluminescence signal was low (e.g., the recirculation zone). In addition to spatial averaging, the integrated C_2* signal was divided by the integrated CH* signal (without filtering) for each operating condition.

These integrated C_2*/CH* values were approximately equal to the spatially-averaged values for all operating conditions, so only the spatial averages will be presented here.

Spatially-averaged C_2*/CH* values are plotted as a function of global equivalence ratio in Figure 4.11, comparing close-coupled fuel injection to upstream injection with both fuel bar configurations – vertical and horizontal. The data shown in Figure 4.11 were obtained for two vane widths over a range of inlet velocities. Interestingly, the average C_2*/CH* value increased linearly with increasing global equivalence ratio when the fuel was injected upstream of the bluff body. Furthermore, these values did not vary considerably when the incoming velocity, bluff body width, or fuel bar configuration were changed, further supporting the use of C_2*/CH* as an indicator of equivalence ratio in hydrocarbon flames. A linear trend fitted to the data obtained with the vertical fuel bar configuration is shown in Figure 4.11, and it can be seen that the other upstream fuel injection data points fall near this line. The vertical fuel bar data was chosen because it was believed to have the most uniform fuel-air ratio distribution in the reactants stream and, therefore, better approximated premixed combustion. It is worth noting that Morrell et al. also report a linear increase in integrated C_2*/CH* values with increasing equivalence ratio for a liquid-fuelled (n-heptane) swirl-stabilized flame [40], and Roby et al. found CH*/OH* to increase linearly with equivalence ratio in the range $0.6<\Phi<1.1$ for turbulent premixed (gaseous) flames [49].

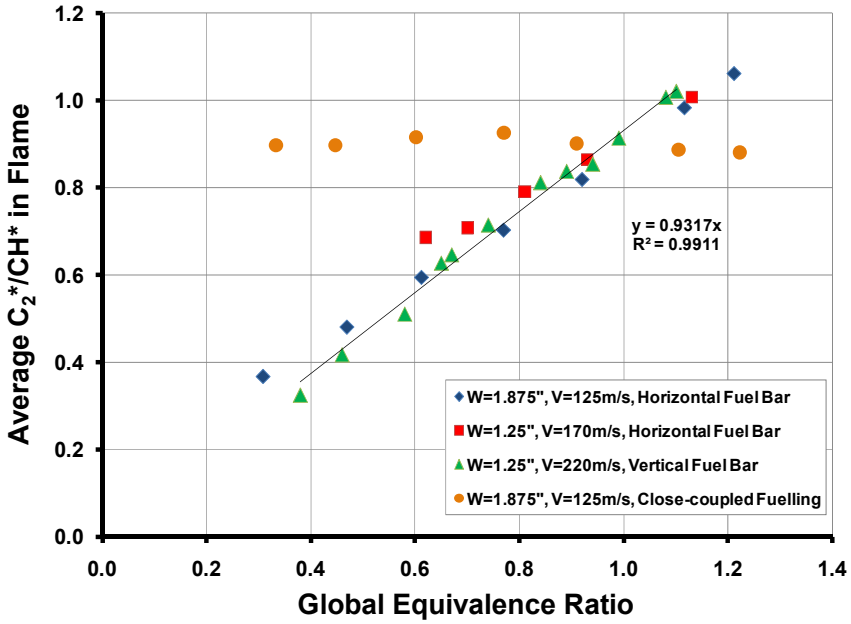

Figure 4.11: Spatially-averaged C_2*/CH* in the flame vs. global equivalence ratio.

The linear dependency of the spatially-averaged C_2*/CH* value upon global fuel-air ratio with upstream fuel injection supports the use of C_2*/CH* as an indicator of equivalence ratio in combustion of Jet-A with air. Furthermore, it suggests that C_2*/CH* measurements can be calibrated to yield quantitative values of Φ_{local} for combustion of Jet-A with vitiated air. Additional work is needed to verify the latter statement, and it is believed that such a calibration would be specific to the situation being investigated. That is, it is believed to depend upon additional factors such as vitiation levels, dilution and/or product recirculation, and the diagnostic system utilized [40, 49]. However, if successful, such a calibration would provide a key tool for researchers and designers of practical combustion systems, as estimates of the local fuel-air ratio could be obtained by measuring naturally-occurring flame radiation.

Since the fuel was likely fully evaporated and well-mixed with the vitiated gas stream prior to burning, it is believed that the spatially-averaged C_2*/CH* values obtained for upstream fuel injection are nearly the same as that which would be measured

if the reactants were perfectly premixed. Thus, it is believed that the linear trend shown in Figure 4.11 can be used to quantitatively estimate values of Φ_{local} in cases in which the fuel-air ratio distribution was spatially stratified or non-uniform. Such estimates will be presented in the next section for close-coupled-fuelled flames.

Contrary to upstream fuel injection, the spatially-averaged C_2*/CH* values resulting from close-coupled fuel injection were nearly the same for all global equivalence ratios. Figure 4.11 shows only slight variation in this value with varying Φ_{global}. Though not shown, similar values were obtained for varying inlet velocity and flame holder width. What is of greater interest, however, is that this approximately constant average C_2*/CH* value equaled the same value obtained when the fuel was injected upstream of the flame holder at globally stoichiometric conditions. This result strongly suggests that the combustion occurred, on average, in stoichiometric flamelets locally when close-coupled fueling was used. One plausible hypothesis is that the liquid fuel jets produced clouds of droplets that were dispersed throughout the combustor and mostly burned in stoichiometric diffusion flames. However, in this case the reaction is believed to have been controlled primarily by turbulent mixing of the evaporated fuel with the vitiated air stream, whereas classical diffusion flames are controlled by mass diffusion [50]. Though Figures 4.1, 4.8 and 4.10 clearly show significant variations in Φ_{local} in the near-wake with varying global fuel-air ratio, it appears that the rest of the mixture burned, on average, at nearly-stoichiometric local equivalence ratios.

4.3 Estimations of Near-wake Equivalence Ratio and Temperature

Spatial variations in fuel-air ratio and heat release occurred in the reacting wake (most notably in the near-wake reaction zone) when close-coupled fuel injection was used. While it is difficult to measure three-dimensional distributions of local equivalence ratio, the C_2*/CH* measurements performed when the fuel was introduced well-upstream

of the bluff body provided a means to estimate the line-of-sight averaged local equivalence ratio at any point in the reaction zone. This was done using the line fitted to the "premixed" data in Figure 4.11 to estimate quantitative values of the span-wise and time-averaged local equivalence ratio based on the measured C_2*/CH* ratio. Of particular interest in this study was the local equivalence ratio in the near-wake reaction zone, since it was believed to strongly influence the static and dynamic stability of the combustion process.

The average C_2*/CH* value in the first two bluff body widths of the reacting wake (see Figure 4.3 for integration area) was evaluated for each operating condition. Upon computing this average, the threshold described in Section 4.2.2 was applied; i.e., pixels with CH* and/or C_2* intensities less than 10% of the image maximum were not considered. The resulting value was the average C_2*/CH* in the near-wake reaction zone which did not consider regions with little to no flame emission. This value was divided by the slope of the trend line shown in Figure 4.11 to obtain a quantitative estimate of the local equivalence ratio in the near-wake.

Estimated time-averaged near-wake equivalence ratios are plotted as a function of global equivalence ratio for close-coupled-fuelled flames in Figure 4.12, comparing results obtained for two inlet velocities: 125 and 185 m/s. This figure suggests that the near-wake mixture burned, on average, at near stoichiometric fuel-air ratios when the global equivalence ratio was relatively low ($0.20<\Phi_{global}<0.50$), regardless of the inlet velocity. As discussed in Section 4.1, this is attributed to robust fuel entrainment into the near-wake due to the low fuel spray penetration into the cross-flow. As the global equivalence ratio increased, the fuel spray penetrated further into the cross-flow, less fuel was entrained into the near-wake, and the local equivalence ratio became progressively leaner until blow out occurred. Figure 4.12 shows that the rate at which the near-wake equivalence ratio became leaner depended upon the inlet velocity, with higher inlet velocities experiencing a more rapid "leaning" of the near-wake with increasing Φ_{global}.

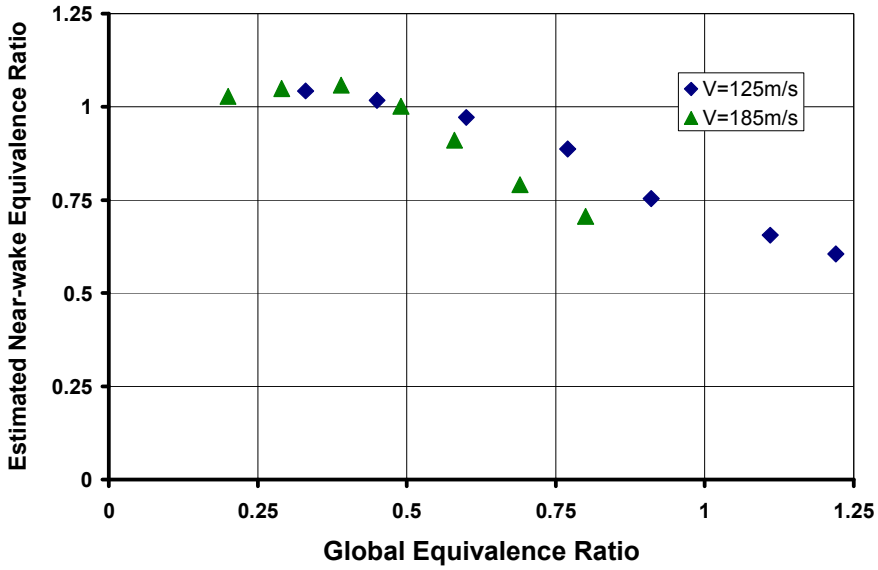

Figure 4.12: Estimated local equivalence ratio in the near-wake vs. global equivalence ratio for close-coupled fuel injection (4.75cm Vane, T~815°C).

The highest global equivalence ratios for each inlet velocity plotted in Figure 4.12 correspond to near blow out conditions. These estimates suggest that the near-wake equivalence ratio at blow out increased with increasing inlet velocity, due to the corresponding decrease in residence time (i.e., the amount of time the reactants were in contact with the hot products in the near-wake). This is in agreement with previous studies of blow out in premixed bluff body-stabilized combustion [2-3, 12], in which lean blow out limits increased (i.e., became richer) as the inlet velocity increased. This result further supports the postulate that the static stability of bluff body-stabilized combustion processes with close-coupled fuel injection is controlled by the local equivalence ratio in the near-wake, as described in §4.1.

It is important to note that the estimates presented in Figure 4.12 are based on flame emission measurements that are integrated across a line-of-sight, even though the local equivalence ratio was, in all likelihood, non-uniform in the span-wise direction (i.e., along the optical integration path). In fact, in Section 4.2.1 it was postulated that the

injection of a discrete number of liquid fuel jets just upstream of the bluff body trailing edge resulted in a "broken" reaction zone in the near-wake, with unburned vitiated air passing between two distinct reaction zones in each shear layer (see Figure 4.5a). The measurements described in Figure 4.12 were only influenced by regions of the near-wake in which combustion occurred, since the chemiluminescent radicals were present only in the reaction zone. Therefore, the data plotted in Figure 4.12 are believed to be the spatial and time-averaged local equivalence ratio of the discrete reaction zones in the near-wake, but they do not consider regions of the control volume in which no reaction occurred.

In light of the above discussion, if the local equivalence ratio in the discrete near-wake reaction zones are known, as well as the amount of unburned gases entrained into the recirculation zone, the average temperature of the recirculation zone gases can be estimated. Such estimates were performed by assuming the near-wake reaction zone consisted of two distinct flame sheets in each shear layer, similar to the illustration shown previously in Figure 4.5a. Each flame sheet was assumed to have a constant equivalence ratio equal to the estimated values plotted in Figure 4.12. The time-averaged flame temperature for each sheet was then estimated based on the reactants temperature and the estimated local equivalence ratio. This was done using the commercial equilibrium solver GasEq by modeling the reactants as a mixture of n-Heptane (since thermodynamic properties for Jet-A were not available), air, and products of lean methane-air combustion (to simulate the pre-burner exhaust). The measured reactants temperature of 815°C was used for these calculations, and the O_2 mole fraction was held constant at 14% for each case, which was the measured concentration during the experiments. The n-Heptane mole fraction was varied based on the estimated near-wake local equivalence ratio.

Previous studies employing premixed reactants have found the recirculation zone gas temperature to be ~90% of the theoretical adiabatic flame temperature calculated based on reactants temperature, pressure, and equivalence ratio (see [2] for example). Therefore, the adiabatic flame temperature computed using GasEq was multiplied by 0.9

to obtain an estimate of the actual products gas temperature leaving each discrete flame sheet. However, in order to account for wake cooling by unburned gas entrainment, an estimate of the average width of each discrete flame sheet was necessary. This was done using the CH* profiles shown previously in Figure 4.4, which compared near-wake heat release between upstream and close-coupled fuel injection modes at Φ_{global}=0.77. For this particular global equivalence ratio, the integrated CH* intensity in the near-wake (i.e., 0<x<2W) with close-coupled fuel injection was approximately 65% of that resulting from upstream fuel injection. Upon comparing C_2*/CH distributions, these two cases were found to have similar local fuel-air ratios in this region, so it was assumed that the difference in CH* emission was mostly due to differences in span-wise distributions of heat release. Based on this comparison, it was estimated that combustion reactions made up 65% of the near-wake when close-coupled fuel injection was used, while the remainder consisted of unburned vitiated air entrained into the recirculation zone. Therefore, the span-wise temperature distribution in the near-wake was assumed to have the profile shown in Figure 4.13 for close-coupled fuel injection tests, where T_b is the estimated local flame temperature in the flame sheets and T_u the unburned vitiated gas temperature.

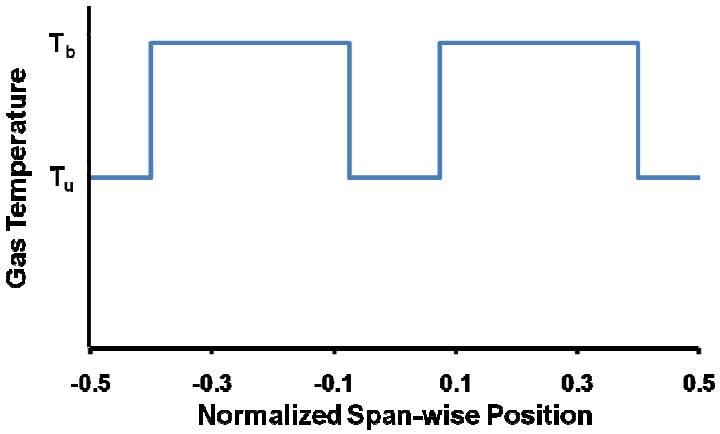

Figure 4.13: Model of span-wise temperature distribution in the near-wake (x<2W) for close-coupled fuel injection.

The spatial and time-averaged gas temperature in the near-wake (i.e., x<2W) was estimated for close-coupled-fuelled flames using the modeled temperature distribution shown in Figure 4.13 and the estimated local equivalence ratios of Figure 4.12. Results of these estimates are plotted vs. Φ_{global} in Figure 4.14. Note that the products temperatures have been normalized by the reactants temperature in this plot. Figure 4.14 shows that the near-wake gas temperature decreased with increasing global equivalence ratio (and thus, increasing fuel penetration) due to the near-wake local equivalence ratio becoming leaner.

For comparison, the estimated near-wake products temperatures for tests using upstream fuel injection are also plotted in Figure 4.14. In the case of upstream fuel injection, the reaction zone likely extended across the combustor span, so the products gas temperature was assumed to be 90% of the theoretical adiabatic flame temperature calculated based on reactants temperature and the local equivalence ratio in the near-wake (which was typically slightly richer than Φ_{global}). Figure 4.14 shows that the near-wake gas temperature was significantly lower for close-coupled fuel injection than "premixed" conditions for all but the leanest global equivalence ratio, due to the hypothesized differences in fuel-air mixing and flame structure between the two fuel injection modes.

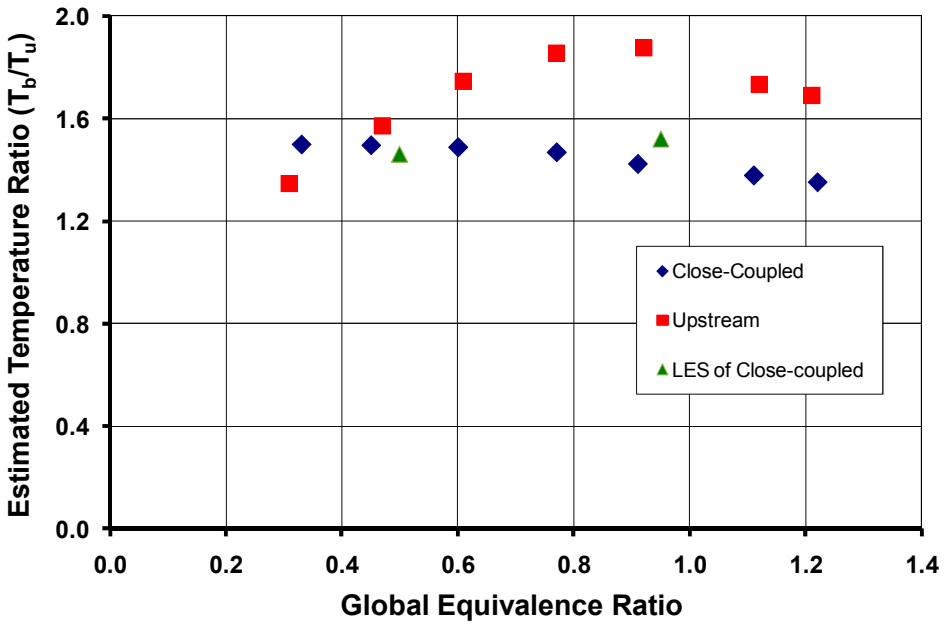

Figure 4.14: Estimated spatial and time-averaged burned-to-unburned temperature ratio in the near-wake (x<2W) vs. global equivalence ratio, comparing fuel injection modes (4.75cm Vane, V=125m/s, T=815°C).

In order to evaluate the accuracy of the temperature estimates in the case of close-coupled fuel injection, computed near-wake gas temperatures obtained from companion LES studies are shown in Figure 4.14 for two global equivalence ratios: 0.50 and 0.95 [53]. These temperatures were obtained by averaging the computed temperature distributions in time and across the combustor span, which were then integrated along the first two bluff body widths downstream of the vane trailing edge. Figure 4.14 demonstrates good agreement between the estimated temperatures based on chemiluminescence measurements and the computed temperatures, supporting the method used to estimate local gas temperature based on line-of-sight-integrated heat release and local equivalence ratio measurements.

Note the relatively minor discrepancy between the estimated near-wake T_b/T_u and the value computed by LES for near-stoichiometric global equivalence ratios. This is attributed, in part, to the assumption that the width of each discrete reaction zone in the

near-wake remained constant as Φ_{global} and, therefore, the fuel jet to cross-flow momentum flux ratio increased. Based on empirical data reported in [47], the lateral dispersion of a liquid jet in cross-flow increases slightly with increasing momentum flux ratio. Thus, the width of the discrete reaction zones likely increased slightly with increasing Φ_{global} due to increasing momentum flux ratio. However, despite the probable increase in reaction zones widths, it is still anticipated that the near-wake T_b/T_u decreased with increasing Φ_{global} due to the reduction in local heat release and equivalence ratio as the fuel jets penetrated further into the cross-flow. Note that the LES data predicted the near-wake T_b/T_u to increase slightly with Φ_{global}. This result is questionable, due to the measured C_2*/CH* data indicating a significant reduction in local equivalence ratio as the fuel sprays penetrated further into the cross-flow.

The qualitative accuracy of the temperature estimates plotted in Figure 4.14 are also supported by the axial distributions of CH* and C_2*/CH* described in Figures 4.6 and 4.10, respectively. Recall that Figures 4.6 and 4.10 considered four cases: Φ_{global}=0.31 and 0.92 for both close-coupled and upstream fuel injection modes. For these four operating conditions, Figure 4.14 shows that the near-wake T_b/T_u decreased in the following order: premixed operation at Φ_{global}=0.92, close-coupled injection at Φ_{global}=0.31, close-coupled injection at Φ_{global}=0.92, and premixed operation at Φ_{global}=0.31. Similarly, Figures 4.6 and 4.10 show that the CH* and C_2*/CH* values in the near-wake (i.e., x<2W) also decreased in the same order, suggesting that the amount of heat release and the local equivalence ratio decreased in this zone, which is in agreement with the estimates that T_b/T_u decreased in the order described above.

4.4 Influence of Near-wake Heat Release upon BVK Flame Dynamics

In Chapter 3, the amplitudes of BVK-associated heat release dynamics were shown to increase with increasing global fuel-air ratio when close-coupled fuelling was

used. The previous three sections established that the largest variations in local equivalence ratio and heat release occurred in the near-wake when the global fuel-air ratio was varied. Consequently, it is postulated that the near-wake fuel-air ratio and heat release strongly influenced the flame dynamics. For this reason, this section will compare the BVK heat release dynamics to the time-averaged heat release, equivalence ratio and temperature in the near-wake reaction zone in order to identify the fundamental processes controlling the BVK instability in reacting flows. The emphasis on the near-wake is partly due to the fact that prior research has established that BVK vortex shedding in non-reacting flows is the result of local absolute instability in this region, which can be eliminated if the recirculation zone density is sufficiently lower than the free-stream value [22]. In Chapter 5, the connection between near-wake combustion processes and local absolute instability will be investigated.

Figure 4.15 compares BVK heat release dynamic intensities to estimated steady-state, local equivalence ratios in the near-wake for close-coupled fuel injection at two inlet velocities: 125 and 185 m/s (T_{in}~850°C). The local equivalence ratio estimates were obtained using the method described in Section 4.3 (see Figure 4.12). Figure 4.15 shows that as the equivalence ratio in the near-wake decreased (due to the fuel jets penetrating further into the cross-flow), the BVK flame dynamics increased in amplitude. This was most likely due to the associated decrease in local density ratio, ρ_u/ρ_b, across the reaction zones (due to decreasing flame temperature), which promoted absolutely instability [22, 34-36, 46]. The influence of near-wake density ratio upon the heat release dynamics will be discussed in more detail later in this section.

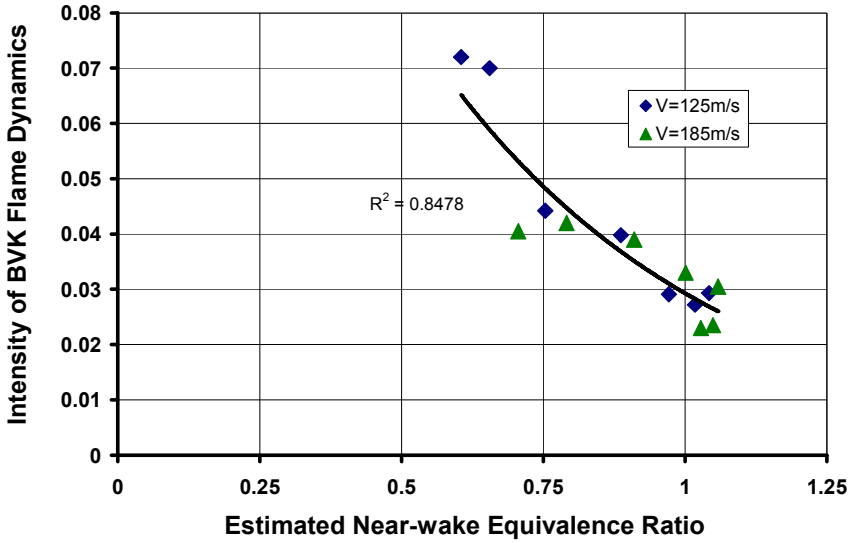

Figure 4.15: Dependence of BVK heat release oscillation intensity upon estimated steady-state near-wake equivalence ratio with close-coupled fuel injection.

It is interesting to note that LES of near blow out, partially-premixed bluff body-stabilized flames performed by Porumbel demonstrated asymmetric vortex shedding to occur when the local equivalence ratio in the near-wake shear layers were leaner than the global value [51]. This was the case despite the relatively high dilatation ratio in the near-wake (T_b/T_u~5), due to the dynamics associated with this near-blow out operation, such as localized extinction events [29]. Thus, in bluff body-stabilized combustion processes with non-uniform equivalence ratio distributions, it appears that the BVK instability is strongly influenced by the local equivalence ratio in the near-wake. Recall that previous research with premixed reactants, as well as experiments performed with upstream fuel injection in this study, found that BVK vortex shedding was most prominent near lean blow out [13-15, 31-32]. Therefore, it may be deduced that BVK heat release dynamics increase in amplitude with decreasing near-wake equivalence ratio, regardless of the fuel injection method and spatial equivalence ratio distribution, and

reach a maximum just before the local mixture becomes lean enough that extinction occurs.

Recall that, in Chapter 3, the amplitudes of BVK-associated heat release oscillations were found to significantly decrease when the fuel was introduced further upstream of the reaction zone. The primary reason for this significant change in flame dynamics was postulated to be the large differences in fuel-air ratio and heat release distributions between upstream and close-coupled fuel injection modes. In order to investigate this, Figure 4.16 compares BVK heat release oscillation intensities with the corresponding time-averaged CH* intensities integrated in the near-wake (see Fig. 4.3) for the two fuel injection modes tested. The spectral amplitudes plotted in Figure 4.16 correspond to the values shown previously in Figure 3.11. Figure 4.16 demonstrates that operating conditions resulting in high-amplitude BVK flame dynamics had low time-averaged heat release (i.e., CH* emission) in the near-wake. As the near-wake heat release increased, the BVK flame dynamics weakened. These results demonstrate the damping nature of combustion process heat release upon the formation and shedding of large-scale, coherent BVK vortices. As the local heat release increased, the local dilatation correspondingly increased, thereby reducing the vorticity magnitude in the near-wake shear layers and inhibiting BVK vortex shedding.

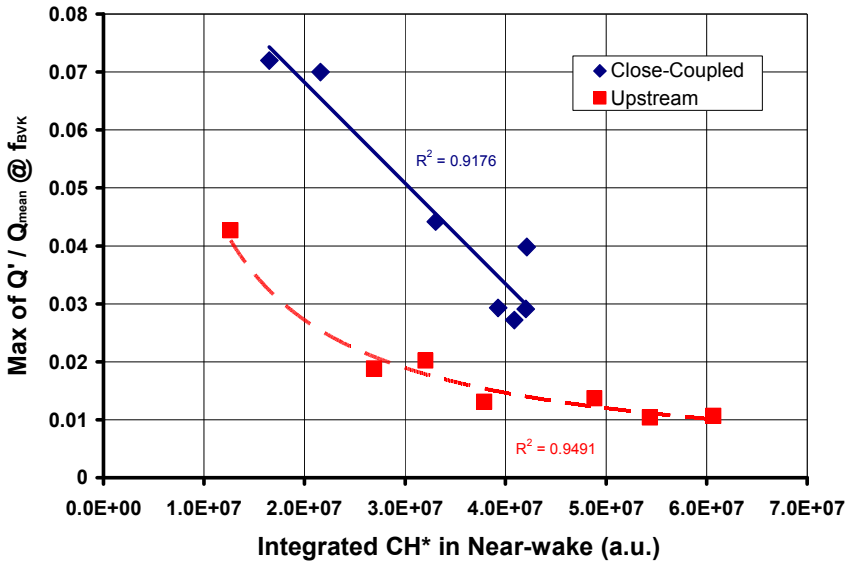

Figure 4.16: Maxima of BVK heat release dynamic amplitude vs. integrated CH* intensity in the near-wake (x<2W) reaction zone, comparing fuel injection modes (4.75 cm Vane, V=125m/s, T=815°C).

It is important to note that the CH* intensity integrated in the near-wake was likely influenced by the local equivalence ratio and may not be directly proportional to the amount of fuel burned in this zone for all cases [39, 42]. For close-coupled fuel injection, both CH* and C_2*/CH* in the near-wake (i.e., x<2W) decreased with increasing Φ_{global}. In this case, the decrease in CH* intensity is an indicator of less fuel being entrained and burned in the near-wake. In contrast, the local equivalence ratio in the near-wake increased with increasing Φ_{global} for upstream fuel injection. However, the local CH* intensity peaked at approximately Φ_{global}=0.77 before decreasing with increasing Φ_{global} beyond this value. The C_2*/CH* measurements indicate that more fuel was present, but the CH* intensity decreased due to the local equivalence ratio becoming rich (as described in [39], CH* intensity follows the same trend with equivalence ratio as flame temperature). Therefore, the data points in Figure 4.16 corresponding to upstream fuel injection with Φ_{global}>0.77 may be erroneous indicators of near-wake heat release. However, note that if these data points were discarded, the same general trend shown in

Figure 4.16 would exist; i.e., the BVK heat release dynamic amplitude would decrease with increasing near-wake CH*. Thus, it may be concluded that the combustion process heat release in the near-wake has a suppressing effect upon the BVK instability.

In general, upstream fuel injection resulted in both larger amounts of near-wake heat release and lower amplitude BVK flame dynamics than in close-coupled fuel injection cases (see Figures 3.11, 4.2 and 4.16). This is attributed to differences in fuel-air mixing and subsequent distribution in the reaction zone between the two fuel injection modes. If the hypothesized flame structures illustrated in Figure 4.5 are correct, then close-coupled fuelling would have resulted in the passage of vitiated air between the distinct reaction zones and into the recirculation zone. The entrainment of unburned air would likely have cooled the recirculated gases, resulting in smaller density gradients across the near-wake reaction zone(s) when averaged across the span of the combustor. This cooling of the near-wake was demonstrated in Figure 4.14. Conversely, the reaction zone likely extended across the entire combustor span when the fuel was introduced well upstream of the bluff body, resulting in stronger near-wake density gradients than close-coupled fuelling. Thus, the suppressing mechanisms of dilatation and baroclinic torque were, in all likelihood, weaker in the case of close-coupled fuel injection than for upstream fuel injection due to the hypothesized differences in near-wake heat release distribution and density gradients. This allowed the BVK flame dynamics to be much stronger in the case of close-coupled fuel injection.

Based on the results presented up to this point, it is believed that transverse density gradients in the near-wake ultimately control the BVK heat release dynamics. While the C_2*/CH* and CH* comparisons shown in Figures 4.15 and 4.16 provide much insight into the physical processes controlling the BVK instability, more direct comparisons to local density ratios are necessary. Such a comparison is shown in Figure 4.17, which plots BVK flame dynamic intensities to the corresponding estimated time-averaged density ratios ($S=\rho_b/\rho_u$) in the near-wake, comparing upstream and close-

coupled fuel injection modes. These density ratios were obtained from the temperature ratio estimates of Figure 4.14. Assuming constant pressure combustion of an ideal gas, the density ratio across the reaction zone was estimated to be equal to the inverse of the temperature ratio, which is a reasonable approximation provided the molecular weights are similar between reactants and products. In the case of Jet-A combustion with vitiated air (which contains significant amounts of CO_2 and H_2O), the molecular weights are quite comparable, especially at lean operation. Thus, the assumption that $\rho_b/\rho_u=T_u/T_b$ is a reasonable one.

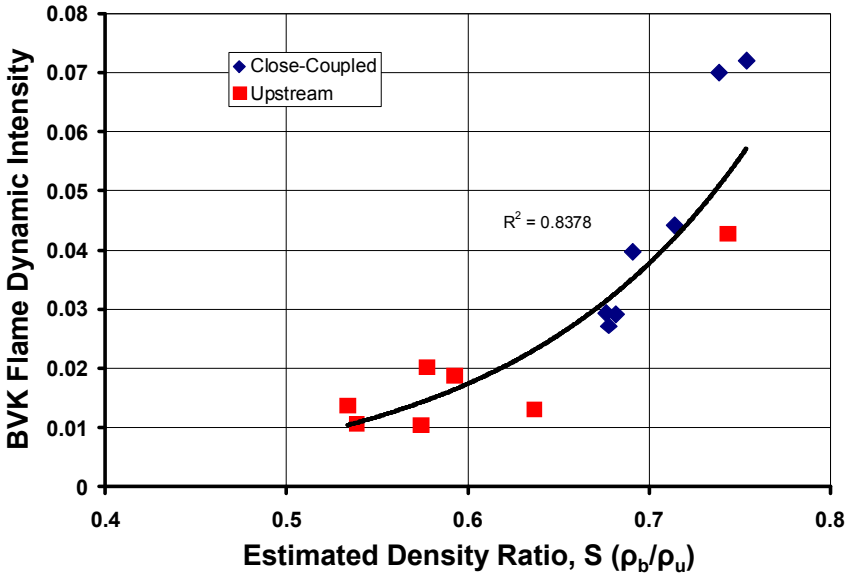

Figure 4.17: BVK flame dynamic intensity vs. estimated steady-state near-wake density ratio, ρ_b/ρ_u, comparing upstream and close-coupled fuel injection modes.

Figure 4.17 shows a strong correlation between BVK heat release dynamic intensity and near-wake density ratio. When the near-wake density ratio was relatively low (ρ_b/ρ_u~0.55), the BVK flame dynamics were negligible, with spectral amplitudes of approximately 1% of the mean luminosity. As ρ_b/ρ_u in the near-wake increased (i.e., approached unity), the BVK flame dynamics increased exponentially in amplitude. Note

that the trend line shown in Figure 4.17 is fitted to both sets of data points (i.e., both fuel injection modes). The fact that both data sets lie near this single characteristic supports the postulate that it is the near-wake density gradients that ultimately control the BVK instability in reacting bluff body wakes, regardless of the fuel injection mode. However, a relatively large degree of scatter can be seen in the data corresponding to upstream fuel injection, especially at low ρ_b/ρ_u values.

Recall from Section 1.2.2 that gas expansion and baroclinic vorticity production suppress the formation and shedding of coherent vortical structures in the presence of combustion. The magnitudes of both damping mechanisms are proportional to the density ratio across the reaction zone, ρ_u/ρ_b. As the density gradient increases, gas expansion and baroclinic torque further reduce the shear layers vorticity magnitude, thus inhibiting their interaction to produce BVK vortices. The strong connection between the magnitude of vorticity in the shear layers and the onset of vortex shedding has already been established [16-20, 52]. Thus, the BVK instability will be suppressed in flames with strong density gradients in the near-wake, where the BVK vortices form. Reacting bluff body wakes with relatively low density gradients across the near-wake shear layers are more susceptible to asymmetric vortex shedding due to the low local dilatation.

The results presented in Figure 4.17 are in agreement with those of previous studies which have demonstrated a strong link between BVK-associated flame dynamics and global burned-to-unburned temperature (and thus, density) ratio in premixed bluff body-stabilized combustion [34-36]. However, the results of this study are unique in that the flame dynamics have been correlated to local density ratios, which is particularly significant for bluff body-stabilized combustion with spatially non-uniform fuel-air ratio and heat release distributions. In fact, in combustion processes with spatial variations in equivalence ratio and other thermodynamic properties, global flow properties are essentially insignificant. Recall from Section 3.3 that significant differences in BVK-associated heat release dynamics occurred at the same global operating conditions by

altering the fuel injection location. The significance of Figure 4.17 is that it shows that the local density gradient across the near-wake reaction zone controls the BVK instability for all reacting bluff body wakes, regardless of the manner in which the fuel is introduced and subsequently distributed in the reacting wake.

While the steady-state, near-wake ρ_b/ρ_u undoubtedly has a strong influence upon the BVK heat release dynamics, the role of phenomena associated with near blow out operation, such as localized extinction events, should not be overlooked. For example, note that a large jump in BVK heat release dynamic intensity occurred as Φ_{global} reduced from 0.45 to 0.31 for upstream fuel injection, as demonstrated in Figure 3.11. Upon analyzing the high-speed movie recorded for premixed operation at Φ_{global}=0.31, localized extinction events were observed based on the appearance of "pockets" with very little flame emission which originated in the near-wake and convected downstream. As described in [29], such localized extinction events have been shown to cause a bifurcation in flame dynamics from symmetric to asymmetric (i.e., BVK) modes in premixed flames. Thus, a key issue that needs to be resolved is how much of the change in BVK heat release dynamic amplitude from Φ_{global}=0.45 to 0.31 was caused by changes in steady-state local ρ_b/ρ_u and how much of it was due to near-blow off events.

As discussed in Section 1.2.1, a complete suppression of the BVK instability is only possible if local absolute instability in the near-wake is eliminated. In the next chapter, the relationship between near-wake combustion processes and local absolute instability will be explored with the aid of a linear stability analysis. This analysis will provide further understanding of the physical processes controlling the BVK instability in reacting bluff body flows.

CHAPTER 5

LINEAR STABILITY ANALYSIS

In the previous chapter, BVK-associated heat release dynamics were found to increase in amplitude as the mean heat release in the near-wake shear layers decreased. As a result, it was postulated that the local density ratio, ρ_b/ρ_u, in the near-wake was the key parameter controlling the onset and amplitude of the BVK instability in bluff body-stabilized reacting flows.

In order to further understand the influence of the local combustion processes in the near-wake upon the BVK instability, a linear stability analysis is presented in this chapter. This analysis was originally developed by Yu and Monkewitz [22] to study the effect of gas density non-uniformities upon the stability of non-reacting wakes and jets. Here, this analysis will be applied to bluff body-stabilized combustion processes by generalizing the combustion process as an abrupt discontinuity in gas density and velocity. That is, the flame will be modeled as an infinitely thin sheet with unburned reactants on one side and fully burned products on the other. A similar analysis is described in [36].

The following section introduces the problem and describes this "vortex sheet" approximation in more detail. Section 5.2 formulates the governing equations, beginning with the linearized equations of motion and ending with a dispersion relation describing the stability of the flow. The results of the model are described in Section 5.3, comparing predicted stability characteristics with measured oscillatory heat release data presented in Chapters 3 and 4. The chapter closes with a discussion of the physical insight provided by the linear stability analysis (§5.4.1), as well as its limitations (§5.4.2).

5.1 Introduction

The connection between local absolute instability and the onset of self-excited, global oscillations of a shear flow has been established [21-24]. For spatially developing flows (such as wakes, mixing layers and jets), the occurrence of a linear, global instability is possible only when a sufficient region of local absolute instability exists in the flow field [21-23]. However, the presence of absolute instability in the flow does not necessarily lead to a self-excited, global instability. Still, if axial variations of key flow parameters are small (on the order of the instability wavelength), the search for local absolute instability yields reasonable approximations for the critical flow parameters leading to a global hydrodynamic instability [21-23]. This is the case with bluff body wakes, which are investigated here. Research has shown that the BVK vortex street is the nonlinear result of a time-amplified global instability, which, in turn, is due to the existence of local absolute instability in the near-wake. The BVK instability is suppressed when absolute instability is eliminated throughout the flow field [21].

The objective of this analysis is to identify the critical flow parameters controlling the onset of local absolute instability in reacting bluff body wakes. Yu and Monkewitz first used this analysis to demonstrate that sufficient heating of the low-velocity gases in the near-wake eliminates absolute instability in gaseous wakes [22]. The significance of this result in regard to reacting bluff body wakes is that substantial heating of the recirculating gases behind the bluff body occurs when combustion is present, and previous research has established that the BVK instability is suppressed in bluff body-stabilized reacting flows with sufficiently high temperature gradients [34]. Therefore, the stability analysis originally described in [22] is repeated here to better understand the influence of combustion heat release upon absolute instability in reacting bluff body wakes.

For this analysis, bluff body-stabilized combustion is generalized as an abrupt discontinuity in gas density and velocity, as shown in Figure 5.1. Fully-vaporized

reactants approach a bluff body stabilizer in an unconfined domain, and combustion occurs in an infinitely thin flame sheet stabilized by the bluff body. As the reactants pass through the flame sheet, they exit with a temperature equal to the local flame temperature, which depends upon the reactants temperature and local equivalence ratio at a given axial location. A vortex sheet coincides with the flame sheet, separating the high-velocity reactants stream from the low velocity products. For this "low-order" analysis, the gas velocity and density on either side of the flame/vortex sheet are assumed to be uniform at a fixed axial location, as shown in Figure 5.1.

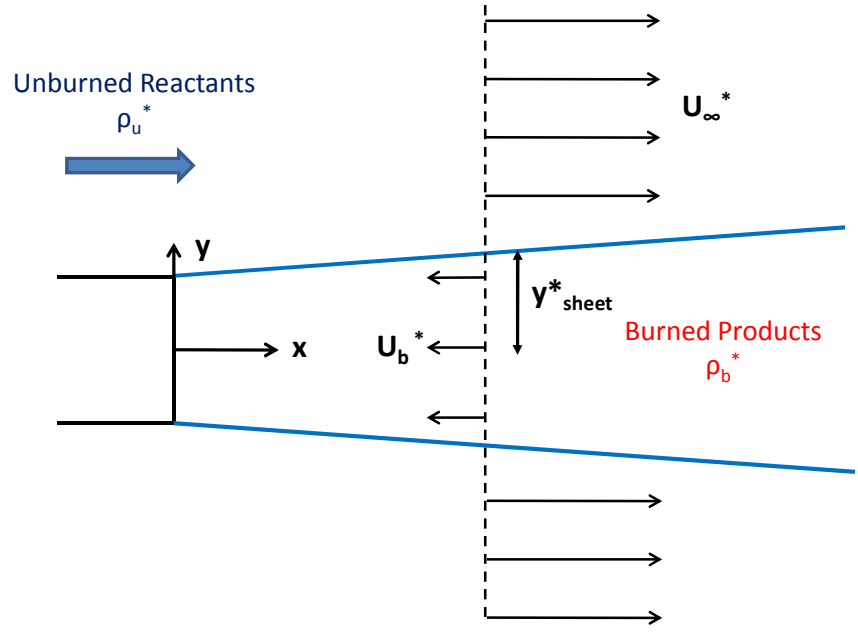

Figure 5.1: Schematic of the double vortex sheet combustion model.

A locally parallel flow approximation is invoked. That is, the mean velocity on either side of the flame/vortex sheet is assumed to have components in the axial direction only, and variations in flow parameters (such as velocity and density) in the axial direction are assumed negligible. Such changes only occur across the interface for a

given axial location. Note that, in reality, bluff body flows are spatially developing (i.e., flow parameters vary in the axial direction) and have velocity components in the transverse direction. However, the flow may be assumed to be locally parallel at a given axial location if axial variations in flow parameters are small over an instability wavelength [23]. This approximation is most valid at the axial location corresponding to maximum flow reversal in the recirculation zone [22-23]. Thus, the subsequent analysis will focus primarily at this axial location, which has been shown to be the most unstable point in the flow [22]. That is, if absolute instability exists in the flow field, it most likely occurs at this axial location.

The instability characteristics predicted by this analysis will be compared with measured heat release dynamics described in Chapter 3. In doing so, it is important to note that the model is purely two-dimensional and only considers gaseous flows, so certain assumptions must be made when predicting the instability characteristics of reacting wakes with spatially-varying flow properties in all three dimensions and/or two-phase flow. In order to compare the results of this analysis to experimental data obtained for close-coupled fuelling, the span-wise and time-averaged values of near-wake gas density presented in Section 4.3 (see Figure 4.14) will be used. In addition, the relatively high ratios between the bluff body width and the lengths of the transverse and span-wise combustor dimensions (approximately 31% and 63%, respectively) limits the extent to which the experimental results can be compared to the results of this unconfined, two-dimensional model. These limitations and those resulting from other assumptions made in comparing the experiments and the stability analysis will be discussed in Section 5.4.2.

5.2 Formulation

The starting points for this analysis are the governing equations of motion given by Batchelor [54]. Assuming both fluid streams are ideal gases, the equations of

continuity, momentum, energy and state for a two-dimensional flow are given by Equations 5.1-4, respectively.

$$\frac{\partial \rho^*}{\partial t^*} + \nabla \cdot (\rho^* \vec{u}^*) = 0 \tag{5.1}$$

$$\rho^* \frac{Du^*_i}{Dt^*} = -\frac{\partial p^*}{\partial x^*_i} + \frac{\partial}{\partial x^*_j}\left[2\mu^* \left(\frac{1}{2}\left(\frac{\partial u^*_i}{\partial x^*_j} + \frac{\partial u^*_j}{\partial x^*_i} \right) - \frac{1}{3} \nabla \cdot \vec{u}^* \delta_{ij} \right) \right] \tag{5.2}$$

$$\frac{DE^*}{Dt^*} = -\frac{p^* (\nabla \cdot \vec{u}^*)}{\rho^*} + \frac{2\mu^*}{\rho^*}\left[\frac{1}{4}\left(\frac{\partial u^*_i}{\partial x^*_j} + \frac{\partial u^*_j}{\partial x^*_i} \right)^2 - \frac{1}{3}\left(\nabla \cdot \vec{u}^* \right)^2 \right] + \frac{1}{\rho^*} \frac{\partial}{\partial x^*_i} (\kappa^* \frac{\partial T^*}{\partial x^*_i}) \tag{5.3}$$

$$p^* = \rho^* \left(\frac{R^*_u}{MW^*} \right) T^* \tag{5.4}$$

In Equations 5.1-4, asterisks denote a dimensional quantity, and the subscripts "*i*" and "*j*" are tensor indices. Body forces and bulk viscosity have been neglected in the above equations. For the remainder of this analysis, constant specific heat (C_p*), Prandtl number (Pr*), and mean pressure ($\bar{p}$*) are assumed.

Each thermodynamic parameter, *a*, is then decomposed into the sum of its steady-state and fluctuating components, *ā(y)* and *a'(x,y,t)*, respectively. Substituting this decomposition into Equations 5.1-4, cancelling the mean terms, and neglecting squares of fluctuating terms leads to the following linearized disturbance equations of continuity, x and y-momentum, energy, and state (Equations 5.5-9, respectively):

$$\frac{\partial \rho'}{\partial t} + \bar{u} \frac{\partial \rho'}{\partial x} + \bar{\rho}_y v' + \bar{\rho}\left(\frac{\partial u'}{\partial x} + \frac{\partial v'}{\partial y} \right) = 0 \tag{5.5}$$

$$\begin{aligned} \bar{\rho}\left(\frac{\partial u'}{\partial t} + \bar{u} \frac{\partial u'}{\partial x} + \bar{u}_y v' \right) = & -\frac{\partial p'}{\partial x} + \frac{1}{\mathrm{Re}}\left[\bar{\mu}\left(\frac{4}{3}\frac{\partial^2 u'}{\partial x^2} + \frac{1}{3}\frac{\partial^2 v'}{\partial x \partial y} + \frac{\partial^2 u'}{\partial y^2} \right) \right] \\ & + \frac{1}{\mathrm{Re}}\left[\bar{u}_y \left(\bar{\mu}_{Ty} T' + \bar{\mu}_T \frac{\partial T'}{\partial y} \right) + \bar{\mu}_y \left(\frac{\partial u'}{\partial y} + \frac{\partial v'}{\partial x} \right) + \bar{u}_{yy} \bar{\mu}_T T' \right] \end{aligned} \tag{5.6}$$

$$\bar{\rho}\left(\frac{\partial v'}{\partial t}+\bar{u}\frac{\partial v'}{\partial x}\right)=-\frac{\partial p'}{\partial y}+\frac{1}{\mathrm{Re}}\left[\bar{\mu}\left(\frac{\partial^2 v'}{\partial x^2}+\frac{1}{3}\frac{\partial^2 u'}{\partial x\partial y}+\frac{4}{3}\frac{\partial^2 v'}{\partial y^2}\right)\right] + \frac{1}{\mathrm{Re}}\left[\bar{\mu}_y\left(-\frac{2}{3}\frac{\partial u'}{\partial x}+\frac{4}{3}\frac{\partial v'}{\partial y}\right)+\bar{u}_y\bar{\mu}_T\frac{\partial T'}{\partial x}\right] \tag{5.7}$$

$$\bar{\rho}\left(\frac{\partial T'}{\partial t}+\bar{u}\frac{\partial T'}{\partial x}+\bar{T}_y v'\right)=\frac{1}{\mathrm{Re}\,\mathrm{Pr}}\left[\bar{\kappa}\left(\frac{\partial^2 T'}{\partial x^2}+\frac{\partial^2 T'}{\partial y^2}\right)+\bar{\kappa}_y\frac{\partial T'}{\partial y}\right] + \frac{1}{\mathrm{Re}\,\mathrm{Pr}}\left[\bar{T}_y\left(\bar{\kappa}_{Ty}T'+\bar{\kappa}_T\frac{\partial T'}{\partial y}\right)+\bar{T}_{yy}\bar{\kappa}_T T'\right] \tag{5.8}$$

$$\frac{\rho'}{\bar{\rho}}+\frac{T'}{\bar{T}}=0 \tag{5.9}$$

where $(\,)_y$ and $(\,)_T$ denote derivatives with respect to y and T, respectively. Note the terms in Equations 5.5-9 are non-dimensional (i.e., the asterisks have been dropped). The reference velocity used for this normalization is the average of the two gases separated by the flame/vortex sheet:

$$\bar{U}_{av}^{\,*}=0.5\left(\bar{U}_b^{\,*}+\bar{U}_\infty^{\,*}\right) \tag{5.10}$$

The reference length is the mean transverse distance of the vortex sheet from the combustor centerline, y^*_{sheet} (see Figure 5.1). The remaining thermodynamic properties are normalized by their free-stream values. With these normalizations,

$$\mathrm{Re}=\frac{\bar{\rho}_\infty^{\,*}\bar{U}_{av}^{\,*}y_{sheet}^{\,*}}{\bar{\mu}_\infty^{\,*}} \tag{5.11}$$

$$\mathrm{Pr}=\frac{c_p^{\,*}\bar{\mu}_\infty^{\,*}}{\bar{\kappa}_\infty^{\,*}} \tag{5.12}$$

$$\kappa'=\mu'=\bar{\mu}_T T' \tag{5.13}$$

since κ and μ are functions of T only, and Pr is assumed constant.

Each unsteady variable, a', is expanded as a normal mode of the form:

$$a'=\hat{a}\exp\left[ik\left(x-ct\right)\right] \tag{5.14}$$

$$c = \frac{\omega}{k} \tag{5.15}$$

where k is the wave number, ω the frequency, and $\hat{a}$ the amplitude of the disturbance. Substituting this expansion into Equations 5.5-9, the following five equations result:

$$\hat{\rho}\left(\bar{u}-c\right)+\bar{\rho}\hat{u}=\frac{i}{k}\frac{\partial}{\partial y}\left(\bar{\rho}\hat{v}\right) \tag{5.16}$$

$$\begin{aligned}\bar{\rho}\hat{u}\left(\bar{u}-c\right)-\frac{i\bar{\rho}\bar{u}_y\hat{v}}{k} &= -\hat{p}+\frac{1}{\mathrm{Re}}\left[\bar{\mu}\left(\frac{4}{3}ik\hat{u}+\frac{1}{3}\hat{v}_y-\frac{i\hat{u}_{yy}}{k}\right)\right] \\ &\quad +\frac{1}{\mathrm{Re}}\left[\bar{\mu}_y\left(\hat{v}-\frac{i\hat{u}_y}{k}\right)-\frac{i}{k}\frac{\partial}{\partial y}\left(\bar{u}_y\bar{\mu}_T\hat{T}\right)\right]\end{aligned} \tag{5.17}$$

$$\bar{\rho}\hat{v}\left(\bar{u}-c\right)=\frac{i\hat{p}_y}{k}+\frac{1}{\mathrm{Re}}\left[\bar{\mu}ik\hat{v}-\frac{i4}{3k}\frac{\partial}{\partial y}\left(\hat{v}_y\bar{\mu}\right)+\frac{1}{3}\frac{\partial}{\partial y}\left(\bar{\mu}\hat{u}\right)-\bar{\mu}_y\hat{u}+\bar{u}_y\bar{\mu}_T\hat{T}\right] \tag{5.18}$$

$$\bar{\rho}\left[\hat{T}\left(\bar{u}-c\right)ik+\bar{T}_y\hat{v}\right]=\frac{1}{\mathrm{Re}\,\mathrm{Pr}}\left[-k^2\bar{\kappa}\hat{T}+\frac{\partial}{\partial y}\left(\bar{\kappa}\hat{T}_y\right)+\frac{\partial}{\partial y}\left(\bar{T}_y\bar{\kappa}_T\hat{T}\right)\right] \tag{5.19}$$

$$\hat{T}+\hat{\rho}\bar{T}^2=0 \tag{5.20}$$

In order for the locally parallel flow assumption to satisfy the governing equations of motion (5.1-4), viscous and thermal diffusion must be negligible [22]. This assumption reduces the system of equations 5.16-20 to a single second-order differential equation for the disturbance pressure (see Appendix C for a detailed derivation):

$$\frac{d^2\hat{p}}{dy^2}-\left[\frac{\bar{\rho}_y}{\bar{\rho}}+\frac{2\bar{u}_y}{\left(\bar{u}-c\right)}\right]\frac{d\hat{p}}{dy}-k^2\hat{p}=0 \tag{5.21}$$

Equation 5.21 can be solved if the density and velocity distributions, along with appropriate boundary conditions, are known. Boundary conditions must be chosen based on the desired symmetry of the unsteady flow field (i.e., sinuous or varicose modes) and in order to ensure that disturbances vanish as $y\rightarrow\infty$. For this analysis, only the sinuous mode is considered, as this corresponds to the BVK instability.

The vortex sheet approximation described in the previous section allows Equation 5.21 to be integrated analytically for each gas stream on either side of the flame/vortex sheet. The boundary conditions for each gas stream are:

$$\begin{bmatrix} \hat{p} \\ \hat{p}_y \end{bmatrix}(y \to \infty) \sim \begin{bmatrix} 1 \\ -k \end{bmatrix} \exp(-ky)$$
$$\begin{bmatrix} \hat{p} \\ \hat{p}_y \end{bmatrix}(y = 0) = \begin{bmatrix} 0 \\ 1 \end{bmatrix} \tag{5.22}$$

In order to arrive at a dispersion relation between ω and k, perturbation pressure and transverse displacement must be matched at the interface of the two fluid streams [22, 55]. For this purpose, an unsteady velocity potential is defined for each gas stream. Applying the boundary conditions of Equation 5.22, it can be readily shown (see Appendix C) that these velocity potentials are given by:

$$\phi_\infty = \overline{\phi}_\infty + C_\infty e^{-ky} \exp\left[ik\left(x - ct\right)\right]$$
$$\phi_b = \overline{\phi}_b + C_b (e^{ky} - e^{-ky}) \exp\left[ik\left(x - ct\right)\right] \tag{5.23}$$

where C_∞ and C_b are constants that must be solved for based on boundary conditions.

Let $h`(x,t)$ be the distance the vortex sheet is displaced from $y^*_{sheet}$ (i.e., $y$=1) at a given time instant and axial position, and assume that $h`$ takes on the form given by Eqn. 5.14. For each gas stream, the transverse displacement at the unsteady interface (i.e., flame/vortex sheet) is given by:

$$v' = \frac{\partial \phi_i}{\partial y} = \frac{dh}{dt} = \frac{\partial h}{\partial t} + \frac{\partial h}{\partial x}\frac{\partial x}{\partial t} \tag{5.24}$$

where the subscript "i" in this case represents the particular gas stream considered.

Using the velocity potentials of Equation 5.23, the unsteady Bernoulli equation for each gas stream is given by

$$\frac{p_i}{\rho_i} = \frac{p_{o,i}}{\rho_i} - \frac{\partial \phi_i}{\partial t} - \frac{1}{2}\left(\overline{u}_i + \frac{\partial \phi_i}{\partial x}\right)^2 - \frac{1}{2}\left(\frac{\partial \phi_i}{\partial y}\right)^2 \tag{5.25}$$

Solving Equations 5.24 and 5.25 for the transverse displacement and perturbation pressure, respectively, of each gas stream and matching at the interface leads to a single dispersion relation between ω and k:

$$S\frac{\left(1+\Lambda-c\right)^2}{\left(1-\Lambda-c\right)^2}=-\frac{e^k+e^{-k}}{e^k-e^{-k}}=-\coth(k) \tag{5.26}$$

where

$$S\equiv\frac{\bar{\rho}_b^*}{\bar{\rho}_\infty^*} \tag{5.27}$$

$$\Lambda\equiv\frac{\bar{u}_b^*-\bar{u}_\infty^*}{\bar{u}_b^*+\bar{u}_\infty^*} \tag{5.28}$$

Equation 5.26, along with definitions 5.27-28, is the governing dispersion relation describing the local instability characteristics at a given axial location, provided the locally parallel flow approximation is valid at that position. These equations show that the flow stability depends upon the products-to-reactants gas density and velocity ratios, ρ_b/ρ_∞ and U_b/U_∞, at the given axial location. Recall that in Section 4.4 it was postulated that the BVK instability in reacting flows is controlled by transverse density gradients in the near-wake. Equation 5.26 suggests that an additional parameter, the velocity gradient, also significantly influences the flow instability characteristics.

5.3 Results

5.3.1 Dependence of Absolute Growth Rate upon Density and Velocity Ratios

As previously stated, the objective of this analysis is to determine the critical flow parameters resulting in absolute instability in reacting bluff body wakes. To do this, Equation 5.26 is solved for the complex frequency corresponding to zero group velocity [21-23] for a given combination of S and Λ. This frequency is also referred to as the "absolute frequency" and is given by:

$$\frac{\partial \omega}{\partial k}(k^0) = 0$$
$$\omega(k^0) = \omega^0 \tag{5.29}$$

provided that k^0 corresponds to a "pinch-point" of two spatial branches [23]. If these criteria are met, k^0 is a saddle point of $\omega(k)$. Following an infinitesimal impulse at a particular time and location, the system response at that location as $t \rightarrow \infty$ depends upon the real and complex components of ω^0 [21, 23]. The disturbance frequency viewed by a stationary observer in the laboratory reference frame is given by the real component, ω^0_r. The imaginary component, ω^0_i, is the linear growth rate of the system following the initial perturbation. If ω^0_i is positive, oscillations grow exponentially at a given axial location, and the flow is absolutely unstable. If negative, any instability is of the convective type, and all disturbances are swept away by the flow.

The boundary between convective and absolute instability (i.e., the contour at which ω^0_i=0) is plotted in Figure 5.2 as a function of centerline-to-free stream (or, burned-to-unburned) density and velocity ratios. This figure provides an overview of the critical flow parameters resulting in local absolute instability in reacting bluff body wakes. Figure 5.2 shows that the critical density ratio at which the flow transitions from convective to absolutely unstable strongly depends upon the velocity ratio between the fluid streams. When the flow reversal in the near-wake is strong (i.e., when the recirculation zone velocities are highly-negative), local absolute instability is suppressed only when the recirculated gases are well heated. For example, when U^*_b/U^*_∞=-0.3, absolute instability is suppressed for $S < \sim 0.6$. In contrast, at axial locations in which the flow is weakly reversed, low amounts of heating are required to suppress absolute instability. In the limit of isothermal wake flow (S=1), Figure 5.2 shows that absolute instability is suppressed for centerline-to-free stream velocity ratios greater than -0.05. Thus, for isothermal flows or exothermic reacting flows (i.e., $S \leq 1$) all linear

hydrodynamic instabilities are of the convective type downstream of the recirculation zone, as the centerline-to-free stream velocity ratio is always positive beyond this point.

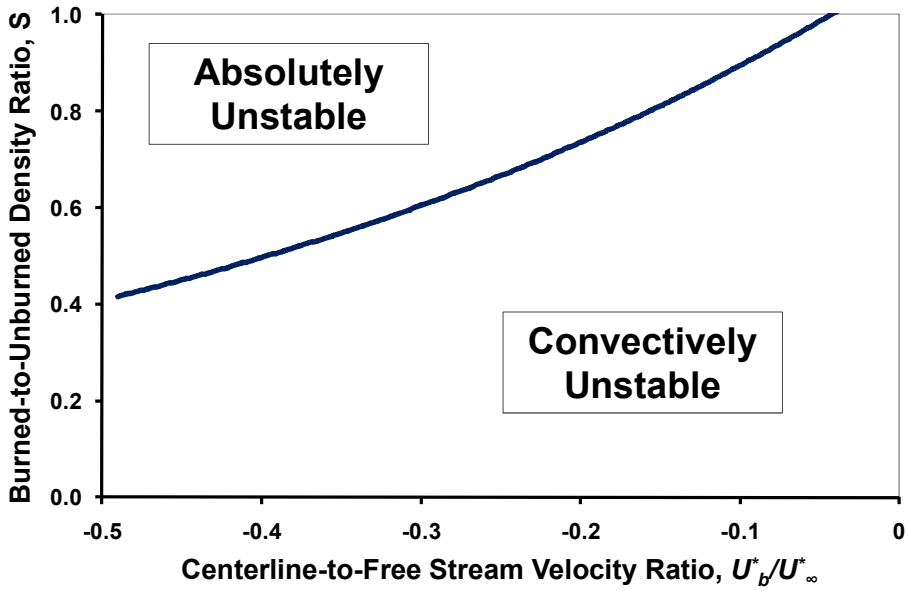

Figure 5.2: Boundary between convective and absolute instability as a function of centerline-to-free stream density and velocity ratios (double-vortex sheet wake).

The absolute growth rate, ω^0_i, is plotted in Figure 5.3 for a range of density and velocity ratios likely to exist in bluff body-stabilized reacting wakes with high-temperature, vitiated reactants. Figure 5.3 shows that the onset and growth rate of absolute instability strongly depends upon both density and velocity ratios. For all velocity ratios, the absolute growth rate increases with increasing density ratio, S. However, the degree to which ω^0_i increases with increasing S strongly depends upon the velocity ratio, U^*_b/U^*_∞. The lower (i.e., more negative) the velocity ratio, the more ω^0_i increases with increasing burned-to-unburned density ratio. Figure 5.3 also shows that the absolute growth rate increases as U^*_b/U^*_∞ decreases (i.e., becomes more negative) for a fixed density ratio. These results suggest that when the near-wake flow reversal is strong, absolute instability is more likely to occur.

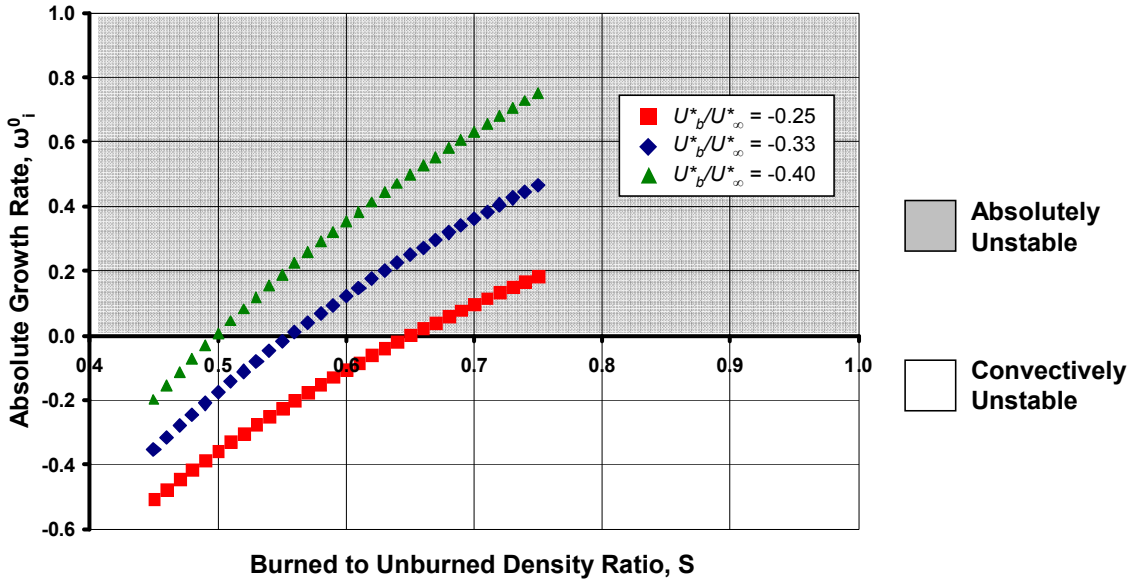

Figure 5.3: Absolute growth rate (ω^0_i) vs. density ratio (S) for varying velocity ratios (U^*_b/U^*_∞).

The results presented in Figures 5.2-3 provide insight into the fundamental processes controlling the onset of absolute instability in bluff body-stabilized reacting flows. First, they demonstrate that it is the heating by the combustion processes in the near-wake (especially in the vicinity of maximum flow reversal) which controls the instability characteristics of the flow (i.e., whether the flow is absolutely or convectively unstable). Absolute instability is eliminated only when the temperature rise across the near-wake reacting shear layers is sufficiently high. The critical density ratio at which suppression occurs depends upon the near-wake velocity distribution, but note that for the strongest flow reversal case plotted in Figure 5.2, U^*_b/U^*_∞ = -0.49, local absolute instability is suppressed when ρ^*_b/ρ^*_∞ reaches approximately 0.43. Assuming constant pressure and molecular weight on either side of the flame sheet, this corresponds to a temperature ratio of T_b/T_u~2.3. This result is in agreement with previous studies which demonstrated the absolutely unstable, BVK vortex street to be eliminated in reacting bluff body flows with T_b/T_u slightly greater than two [34-36].

Second, the results demonstrate that local absolute instability is impossible at the downstream end of the recirculation zone and beyond, since $\omega^0_i>0$ only at axial locations in which the centerline flow is reversed when $S\leq 1$. Therefore, the local density ratio (ρ_b/ρ_u) in the near-wake is critical for the onset of absolute instability. Further downstream, heat release due to combustion has no influence on absolute instability. This is in agreement with the experimental results described in the last chapter, in which the amplitude of BVK-associated heat release oscillations were correlated with the local density ratio in the near-wake.

Finally, the velocity ratio dependence described in Figures 5.2-3 suggests that bluff body geometry and blockage ratio also influence the onset of absolute instability in reacting wakes. For example, combustion systems using flame holders with "bluff" geometries, such as V-gutters and disks, may be more susceptible to absolute instabilities than those with more slender, aerodynamic designs (e.g., the "vane" configuration used in this study) due to the presence of strong flow reversal in the near-wake [56]. Absolute instability can potentially be eliminated in bluff body combustion systems operating near a critical density ratio by using more "streamlined" bluff body geometries to reduce the near-wake flow reversal. This result should be validated in the laboratory environment, as it has important implications for the design of practical bluff body-stabilized combustion systems.

5.3.2 Comparison with Measured Heat Release Dynamics

The results of this stability analysis were compared to the measured heat release dynamics presented in Chapter 3. To perform these comparisons, the near-wake gas temperature estimates shown in Figure 4.14 were used to estimate the steady-state, near-wake density ratio, S. Assuming constant pressure combustion and noting that the molecular weights of the reactants and products are approximately equal (as the vitiated gas stream contains products of combustion), the density ratios were estimated to be the

inverse of their temperature ratio: $S=\rho^*_b/\rho^*_\infty=T_u/T_b$. In the case of close-coupled fuel injection, these estimates were validated by parallel LES computations [53].

The velocity ratio, U^*_b/U^*_∞, was also estimated based on the LES computations, as well as reacting flow PIV measurements performed in a separate study which used a bluff body geometry and blockage ratio similar to the 4.75 cm vane used in this study [35-36]. For each fuel-air ratio and fuel injection method, a constant maximum reverse flow velocity was assumed, U^*_b/U^*_∞ =-0.34, which was the computed maximum for a close-coupled-fuelled flame at Φ_{global}=0.50 [53]. Even though the near-wake velocity distribution in the experiments likely changed as the local heat release and dilatation varied, it is assumed that the maximum reverse flow velocity did not vary considerably. This is supported by the PIV measurements reported in [35-36] which demonstrated that the minimum (i.e., most negative) value of U^*_b/U^*_∞ remained nearly constant as ρ^*_∞/ρ^*_b was varied from 1.7 to 3.0 for a fixed bluff body geometry and approach velocity. Thus, the assumption of constant minimum U^*_b/U^*_∞ is reasonable for the low density ratio, reacting flow experiments under consideration. Furthermore, it is assumed that the axial location in which the centerline flow reversal was strongest always occurred within the first two bluff body widths downstream of the trailing edge (i.e., within the area of integration in performing the density ratio estimates) for each operating condition. The validity of these assumptions is discussed further in Section 5.4.2.

Figure 5.4 plots maximum absolute growth rates computed for each experimental flow condition versus their measured BVK heat release dynamic intensities, comparing results obtained for close-coupled and upstream fuel injection for varying Φ_{global}. Note that the dynamic heat release intensities shown in Figure 5.4 were taken from Figure 3.11. Figure 5.4 shows that all operating conditions predicted to be absolutely unstable (i.e., $\omega^0_i>0$) experienced BVK heat release dynamics with spectral amplitudes greater than 1% of the mean luminosity. All of the close-coupled-fuelled operating conditions and the "premixed" condition near lean blow out (Φ_{global}=0.31) were predicted to have

high absolute growth rates, with ω^0_i values greater than 0.3. Correspondingly, these conditions were observed to be the most unstable, with spectral amplitudes at the BVK frequency ranging between 2.5 and 7.2% of the mean luminosity.

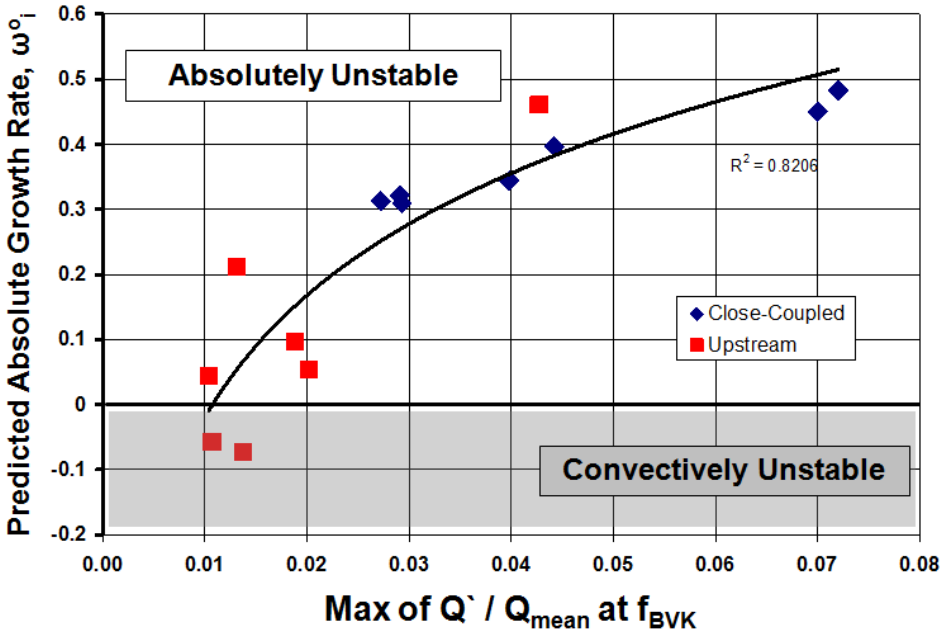

Figure 5.4: Predicted maximum absolute growth rates vs. measured BVK heat release dynamic intensities, comparing upstream and close-coupled fuel injection modes for varying Φ_{global} (V=125 m/s, T_{in}=815°C, 4.75 cm Vane).

While the purpose of this linear stability analysis was to predict whether or not a given operating condition resulted in absolute instability, it is worth noting the general correlation between the predicted absolute growth rate and the measured oscillatory heat release amplitude shown in Figure 5.4. This figure shows that operating conditions resulting in high-amplitude BVK heat release dynamics were predicted to have high linear growth rates. Thus, it is postulated that bluff body-stabilized combustion processes with high linear, absolute growth rates will result in high limit-cycle amplitudes at the BVK frequency, and that the near-wake density gradients control both the onset and saturation amplitude of the BVK instability. However, it must be emphasized that a high

linear growth rate must not necessarily lead to a large saturation amplitude, and further work is needed to identify the damping mechanisms controlling saturation and validate the above hypothesis. This requires non-linear analysis, which is beyond the scope of this thesis.

Due to the use of high-temperature, vitiated reactants in these tests, only "premixed" operation (i.e., upstream fuel injection) at near-stoichiometric fuel-air ratios resulted in near-wake density ratios, ρ^*_b/ρ^*_u, low enough that absolute instability could be suppressed. For the test data plotted in Figure 5.4, only two operating conditions (upstream fuel injection at Φ_{global}=0.77 and 0.92) were predicted to be convectively unstable. However, oscillatory heat release spectra revealed low amplitude BVK flame dynamics ($Q`/Q_{mean}$~1%) for these conditions, as shown in Figure 5.4. This apparent inconsistency is believed to be due to several reasons.

First, the stability analysis assumes a double vortex sheet velocity profile with uniform density on either side of the vortex sheets, which is an oversimplification of typical velocity and density distributions observed in reacting bluff body wakes. As pointed out in [22], a considerably lower density ratio is needed to eliminate absolute instability at a given velocity ratio for such "realistic" velocity profiles. Thus, the actual stability boundary likely occurs at density ratios lower than those shown previously in Figure 5.2, which could result in all of the operating conditions shown in Figure 5.4 being absolutely unstable.

Second, the stability analysis assumes a laminar mean flow, whereas the reacting flow fields in the experiments were turbulent, which may contribute to the apparent discrepancy between predicted growth rate and measured heat release dynamics for the operating conditions predicted to be convectively unstable. Note that these operating conditions fell near the predicted boundary between absolute and convective instability (i.e., ω^0_i was nearly zero). When the high-speed movies recorded at these conditions were analyzed, the BVK flame dynamics appeared intermittently, with most frames

showing no clear evidence of asymmetry. This is illustrated in Figure 5.5, which compares frames extracted from the same high-speed movie (Φ_{global}=0.77, upstream fuel injection) at two different time instances, showing two distinct flame structures. Similar intermittencies in flame dynamics were observed for operating conditions predicted to be absolutely unstable but with low growth rates (i.e., $0<\omega^0_i<0.1$). Due to the unsteady flow field associated with this high Reynolds number operation (Re~40,000) it is possible that operating conditions near this "stability boundary" were convectively unstable for a certain time interval and absolutely unstable for another, resulting in intermittent BVK heat release dynamics. Emerson et al. observed similar intermittencies and hypothesize that the transition in stability cannot be characterized by a sharp bifurcation for such high Reynolds number flows [36].

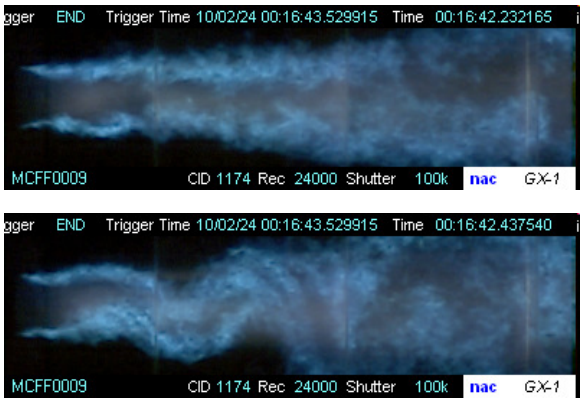

Figure 5.5: Comparison of frames extracted from the same high-speed movie, showing intermittency in flame structure (Φ_{global}=0.77, upstream fuel injection).

Regardless of the discrepancies described above, it should be emphasized that the BVK heat release dynamics were quite low for operating conditions in which ω^0_i was predicted to be near zero, whether positive or negative. Thus, the prediction that these operating conditions were near the transition between absolute and convective instability appears to be a good one.

In order to obtain a better characterization of the boundary between convective and absolute instabilities, heat release dynamics were measured at operating conditions resulting in lower near-wake density ratios, ρ^*_b/ρ^*_∞, and, therefore, lower (more negative) absolute growth rates than those shown previously in Figure 5.4. This was done by reducing the reactants stream temperature to 675°C and increasing the vitiated air oxygen concentration to 16.5%. Both the reduced reactants temperature and increased oxygen content resulted in higher products-to-reactants temperature ratios and, therefore, lower near-wake density ratios, ρ^*_b/ρ^*_u.

High-speed movies were recorded at Φ_{global}=1.1 for upstream fuel injection and Φ_{global}=0.9 for close-coupled fuel injection (blow out occurred beyond this equivalence ratio) at this inlet air condition. Figure 5.6 compares their oscillatory heat release spectra measured at three bluff body widths downstream of the vane trailing edge. While the spectrum for the close-coupled-fuelled case clearly shows heat release fluctuations at the BVK instability (f=1175 Hz), the "premixed" flame spectrum displays no noticeable BVK dynamics. This same result was obtained at all axial locations, indicating that the BVK instability was completely suppressed for the upstream fuel injection case due to its low near-wake density ratio, ρ^*_b/ρ^*_u~0.44. In contrast, when close-coupled fuel injection was used, the recirculated gas temperature decreased due to locally lean combustion and unburned reactants entrainment, resulting in a higher near-wake density ratio (ρ_b/ρ_u~0.62) which led to the BVK heat release dynamics shown in Figure 5.6.

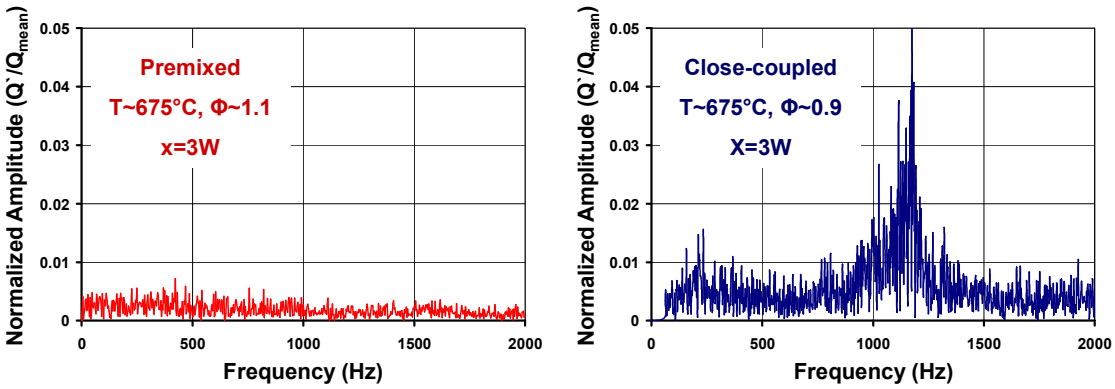

Figure 5.6: Comparison of oscillatory heat release spectra between upstream (left) and close-coupled (right) fuel injection at Φ_{global}~1.0 and T_{in}~675°C.

Upon computing the absolute growth rates for the operating conditions described in Figure 5.6, the drastic difference in heat release dynamics can be attributed to their differences in hydrodynamic instability modes. Despite having similar global operating conditions, the close-coupled fuel injection case was absolutely unstable (ω^0_i=0.17), whereas the upstream fuel injection case was convectively unstable (ω^0_i = -0.38). This is shown in Figure 5.7, which plots these operating conditions on a stability map similar to the one in Figure 5.2. The "premixed" case had a density ratio much lower than the predicted critical value due to its high flame temperature. The lack of BVK-associated fluctuations in the dynamic heat release spectra indicates that this operating condition was "continuously" in the convectively unstable regime, due to its highly-negative value of ω^0_i. In contrast, the close-coupled fuel injection case apparently resulted in a near-wake density ratio well above the critical value for absolute instability due to locally lean combustion and reactants entrainment, resulting in the strong BVK heat release dynamics shown in Figure 5.6. Therefore, the non-uniform near-wake fuel distribution associated with close-coupled fuel injection resulted in an absolutely unstable wake at operating conditions in which premixed operation was convectively unstable.

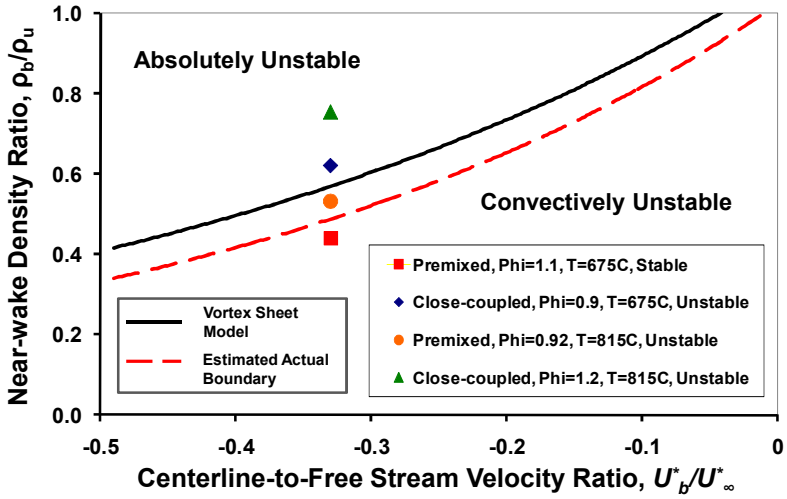

Figure 5.7: Dependence of instability mode upon fuel injection method and reactants temperature.

For comparison, Figure 5.7 also plots operating conditions at similar equivalence ratios for each fuel injection mode, but with higher reactants temperatures: T_{in}=815°C. It can be seen that "premixed" operation at 815°C resulted in a near-wake density ratio much closer to the predicted stability boundary than the T_{in}=675°C case, which is believed to be the reason why BVK heat release dynamics were observed intermittently (see Figures 5.4-5). Since operation at T_{in}=675°C resulted in lower values of ρ^*_b/ρ^*_u in the near-wake and, thus, absolute growth rates much lower than the predicted stability boundary, an absolutely unstable BVK mode was not observed at any instant during the time-resolved flame visualization. In addition, note that if more realistic density and velocity profiles were used in the analysis, it is anticipated that the predicted stability boundary would fall somewhere between these two flow conditions. This is demonstrated by the red dashed line in Figure 5.7, which is an approximation of the actual stability boundary for the experiments under consideration. In this case, the T_{in}=815°C case would be absolutely unstable, whereas the T_{in}=675°C case would remain convectively unstable, in agreement with the measured heat release dynamics.

The results shown in Figures 5.4-5.7 demonstrate the ability of this relatively simple, laminar, vortex sheet model (which generalizes combustion as a discontinuity in gas temperature) to predict the onset and location of absolute instability in turbulent, reacting bluff body wakes. Stability boundaries predicted by this analysis may be viewed as a conservative estimate of reacting flow operating conditions resulting in absolute instability, as consideration of velocity and density profiles typically observed in bluff body-stabilized combustion processes will shift the stability boundary toward lower values of ρ_b/ρ_u. This simplified model can also be used to predict convectively unstable reacting flow operating conditions, provided the computed absolute growth rate is sufficiently lower than the predicted stability boundary (i.e., $\omega^0_i < -0.1$). This is because intermittency in flame dynamics between symmetric and asymmetric modes have been observed in this study and in [35-36] when $\omega^0_i \sim 0$.

5.4 Discussion

5.4.1 Influence of Heat Release Distribution upon Absolute Instability

The results of this analysis reinforce the hypothesis that the BVK instability in reacting bluff body wakes is caused by an absolute instability in the near-wake region. This instability disappears as the temperature rise across the reacting shear layers increases beyond a certain threshold limit. Consequently, the spatial distributions of fuel-air ratio and heat release in the near-wake strongly influence the hydrodynamic instability characteristics of bluff body-stabilized combustion processes. This is illustrated in Figure 5.8, which describes the mechanisms controlling the BVK-associated heat release dynamics for the two fuel injection modes utilized in this study – close-coupled and premixed.

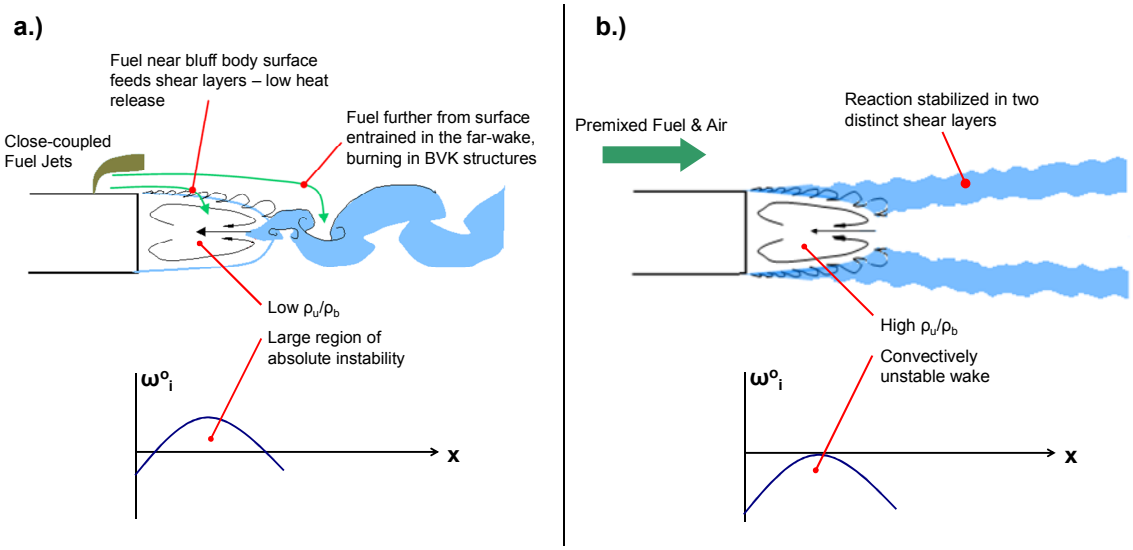

Figure 5.8: Influence of fuel and heat release distribution upon absolute instability in reacting bluff body wakes.

When close-coupled fuel injection is utilized (see Figure 5.8a), the fuel and heat release distributions in the reacting wake are highly dependent upon the fuel spray penetration into the cross-flow. Small droplets stripped from the fuel jet by aerodynamic shear are supplied to the boundary layers along the bluff body surface, where they evaporate, mix with the air, and are transported to the reacting shear layers in the near-wake. However, larger droplets formed by liquid column breakup processes are either not fully vaporized and mixed with the incoming air stream by the time they are entrained into the near-wake, or they penetrate into the faster moving free-stream flow and are transported to the far-wake. In fact, the majority of the fuel is usually entrained and burned in the far-wake, especially when the fuel jet penetration is high. As a result, the amount of heat release in the near-wake shear layers is low. In addition, unburned reactants are entrained into the recirculation zone due to the proximity of the fuel injectors to the bluff body trailing edge. Therefore, the resulting near-wake density ratio, ρ_b/ρ_u, is large (i.e., near unity), producing a large region of absolute instability locally, which ultimately leads to the alternate shedding of BVK vortices [21]. The fuel

transported to the far-wake burns in these large-scale, coherent structures, as illustrated in Figure 5.8a.

In contrast, when the fuel is introduced sufficiently far upstream of the reaction zone, it is likely that it is fully evaporated and well-mixed with the incoming air stream by the time it reaches the near-wake. Span-wise non-uniformities in the reaction zone are virtually non-existent, and greater amounts of fuel are entrained and burned in the near-wake shear layers than in close-coupled-fuelled flames. The resulting near-wake density ratio, ρ_b/ρ_u, is low due to the high local flame temperature, eliminating or reducing the size of absolutely unstable pockets in the near-wake, provided the combustor is operating away from blow off limits. The resulting reaction zone is characterized by two distinct, turbulent shear layers which spread downstream of the bluff body, as illustrated in Figure 5.8b. Measured data suggests, however, that the absolutely unstable region may become large enough so that asymmetric vortex shedding occurs if blow out limits are approached or the near-wake density ratio exceeds a critical value (i.e., if the flame temperature is low relative to the reactants temperature) [21, 34-36].

The experimental results and stability analysis described in this thesis have demonstrated that the near-wake combustion processes and the resulting density and velocity gradients ultimately control the onset and, in all likelihood, the amplitude of the BVK instability in reacting bluff body wakes. Regardless of the method of fuel injection, knowledge of these local flow properties is critical for predicting the hydrodynamic instability characteristics of bluff body-stabilized combustion processes. This is especially true when the fuel-air ratio distribution is spatially non-uniform, as the near-wake density ratios, ρ_b/ρ_u, can be sufficiently higher (i.e., closer to unity) than those typically observed in bluff body-stabilized combustion processes with premixed reactants, making such systems more susceptible to the BVK instability. In fact, this thesis demonstrated that non-uniform fuelling of the near-wake can result in absolute

instability at global operating conditions at which premixed flames are stable (i.e., the BVK instability is suppressed).

5.4.2 Limitations of the Linear Stability Analysis

The parallel, linear stability analysis originally described in [22] provides much insight into the influence of combustion process heat release upon the BVK instability. By modeling the combustion process as a discontinuity in temperature and velocity, the key mechanisms controlling the onset of absolute instability in reacting bluff body wakes were elucidated. However, several key assumptions were made in this analysis to interpret the measured data, and an improved understanding of the fundamental processes controlling the BVK instability in reacting wakes could be obtained by improving upon these generalizations.

First, the analysis could be improved by incorporating velocity and density profiles more relevant to reacting bluff body wakes. As pointed out in Section 5.3.2 and in [22], the boundary between convective and absolute instability shown in Figure 5.2 is an over-prediction of the actual critical density ratio, ρ^*_b/ρ^*_u, corresponding to transition for a given velocity ratio, U^*_b/U^*_∞. Consideration of more realistic velocity and density profiles would improve the accuracy of the predicted stability boundary. This, however, requires spatially-resolved measurements of velocity and gas density (or temperature) over a wide range of flow conditions (e.g., equivalence ratio, reactants temperature and pressure) for a given bluff body geometry. In addition, consideration of these "realistic" velocity and density profiles would likely require the use of numerical solutions in the stability analyses, as analytical solutions are unlikely. Such work is also outside the scope of this thesis, but should be investigated in future research.

Recall that, in computing the maximum absolute growth rates for each condition, the minimum U^*_b/U^*_∞ value and the axial location at which it occurred were assumed to remain nearly constant as operating conditions and fuel injection modes changed. The

assumption of constant minimum U^*_b/U^*_∞ is supported by velocity measurements reported in [35-36] and [56], but the precise value of this velocity ratio minimum most likely changed as operating conditions varied. In addition, the axial location at which the flow reversal was strongest likely varied somewhat as the length of the recirculation zone varied with varying density ratios, but it is believed to have always remained within the first two bluff body widths downstream (i.e., the region of integration for performing the density estimates). This is supported by the LES data in [53]. Regardless of the validity of the above assumptions, the accuracy of the stability analysis could be improved by measuring the velocity and density ratios at multiple axial locations in the near-wake for each operating condition, and by using the measured values as inputs to compute the absolute growth rates at each axial location. Such measurements and analysis should be performed in future studies.

While the transverse density and velocity gradients in the near-wake were identified as the key parameters controlling absolute instability in reacting bluff body wakes, additional insight may be obtained by considering certain terms which were neglected in the governing equations (see Equations 5.1-5.4). For example, the energy equation (5.3) does not contain a heat release term due to chemical reactions. Consideration of this and similar terms will undoubtedly make the analysis more complex, but it may yield more accurate predictions of absolute instability boundaries in reacting wakes. Therefore, such considerations should be made in future efforts.

Another aspect of the reacting flow experiments which was not considered in the stability analysis was the effect of confinement by the combustor walls on the wake stability. Previous studies have demonstrated that flow confinement can strongly influence the onset and amplitude of an absolutely unstable, BVK mode in wakes [57-58]. For example, Juniper extended the stability problem described in this chapter and found that confinement causes the transition from convective to absolute instability to occur at lower values of shear [58]. As a result, it is likely that the absolute growth rates

predicted in Section 5.3 would increase if the presence of confinement in the experiments was considered. Analyses similar to those described in [58] that consider velocity and density profiles pertinent to reacting wakes should be performed in future studies.

Finally, recall that three-dimensional variations in density and velocity, which likely occurred in the case of close-coupled fuel injection, were not considered in this analysis. Instead, estimates of span-wise and time-averaged recirculation zone gas temperature and velocity were used as inputs for this two-dimensional model. Stability analyses which consider variations of key parameters in all three spatial dimensions would, in all likelihood, improve the accuracy of the predicted instability characteristics, such as absolute growth rate, and should be developed.

In addition to span-wise variations in density and velocity, note that the transverse variations of these parameters may not be well represented by the vortex sheet model of Figure 5.1 in the case of close-coupled fuel injection. Since the stability analysis was two-dimensional, it was assumed that the density abruptly changed from that corresponding to unburned reactants to that of a mixture between products of combustion and unburned vitiated air entrained into the wake. That is, ρ_b was calculated based on the estimated amount of mixing between products and vitiated air in the recirculation zone. Since ρ_b was assumed constant on the products side of the flame sheet, it was assumed that mixing occurred infinitely fast. However, a more accurate representation of the transverse density profile may have to consider three characteristic densities: that of unburned reactants, followed by burned products, followed by a mixture of burned products and unburned vitiated air, as illustrated in Figure 5.9. If this third characteristic density were added, the density would actually increase slightly following its abrupt decrease due to combustion.

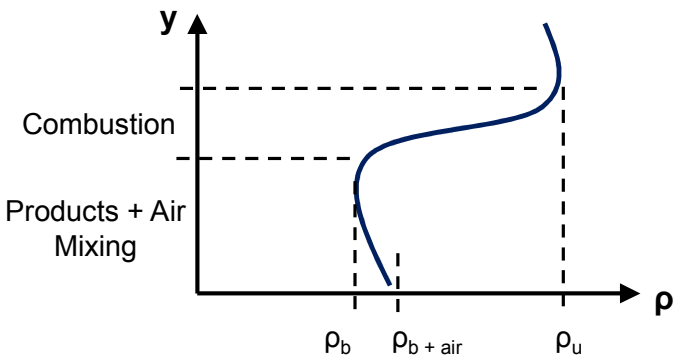

Figure 5.9: Hypothesized transverse density profile at a fixed axial and span-wise location in the near-wake for close-coupled-fuelled combustion.

Future analyses should consider adding a third gas stream based on the discussion above. Although such work is outside the scope of this study, it is important to clarify the influence of each density variation upon the wake instability characteristics. As described in [22], the change in linear instability characteristics from convective to absolute instability is brought about by changes in the interactions between the mixing layers via inertial terms. As the jump in momentum (i.e., ρU) between two gas streams increases, absolute instability becomes more likely. Thus, the jump in density and velocity which has the most dominant effect on the wake stability depends strongly upon the product of ρU. In light of this, it is anticipated that the initial jump in density from reactants to products across the flame (i.e., prior to mixing of products and air in the wake) has the strongest influence on the transition to absolute instability. This is because the density is decreasing by a factor of approximately two due to combustion, and since the combustion process is most likely occurring in the shear layers, the jump in velocity is also likely to be highest at this interface, going from positive to negative values.

However, the role of unburned vitiated air entrainment into the recirculation zone cannot be neglected. For example, note that close-coupled-fuelled flames with near-stoichiometric local equivalence ratios in the near-wake discrete reaction zones (which occurred at low Φ_{global}) experienced relatively strong heat release dynamics due to

absolutely unstable, BVK vortex shedding. If the wake were modeled to have three characteristic densities as described above, the initial jump in density across the flame would be quite high due to the high local flame temperature. Yet, Figure 4.15 shows that the BVK heat release dynamics were approximately 3% of the mean when the near-wake local equivalence ratio was unity. Contrasting this with the fact that BVK heat release dynamics were around 1% of the mean with upstream fuel injection at near-stoichiometric Φ_{global} values, it is apparent that the entrainment of vitiated air into the wake is strongly influencing the flame dynamics. Thus, the influence of reactants entrainment upon the wake stability cannot be neglected.

Although linear stability analyses can successfully predict the onset of instabilities, they are unable to predict their limit cycle amplitudes and frequencies. In Sections 4.4 and 5.4.1, it was postulated that near-wake density gradients control both the onset and saturation amplitude of the BVK instability in reacting bluff body wakes. While the linear stability analysis presented in this chapter confirmed the influence of this parameter upon the onset of instability, it provided no insight into the physical mechanisms controlling saturation amplitude, which is what was measured. Non-linear stability analyses which identify the dominant damping mechanisms and predict saturation should be developed. Such models have been successfully developed for isothermal wake flows (see, for example, [24]) and should be extended to reacting flows.

Other aspects of the experiments, such as free-stream turbulence and two-phase flow, are too complex for inclusion in the type of analyses described in this chapter. These require Direct Numerical Simulation (DNS) or LES to model. If successfully developed, such models would provide a key tool for the design of practical bluff body-stabilized combustion systems employing close-coupled fuel injection. The experimental results presented in this study should be used to guide the development of these and other predictive tools.

CHAPTER 6

CONCLUSION

This chapter summarizes the key findings of this study (Section 6.1), describes their contributions to the understanding of reacting bluff body flows (§6.2), and provides recommendations for future research (§6.3).

6.1 Summary of Key Findings

The primary objective of this study was to elucidate the influence of combustion process heat release upon Bénard-von Kármán (BVK) vortex shedding in reacting bluff body wakes. For this purpose, spatial and temporal heat release distributions were characterized for bluff body-stabilized combustion of liquid Jet-A fuel with high-temperature, vitiated air over a wide range of operating conditions. Two methods of fuel injection were investigated. In the first method, referred to as close-coupled fuel injection, the fuel was supplied via discrete liquid jets emanating 2.54 cm upstream of the bluff body trailing edge. The proximity of the fuel injectors to the reaction zone limited fuel-air mixing prior to burning, and the resulting fuel distribution in the reaction zone was spatially non-uniform, especially in the near-wake. The fuel was introduced well-upstream (~0.5m) of the bluff body in the second fuel injection mode, resulting in a well-mixed incoming reactants stream. The BVK heat release dynamics were compared between these fuel injection modes in order to investigate their dependence upon spatial fuel-air ratio and heat release distribution in the reacting wake.

When close-coupled fuel injection was used, the amplitude of BVK-associated heat release dynamics increased with increasing global equivalence ratio, reaching a maximum just before globally rich blow out of the combustion process occurred. This was due to a decrease in near-wake fuel entrainment as the fuel spray penetrated further

into the cross-flow, which reduced the local heat release and equivalence ratio (indicated by CH* and C_2*/CH* chemiluminescence, respectively). As a result, the density gradient across the near-wake reaction zone decreased, resulting in less damping of vorticity due to dilatation.

When the fuel was introduced upstream of the bluff body, the amplitude of the BVK heat release dynamics decreased significantly. These heat release fluctuations were strong near lean blow out ($\Phi \sim 0.31$) but were practically negligible for all other equivalence ratios ($0.5<\Phi<1.2$), only appearing intermittently in the time-resolved flame visualizations. This is in agreement with previous studies utilizing premixed reactants which found BVK-associated flame dynamics to be prominent only near lean blow out [13-15]. The weakening of the BVK heat release dynamics with increasing equivalence ratio was attributed to the near-wake density gradient becoming larger as the shear layer flame temperature increased.

The large disparity in dynamic heat release amplitudes between the two fuel injection modes was due to the differences in the spatial fuel-air ratio and heat release distributions. In general, close-coupled fuel injection resulted in significantly lower near-wake heat release than the "premixed" flames. The proximity of the fuel injectors to the reaction zone and the use of only two injectors on either side of the bluff body likely resulted in a "broken" reaction zone in the near-wake shear layers, allowing the entrainment of unburned reactants into the recirculation zone. This reduced the temperature of the recirculating gases, resulting in near-unity values of ρ_b/ρ_u in the near-wake. In contrast, when the fuel was introduced sufficiently far upstream of the bluff body, the fuel was likely fully evaporated and well-mixed with the air prior to burning, and the heat release was distributed more uniformly across the combustor span. This resulted in larger density gradients across the near-wake reaction zone than in the close-coupled fuel injection case, thereby reducing the intensity of BVK-associated heat release oscillations. High-speed visualizations of the combustion process suggested that

practically all of the fuel reaching the near-wake shear layers was consumed there in the case of upstream fuel injection, thus preventing unburned reactants from reaching the recirculation zone.

A parallel, linear stability analysis (originally described in [22]) was performed to further clarify the role of near-wake combustion heat release upon the stability of reacting bluff body wakes. In this analysis, the reaction zone was modeled as an infinitely thin discontinuity between reactant and product fluid streams, each with uniform density and velocity. Reacting wakes with low product-to-reactant density ratios, ρ_b/ρ_u, in the near-field (due to high local flame temperatures) were found to be convectively unstable. As the near-wake ρ_b/ρ_u increased (i.e., approached unity), a transition to an absolutely unstable wake occurred at a critical density ratio, the precise value of which depended upon the local velocity ratio between the burned and unburned gas streams. As the near-wake density ratio increased further, the absolute instability growth rate increased. This change in hydrodynamic instability characteristics (i.e., from convective to absolute instability) was likely brought about by changes in the interactions between the products and reactants streams via inertial terms [22]. As the momentum (i.e., ρU) of the products stream increased, absolute instability became more likely.

The stability analysis results were compared with measured oscillatory heat release spectra in order to investigate the connection between BVK-associated heat release dynamics and local absolute instability. Estimated values of near-wake density and velocity ratios (which were validated by companion LES computations) were used to predict absolute growth rates for a given equivalence ratio and fuel injection mode. For all operating conditions for which absolute instability was predicted, a coherent spike at the BVK frequency appeared in the flame spectra. This was the case for close-coupled fuel injection at all equivalence ratios and upstream fuel injection at lean equivalence ratios. However, two equivalence ratios with upstream fuel injection were predicted to be convectively unstable, but their dynamic heat release spectra revealed low-amplitude

BVK-associated oscillations. This apparent discrepancy was attributed to the fact that the simplified velocity and density profiles used in the stability analysis resulted in an under-prediction of the actual absolute growth rates (i.e., those which would have been calculated using density and velocity profiles typically observed in reacting bluff body wakes) [22]. It was also postulated that the unsteady nature of the reacting flow field caused intermittency between absolute and convective instabilities for these near-critical density ratios, as the predicted absolute growth rate based on time-averaged thermodynamic properties was near zero (see [36] for similar discussion). Upon viewing high-speed movies for these near-transition flow conditions, intermittency in flame dynamics between symmetric and asymmetric modes was, indeed, observed.

A third operating condition (T_{in}=675°C, Φ=1.1, upstream fuel injection) was predicted to be convectively unstable but with absolute growth rates much lower (i.e., more negative) than the cases described above (see Figure 5.7) due to its low ρ_b/ρ_u. Oscillatory heat release spectra at this flow condition revealed a complete suppression of the BVK instability, in agreement with the prediction that absolute instability was eliminated throughout the reacting wake. The results of this analysis support the postulate that sinuous heat release fluctuations due to BVK vortex shedding are the result of local absolute instability in the near-wake, which is eliminated only if the temperature rise across the reacting shear layers is sufficiently high.

6.2 Contributions of this Study

The results of this thesis improved the understanding of the causes of vortex shedding in reacting bluff body wakes. In particular, the influence of spatial distributions of fuel-air ratio and heat release upon the BVK instability was elucidated. It is concluded that the local combustion process heat release and resulting density gradients in the near-wake ultimately control the onset and amplitude of such oscillations in bluff body-

stabilized combustion processes. This is because absolute instability (a necessary condition for the global, BVK instability) can only occur at axial locations in which the centerline flow is reversed for exothermic reacting wakes, which is suppressed if the temperature rise across the reacting shear layers surrounding the recirculation zone is sufficiently large.

In light of this, the BVK instability is not likely to be prominent for premixed bluff body-stabilized combustion processes operating at conditions away from blow out. For example, premixed flames with relatively low temperature, near-stoichiometric reactants result in low products-to-reactants density ratios across the reacting shear layers, preventing local absolute instability throughout the near-wake. However, if blow out limits are approached or if the reactants temperature becomes too high, local absolute instability can occur in the near-wake due to the local products-to-reactants density ratios approaching unity, either intermittently (e.g., when localized extinction events occur near blow out) or for the entire period of operation (as is the case when T_u is high) [33-36]. If this region of absolute instability becomes sufficiently large, BVK vortex shedding commences [21-22].

On the other hand, bluff body-stabilized combustion processes with spatially varying fuel-air ratios (such as liquid-fuelled systems) can be particularly susceptible to the BVK instability. This is because the near-wake products-to-reactants density ratios can be much higher (i.e., closer to unity) than those encountered in premixed flames if the fuel is non-uniformly distributed throughout the reaction zone. As demonstrated in the close-coupled-fuelled experiments in this study, such systems can have locally lean combustion in the near-wake even though the global fuel-air ratio is near-stoichiometric or rich. This, along with the possible entrainment of unburned reactants into the recirculation zone, can create large pockets of absolute instability in the near-wake due to the near-unity values of ρ_b/ρ_u locally. The proximity of the fuel injectors to the reaction

zone in close-coupled-fuelled systems actually increases the likelihood of absolute instability and, thus, oscillatory heat release due to von Kármán vortex shedding.

Therefore, knowledge of the local thermal-fluid properties in the near-wake is critical for predicting the onset and intensity of the BVK instability in reacting bluff body wakes. In fact, global flow properties by themselves are insufficient for determining when and why such heat release oscillations occur. This was demonstrated by comparing two high-speed movies recorded at nearly-identical global operating conditions but with different fuel injection modes: one close-coupled and the other "premixed". Analysis of these movies showed that the close-coupled case was absolutely unstable (as indicated by the observed BVK heat release fluctuations) whereas the premixed case was convectively unstable (see Figure 5.6). This was due to the large difference in near-wake combustion processes between the two cases, as the close-coupled-fuelled system had locally lean combustion even though Φ_{global} for both cases was near unity. Thus, non-uniform fuelling can cause absolute instability to occur at global operating conditions in which premixed systems are convectively unstable.

Another key contribution of this work was an improved understanding of the fundamental processes controlling the static and dynamic stability of bluff body-stabilized combustors using close-coupled fuel injection. Measurements of spatial and temporal heat release and local equivalence ratio distributions were performed over a wide range of operating conditions using this method of fuel injection. The results demonstrated the profound impact the fuel spray penetration has upon the static and dynamic stability of the combustion process. It was demonstrated that the fuel entrainment and subsequent heat release in the near-wake decreased as a larger portion of the fuel spray penetrated further into the cross-flow. This eventually resulted in blow out of the combustion process as the local equivalence ratio in the near-wake became too lean. Heat release dynamics due to the BVK instability also grew in amplitude as the local equivalence ratio in the near-wake became leaner. Interestingly, the average local

equivalence ratio in the far-wake remained remarkably constant as the overall equivalence ratio (and, thus, the fuel jet penetration) was varied. It was estimated that combustion took place, on average, at stoichiometric conditions locally in this region. These results should be verified as they are critical for the development of practical combustors employing this method of fuel injection (e.g., aircraft engines), as well as computational tools which predict their performance.

6.3 Recommendations for Future Studies

The findings of this study have also pointed out the need for additional studies that would further improve the understanding of vortex shedding in reacting bluff body wakes. First, the interactions between coherent vortices shed from bluff bodies and the combustion process heat release need to be studied in more detail using planar visualization techniques, such as Particle Imaging Velocimetry (PIV) and Planar Laser Induced Fluorescence (PLIF). Such measurements would provide an improved understanding of the damping effects of exothermic reactions upon the formation and shedding of coherent structures. Planar velocity measurements would also allow the instantaneous flame stretch and vorticity in the reacting shear layers to be measured, which could determine the influence of these vortex-flame interactions upon blow out of the combustion process. Recall that the results of Lieuwen et al. [13] strongly suggest that coherent vortical structures shed from bluff bodies contribute to the blow out process.

In addition to heat release, the results of this study suggest that bluff body geometry (i.e., size and shape) and approach gas velocity have a considerable influence on BVK-associated flame dynamics. However, these effects were not investigated in detail, and additional work is needed to clarify their role in dynamic heat release due to vortex shedding. Related to this, the influence of base bleed upon the stability of reacting

bluff body wakes should be investigated, as previous research has demonstrated that it can eliminate absolute instability and suppress vortex shedding in non-reacting wakes [21].

Third, additional stability analyses are needed to improve understanding of the physical processes controlling the BVK instability in reacting bluff body wakes. The linear analysis presented in this thesis can be improved by incorporating the suggestions described in Section 5.4.2. In addition, non-linear stability analyses which identify the damping mechanisms and predict saturation amplitudes of BVK instabilities in reacting wakes are needed.

An important question brought up in Chapter 3 was whether or not oscillatory heat release due to absolutely unstable, BVK vortex shedding can participate in a feedback mechanism that drives combustion chamber acoustics. Unfortunately, this was outside the scope of this thesis, but it should be studied extensively, as any involvement in a thermo-acoustic instability mechanism could have detrimental effects on a bluff body-stabilized combustion system. Related to this, the response of BVK-associated flame dynamics to external acoustic forcing should be investigated.

Finally, additional work is needed to determine the fundamental processes controlling blow out in bluff body-stabilized flames using close-coupled fuel injection. The results of this study suggest that globally rich blow out is due to the near-wake reaction zone becoming too lean, as insufficient fuel is supplied to the near-wake shear layers to maintain stable combustion. This hypothesis needs to be investigated in more detail. While chemiluminescence imaging provided estimates of the near-wake local equivalence ratio near blow out (see Figure 4.12), these measurements only provided line-of-sight-integrated information, but could not provide insight into the span-wise variations in local equivalence ratio. Planar or point-wise measurements of local equivalence ratio should be performed in order to characterize such spatial variations and to validate the chemiluminescence measurement technique. These measurements could

also be used to validate the temperature estimations described in Chapter 4. In addition, LES computations should be performed to check the validity of the equivalence ratio distributions described in this thesis and to identify other factors contributing to blow out, such as flame stretch. Such measurements and computations would guide the development of practical bluff body combustors employing this method of fuel injection.

APPENDIX A

COMPARISON OF BROADBAND AND CH* FILTERED HIGH-SPEED IMAGING OF FLAME EMISSION

Chemiluminescence imaging is extensively used to characterize steady and unsteady heat release in combustion systems [39]. In order to accurately measure the concentration of these excited radicals in the reaction zone, care must be taken to eliminate light contributions from background sources. This becomes particularly challenging when the exposure time of the light measurement process is small, such as high-speed imaging of flame luminescence. Since these radicals emit light over narrow wavelength bands, typically on the order of 10-20 nm, low signal-to-noise ratios can occur when the measurements are band pass filtered and the exposure times are short. Such measurements typically require signal intensifiers in order to achieve acceptable signal-to-noise ratios.

High-speed movies of the flame emission were used in this study to characterize the heat release dynamics, with frame rates as high as 24 kHz and exposure times as low as 10 μs. However, the measurements were not band-pass filtered (although the red color signal was eliminated during post-processing of the movies), so the flame emission recorded by the camera contained a relatively wide range of wavelengths: 400-625 nm. In order to evaluate the accuracy of using these broadband flame emission measurements to characterize the heat release dynamics, high-speed movies were recorded with and without a CH* band-pass filter at nearly-identical operating conditions and compared to one another. The CH* filter used in these comparisons was centered at 430 nm and had a full width at half maximum intensity (FWHM) of 10 nm. Upon processing the unfiltered movie, the red color signal was eliminated, and the green and blue color signals were averaged to produce gray-scale images of the flame emission.

Image intensifiers were not used for these measurements, so it was necessary to operate the combustor at high fuel flow rates in order to achieve flame emission intensities high enough that the signal-to-noise ratio was acceptable for the band-pass filtered movies. Both movies were recorded with an inlet velocity of 225 m/s, Φ_{global}=0.90, and an inlet gas temperature of 843°C, which resulted in a highly unsteady reacting wake.

Flame dynamics time histories at each axial location were extracted from the movies using the method described in Section 2.2. Two-dimensional Discrete Fourier Transforms were then performed on these time histories to obtain the amplitudes and frequencies of the oscillatory combustion process heat release. Figure A.1 compares axial distributions of the BVK heat release dynamic amplitude between unfiltered and CH* filtered high-speed movies. Note that the oscillatory heat release amplitudes have been normalized by the maximum amplitude obtained for each movie, as the maximum light intensities recorded by each camera were much different. Figure A.1 demonstrates good agreement in the axial distribution of the BVK heat release dynamic amplitude. The relatively minor discrepancies between amplitude distributions are attributed primarily to the fact that the measurements were performed at two different time intervals for a highly unsteady flame. For both the unfiltered and the CH* filtered movies, the maximum intensity occurred at approximately 200 mm downstream of the bluff body trailing edge.

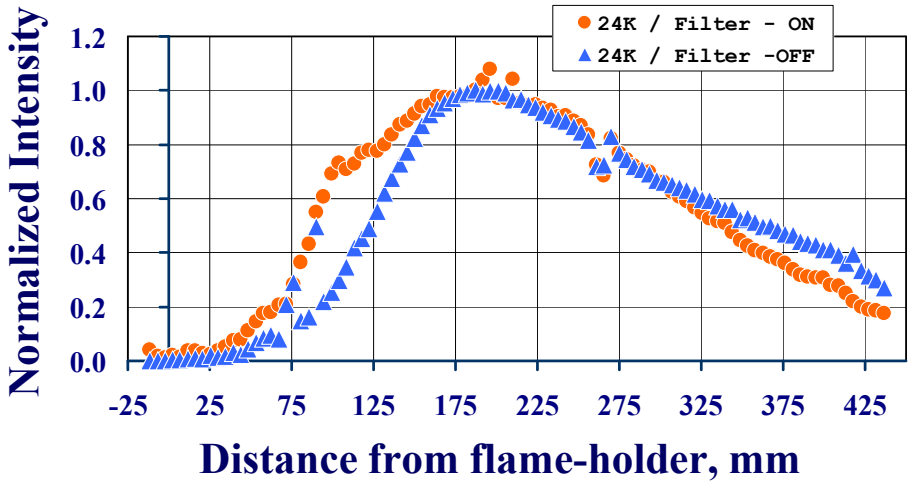

Figure A.1: Axial dependence of the BVK heat release dynamic amplitude, comparing unfiltered and CH* filtered movies (V_{in}=225 m/s, T_{in}=843°C, Φ_{global}=0.90).

The axial dependencies of the phase difference between oscillatory heat release measured by high-speed movies and that measured a photomultiplier tube (PMT) were also compared between band-pass filtered and unfiltered movies. The PMT recorded light at a fixed axial location of 229 mm downstream of the bluff body trailing edge during these measurements. Figure A.2 compares phase distributions between the CH* filtered and broadband movies, demonstrating excellent agreement beyond 50 mm downstream (approximately one bluff body width). The similarities in amplitude and phase distributions demonstrated in Figures A.1 and A.2, respectively, support the use of broadband flame emission measurements to characterize the BVK heat release dynamics in this study, as the lack of wavelength filtering does not appear to have affected the oscillatory heat release measurements considerably.

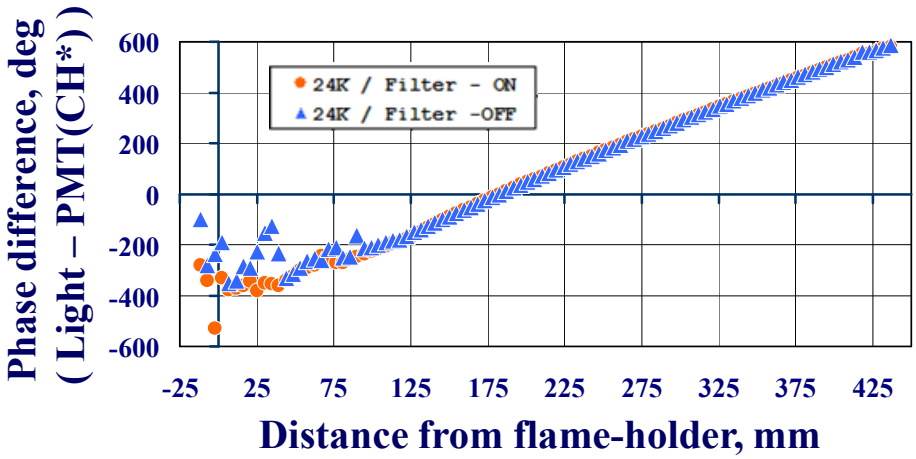

Figure A.2: Axial dependence of phase difference between flame dynamics recorded by high-speed camera and PMT, comparing CH* filtered and unfiltered movies (same operating conditions as Fig. A.1).

APPENDIX B

FLAME EDGE TRACKING

In addition to the two-dimensional Fourier analysis described in Section 2.2, the high-speed movies were also processed using flame edge tracking techniques. These methods use digital image processing techniques to define and track changes in the position of the reaction zone periphery in space and time.

For each frame in the movie sequence, the flame emission intensities recorded by the blue and green color channels of the high-speed camera were averaged to produce a gray-scale image of the flame emission. Next, the flame emission intensities for all pixels at a given axial location were normalized by the maximum intensity occurring along that cross-section. The resulting flame emission intensity varied between zero and unity in the transverse direction at all axial locations. The instantaneous flame edges, $\zeta(x,t)$, were then defined as the outermost transverse locations in which the flame emission intensity crossed a predefined threshold value. This was done by converting the normalized flame image into a binary image in which all pixels with intensity less than the threshold were set to zero, and all pixels with intensity greater than or equal to the threshold were set to unity. The upper and lower flame edges were then respectively defined as the top and bottom interfaces between zero and unity.

This procedure is illustrated in Figure B.1, which compares a gray-scale image extracted from a high-speed movie (Figure B.1a) to its binary conversion using a threshold value of 0.20 (Figure B.1b). The position of the bluff body is superimposed onto the binary image of Figure B.1b, indicated by the gray rectangle on the left. For each binary image obtained from the movie sequence, the upper and lower most points in which the pixel intensity equaled unity at each axial location were recorded. These points were then averaged in time to produce the steady-state upper and lower flame edge

positions, represented by $\bar{\zeta}_U(x)$ and $\bar{\zeta}_L(x)$, respectively, in Figure B.1b (indicated by the red lines). The transverse deviations of the instantaneous flame edges from their steady-state values in space and time were then recorded. These are defined as $\zeta_U(x,t)$ and $\zeta_L(x,t)$ for the upper and lower flame edges, respectively, in Figure B.1b.

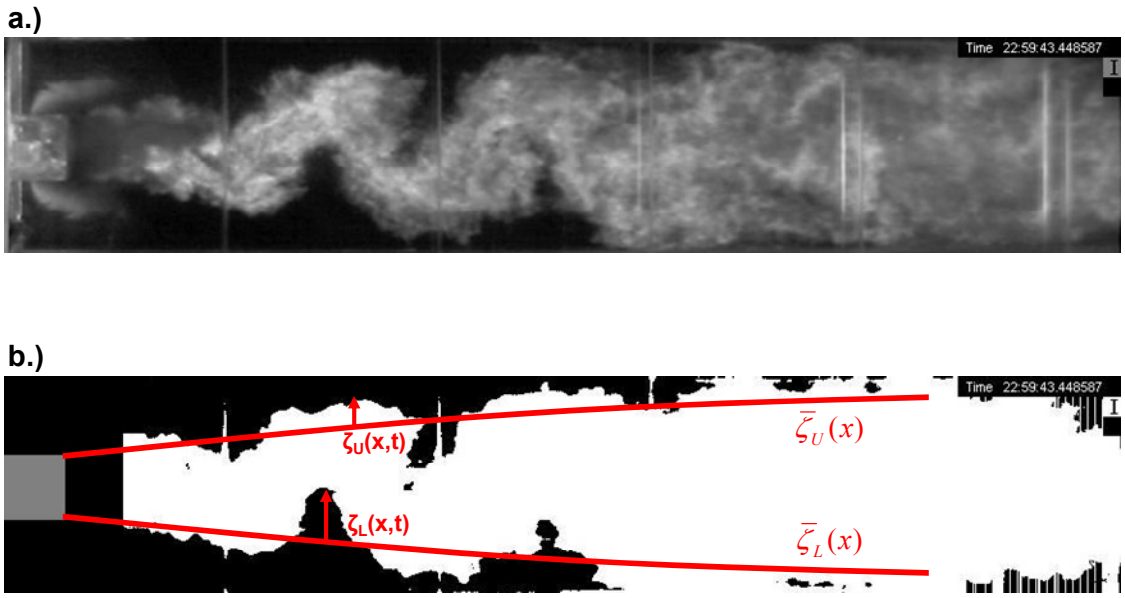

Figure B.1: a.) Gray-scale image of flame emission intensity extracted from a high-speed movie.
b.) Binary image of flame emission intensity after applying a threshold intensity value of 0.20 times the maximum intensity at each axial location. Definitions of the instantaneous flame edge deviation from the mean are given by $\zeta_U(x,t)$ and $\zeta_L(x,t)$.

The time series of $\zeta_U(x,t)$ and $\zeta_L(x,t)$ were then Fourier transformed to produce their temporal spectra for a given axial location. Examples of these spectra are shown in Figure B.2, comparing flame dynamics for close-coupled (left) and upstream (right) fuel injection at nearly-identical global operating conditions. For comparison, these spectra correspond to the same operating conditions shown previously in Figure 3.10, although the axial locations at which they were obtained are different. Figure B.2 shows that high-amplitude BVK flame dynamics (f=961 Hz) occurred at Φ_{global}=0.60 when close-coupled

fuel injection was used, with spectral amplitudes as high as 0.24 cm from the mean flame edge position. In contrast, relatively weak BVK flame dynamics are shown in the spectra corresponding to upstream fuel injection at Φ_{global}=0.61, with flame edge dynamic spectral amplitudes remaining below 0.1 cm at the BVK frequency (f=1043 Hz). These trends are in agreement with Figure 3.10, which showed the BVK heat release dynamics resulting from close-coupled fuel injection to be 3.5 times higher in amplitude than those resulting from upstream fuel injection.

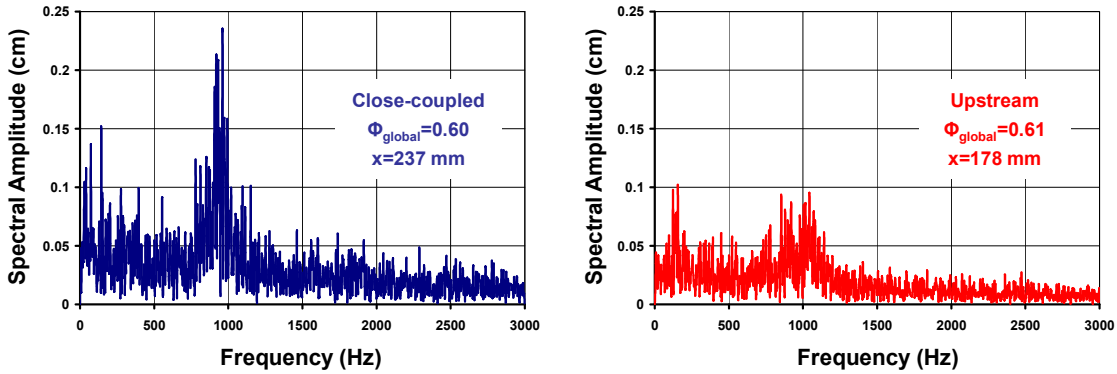

Figure B.2: Flame edge dynamic spectra for close-coupled (left) and upstream (right) fuel injection at Φ_{global}~0.60 (same operating conditions as Figure 3.10).

Similar spectra were obtained for each axial location in the combustor. The maximum BVK spectral amplitude over all axial locations was then defined as the overall BVK flame dynamics intensity for each operating condition. Examples of these maxima are plotted in Figure B.3, which describes their dependence upon global equivalence ratio and fuel injection mode, comparing upstream and close-coupled fuel injection. From the figure, it can be seen that the BVK flame dynamics were significantly higher in amplitude for close-coupled fuel injection than upstream fuel injection for all but the leanest global equivalence ratio, as was previously demonstrated in Figure 3.11, which plots the BVK heat release dynamic intensities at the same operating conditions using

two-dimensional Fourier analysis. What is of greater interest, however, is that the trends shown in Figure B.3 bear striking resemblance to those shown in Figure 3.11. These similarities indicate that the fluctuations in heat release due to BVK vortex shedding were primarily due to fluctuations in flame edge position as the coherent structures interacted with the flame sheets. The transversely integrated heat release fluctuations quantified using two-dimensional Fourier analyses appear to be dominated by such flame edge fluctuations, based on its similarity to the results obtained using edge tracking techniques.

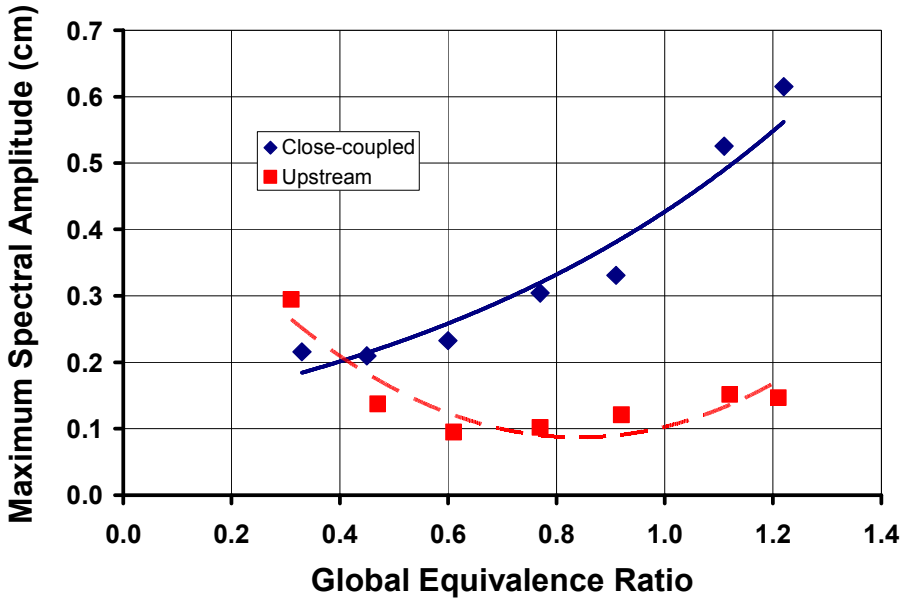

Figure B.3: Axial maxima of BVK flame dynamic amplitude vs. global equivalence ratio, comparing close-coupled and upstream fuel injection modes (same operating conditions as Figure 3.11).

APPENDIX C

EXTENDED DERIVATION OF DISPERSION RELATION

This Appendix provides a more detailed derivation of the dispersion relation describing the stability of a heated wake bounded by two vortex sheets (i.e., Equation 5.26). It is intended to be a supplement to Chapter 5. That is, equations which appear in Chapter 5 are not repeated here. Instead, several intermediate steps which were omitted in the derivation of Section 5.2 are described here to provide a more complete explanation of how the linearized disturbance equations (Equations 5.5-9) reduce to the single analytical dispersion relation describing the stability of the flow.

In Section 5.2 the linearized disturbance equations of motion (Equations 5.5-9) were formulated. Expanding each unsteady variable as a normal mode of the form given in Equation 5.14 led to a system of five differential equations describing the stability of the flow (see Equations 5.16-20). If viscosity and thermal conductivity are neglected, this system of equations simplifies to the following:

$$\frac{\hat{\rho}}{\overline{\rho}}\left(\overline{u}-c\right)+\hat{u}=\frac{i}{k}\left[\frac{d\hat{v}}{dy}+\frac{\hat{v}}{\overline{\rho}}\frac{\partial\overline{\rho}}{\partial y}\right] \tag{C.1}$$

$$\overline{\rho}\hat{u}(\overline{u}-c)=-\hat{p}+\frac{i\overline{\rho}\overline{u}_y\hat{v}}{k} \tag{C.2}$$

$$\hat{v}=\frac{i}{k}\frac{d\hat{p}}{dy}\frac{1}{\overline{\rho}(\overline{u}-c)} \tag{C.3}$$

$$\hat{T}(\overline{u}-c)ik=-\overline{T}_y\hat{v} \tag{C.4}$$

$$-\hat{\rho}\overline{T}^2=\hat{T} \tag{C.5}$$

Substituting Equation C.5 into Equation C.4 results in the following expression:

$$-\hat{\rho}(\overline{u}-c)ik=\hat{v}\frac{d\overline{\rho}}{dy} \tag{C.6}$$

Similarly, Equation C.3 can be substituted into Equations C.2 and C.6 in order to eliminate $\hat{v}$ from the system of equations (C.1-C.5). This yields the following two equations:

$$\hat{u}=\frac{-1}{\overline{\rho}(\overline{u}-c)}\left[\hat{p}+\frac{\overline{u}_y}{k^2(\overline{u}-c)}\frac{d\hat{p}}{dy}\right] \tag{C.7}$$

$$\hat{\rho}=\frac{-\overline{\rho}_y\hat{p}_y}{k^2\overline{\rho}(\overline{u}-c)^2} \tag{C.8}$$

Equations C.3, C.7 and C.8 contain explicit relationships for $\hat{v}$, $\hat{u}$ and $\hat{\rho}$, respectively. These equations can be used to eliminate these three variables from Equation C.1. Making these substitutions results in the following expression:

$$\frac{\overline{\rho}_y\hat{p}_y}{k^2\overline{\rho}^2(\overline{u}-c)}+\frac{1}{\overline{\rho}(\overline{u}-c)}\left[\hat{p}+\frac{\overline{u}_y\hat{p}_y}{k^2(\overline{u}-c)}\right]=\frac{1}{k^2}\left[\frac{d}{dy}\left(\frac{\hat{p}_y}{\overline{\rho}(\overline{u}-c)}\right)+\frac{\hat{p}_y}{\overline{\rho}^2(\overline{u}-c)}\frac{d\overline{\rho}}{dy}\right] \tag{C.9}$$

Upon expanding the first derivative on the right-hand-side of Equation C.9, this equation can be simplified to a second order differential equation for the disturbance pressure amplitude, $\hat{p}$. This equation appears as Equation 5.21 in Section 5.2, with the boundary conditions given in Equation 5.22. The vortex sheet model illustrated in Figure 5.1 allows Equation 5.21 to be simplified even further, since $\overline{u}_y$ and $\overline{\rho}_y$ are equal to zero on either side of the vortex/flame sheet. In this case, Equation 5.21 reduces to:

$$\frac{d^2\hat{p}}{dy^2}-k^2\hat{p}=0 \tag{C.10}$$

Solving this differential equation and applying the appropriate boundary conditions (see Equation 5.22) for each fluid stream (i.e., products and reactants), it can be seen that the disturbance pressures for each stream take on the form:

$$\hat{p}_{\infty}(y) = C_{\infty} \exp(-ky) \tag{C.11}$$

$$\hat{p}_{b}(y) = C_{b} \left[\exp(ky) - \exp(-ky) \right] \tag{C.12}$$

where C_{∞} and C_b are arbitrary constants.

In order to arrive at the dispersion relation (Equation 5.26), perturbation pressure and transverse displacement must be matched at the interface of the two fluid streams [22, 55]. For this purpose, an unsteady velocity potential is defined for each gas stream of the form:

$$\phi = \bar{\phi} + \phi' \tag{C.13}$$

If ϕ' is assumed to take on the same form as $p`$ (see Equations 5.14, C.11 and C.12), then the unsteady potential functions for each stream are given by Equations 5.23.

The transverse displacement of each gas stream at the interface is given by Equation 5.24. The constants C_{∞} and C_b can be solved for by substituting Equations 5.23 for the velocity potential into Equation 5.24. Making these substitutions, it can be seen that:

$$C_{\infty} = \frac{i\hat{h}(c - \bar{u}_{\infty})}{e^{-ky}} \tag{C.14}$$

$$C_{b} = \frac{i\hat{h}(\bar{u}_{b} - c)}{\left(e^{ky} + e^{-ky}\right)} \tag{C.15}$$

In order to match the perturbation pressures at the interface, the unsteady velocity potentials (Equations 5.23) must be substituted into the unsteady Bernoulli equation (Equation 5.25) for each gas stream. If each unsteady variable in Equation 5.25 is expanded according to Equation 5.14 and squares of perturbation terms are neglected, the following relationship between the unsteady pressure and velocity potential results:

$$p'_{j} = \bar{\rho}_{j} \left(i\omega\phi'_{j} - \bar{u}_{j} ik\phi'_{j} \right) \tag{C.16}$$

where the subscript "j" in this case represents the fluid stream under consideration, i.e., products or reactants.

Substituting Equations 5.23, C.14 and C.15 for the velocity potential terms in Equation C.16 results in the following expressions for the perturbation pressures of each gas stream:

$$p'_b = \bar{\rho}_b \left[\frac{i\hat{h}\left(\bar{u}_b - c\right)\left(e^{ky} - e^{-ky}\right)e^{ik(x-ct)}\left(i\omega - \bar{u}_b ik\right)}{\left(e^{ky} + e^{-ky}\right)} \right] \tag{C.17}$$

$$p'_\infty = \bar{\rho}_\infty \left[\frac{i\hat{h}\left(c - \bar{u}_\infty\right)e^{-ky}e^{ik(x-ct)}\left(i\omega - \bar{u}_\infty ik\right)}{e^{-ky}} \right] \tag{C.18}$$

Upon equating Equations C.17 and C.18 and setting y=1 (i.e., matching perturbation pressures at the interface, y=1), it can be shown that:

$$S\frac{\left(\bar{u}_b - c\right)^2}{\left(\bar{u}_\infty - c\right)^2} = -\frac{\left(e^k + e^{-k}\right)}{\left(e^k - e^{-k}\right)} \tag{C.19}$$

where S is defined in Equation 5.27. Finally, note that:

$$\bar{u}_b = \frac{\bar{u}_b^*}{0.5(\bar{u}_b^* + \bar{u}_\infty^*)} = \frac{(\bar{u}_b^* - \bar{u}_\infty^*) + (\bar{u}_b^* + \bar{u}_\infty^*)}{(\bar{u}_b^* + \bar{u}_\infty^*)} \equiv 1 + \Lambda \tag{C.20}$$

$$\bar{u}_\infty = \frac{\bar{u}_\infty^*}{0.5(\bar{u}_b^* + \bar{u}_\infty^*)} = \frac{(\bar{u}_b^* + \bar{u}_\infty^*) - (\bar{u}_b^* - \bar{u}_\infty^*)}{(\bar{u}_b^* + \bar{u}_\infty^*)} \equiv 1 - \Lambda \tag{C.21}$$

where asterisks denote a dimensional velocity and Λ is defined in Equation 5.28. Substituting Equations C.20 and C.21 into C.19 results in the dispersion relation listed as Equation 5.26, which describes the stability of the heated, double vortex sheet wake.

REFERENCES

[1] Zukoski, E. E., and Marble, F. E., "The Role of Wake Transition in the Process of Flame Stabilization on Bluff Bodies," *Combustion Researches and Reviews*, 1955, pp. 167-180.

[2] Zukoski, E. E., and Marble, F. E., "Experiments Concerning the Mechanism of Flame Blowoff from Bluff Bodies," *Proceedings of the Gas Dynamics Symposium on Thermochemistry*, Northwestern University, Evanston IL, 1956, pp. 205-210.

[3] DeZubay, E. A., "Characteristics of Disk-Controlled Flames," *Aero Digest*, **61**, No. 1, July 1950, pp. 54-56.

[4] King, C., "A Semi-empirical Correlation of Afterburner Combustion Efficiency and Lean Blow Out Fuel-air Ratio Data with Several Afterburner Inlet Variables," NACA Report RM E57F26.

[5] Longwell, J., Chenevey, J., Clark, W., and Frost, E., "Flame Stabilization by Baffles in a High Velocity Gas Stream," *Third Symposium on Combustion and Flame and Explosion Phenomena*, p. 40-44, 1949.

[6] Ducruix, S., Schuller, T., Durox, D. and Candel, S., "Combustion Instability Mechanisms in Premixed Combustors," in *Combustion Instabilities in Gas Turbine Engines: Operational Experience, Fundamental Mechanisms and Modeling*, edited by T. Lieuwen and V. Yang, AIAA Progress in Astronautics and Aeronautics, Vol. 210, 2005, pp. 179-212.

[7] Schadow, K. and Gutmark, E., "Combustion Instability related to Vortex Shedding in Dump Combustors and their Passive Control," *Progress in Energy and Combustion Science*, **18**, pp. 117-132.

[8] Hegde, U., Reuter, D., Zinn, B.T. and Daniel, B., "Fluid Mechanically Coupled Combustion Instabilities in Ramjet Combustors," *25th AIAA Aerospace Sciences Meeting*, Reno, Nevada, AIAA Paper No. 87-0216, (1987).

[9] Smith, D. and Zukoski, E., "Combustion Instability sustained by Unsteady Vortex Combustion," *21st Joint Propulsion Conference and Exhibit*, 1985, AIAA Paper 85-1248.

[10] Zinn, B.T. and Lieuwen, T., "Combustion Instabilities: Basic Concepts", in *Combustion Instabilities in Gas Turbine Engines: Operational Experience, Fundamental Mechanisms and Modeling*, edited by T. Lieuwen and V. Yang, AIAA Progress in Astronautics and Aeronautics, Vol. 210, 2005, pp. 3-26.

[11] Coats, C., "Coherent Structures in Combustion," *Progress in Energy and Combustion Science*, **22**, pp. 427-509, 1996.

[12] Shanbhogue, S., Husain, S., and Lieuwen, T., "Lean blowoff of bluff body-stabilized flames: Scaling and dynamics," Progress in Energy and Combustion Science, **35**, pp. 98-120, 2009.

[13] Lieuwen, T., Shanbhogue, S., Khosla, S. and Smith, C., "Dynamics of Bluff Body Flames near Blowoff," *45th AIAA Aerospace Sciences Meeting and Exhibit*, 2007, Reno, Nevada, AIAA Paper No. 2007-0169.

[14] Nair, S., "Acoustic Characterization of Flame Blowout Phenomenon", Ph.D. Thesis, Georgia Institute of Technology, 2006.

[15] Kiel, B., Garwick, K., Lynch, A., Gord, J. R. and Meyer, T., "Non-Reacting and Combusting Flow Investigation of Bluff Bodies in Cross Flow", *42nd AIAA/ASME/SAE/ASEE Joint Propulsion Conference and Exhibit*, Sacramento, California, AIAA Paper #2006-5234.

[16] Perry, A., Chong, M. and Lim, T., "The vortex-shedding process behind two-dimensional bluff bodies," *Journal of Fluid Mechanics*, **116**, pp. 77-90, 1982.

[17] Gerrard, J., "The mechanics of the formation region of vortices behind bluff bodies," *Journal of Fluid Mechanics*, **25**, Part 2, pp. 401-413, 1966.

[18] Strykowski, P.J. and Sreenivasan, K., "On the Formation and Suppression of Vortex 'Shedding ' at low Reynolds Numbers," *Journal of Fluid Mechanics*, **218**, pp. 71-107, 1990.

[19] Lecordier, J., Browne, L., Masson, S., Dumouchel, F. and Paranthoën, P., "Control of Vortex Shedding by Thermal Effect at Low Reynolds Numbers," *Experimental Thermal and Fluid Science*, **21**, pp. 227-237, 2000.

[20] Bearman, P., "Investigation of the Flow behind a Two-dimensional Model with a Blunt Trailing Edge and Fitted with Splitter Plates," *Journal of Fluid Mechanics*, **21**, pp. 241-255, 1965.

[21] Huerre, P. and Monkewitz, P., "Local and Global Instabilities in Spatially Developing Flows," *Annual Review of Fluid Mechanics*, **22**, pp. 473-537, 1990.

[22] Yu, M. and Monkewitz, P., "The Effect of Nonuniform Density on the Absolute Instability of Two-dimensional Inertial Jets and Wakes," *Physics of Fluids*, A, Vol. 2, Issue 7, 1990.

[23] Huerre, P. and Rossi, M. "Hydrodynamic Instabilities in Open Flows," in *Hydrodynamics and Nonlinear Instabilities*, edited by C. Godréche and P. Manneville, Cambridge University Press, 1998, pp. 81-294.

[24] Provansal, M., Mathis, C. and Boyer, L., "Bénard-von Kármán Instability: Transient and Forced Regimes," *Journal of Fluid Mechanics*, **182**, pp. 1-22, 1987.

[25] Williamson, C., "Vortex Dynamics in the Cylinder Wake," *Annual Review of Fluid Mechanics*, **28**, pp. 477-539, 1996.

[26] Fujii, S. and Eguchi, K., "A Comparison of Cold and Reacting Flows around a Bluff Body Flame Stabilizer," *ASME Journal of Fluids Engineering*, **103**, pp. 328-334, 1981.

[27] Bill, R. and Tarabanis, K., "The Effect of Premixed Combustion on the Recirculation Zone of Circular Cylinders," *Combustion Science and Technology*, **47**, pp. 39-53, 1986.

[28] Zukoski, E., "Flame Stabilization on Bluff Bodies at Low and Intermediate Reynolds Numbers," Ph.D. Thesis, California Institute of Technology, 1954.

[29] Nair, S. and Lieuwen, T., "Near-Blowoff Dynamics of a Bluff-body Stabilized Flame," *Journal of Propulsion and Power*, **23**, pp. 421-427.

[30] Mehta, P.G., and Soteriou, M.C., "Combustion heat release effects on the dynamics of bluff body stabilized premixed reacting flows," *41st Aerospace Sciences Meeting and Exhibit*, Reno, Nevada, AIAA Paper # 2003-0835.

[31] Thurston, D. "An Experimental Investigation of Flame Spreading from Bluff Body Flameholders," Thesis, California Institute of Technology, 1958.

[32] Hertzberg, J. R., Shepherd, I. G., and Talbot, L., "Vortex Shedding Behind Rod Stabilized Flames," *Combustion and Flame*, **86**, 1991, pp. 1-11.

[33] Anderson, K., Hertzberg, J. and Mahalingam, S., "Classification of Absolute and Convective Instabilities in Premixed Bluff Body Stabilized Flames," *Combustion Science and Technology*, **112**, pp. 257-269, 1996.

[34] Erickson, R.R., Soteriou, M.C. and Mehta, P.G., "The Influence of Temperature Ratio on the Dynamics of Bluff Body Stabilized Flames," *44th Aerospace Sciences Meeting and Exhibit*, Reno, Nevada, AIAA Paper #2006-753.

[35] Emerson, B., Lundrigan, J., O'Connor, J., Noble, D. and Lieuwen, T., "Dependence of the Bluff Body Wake Structure on Flame Temperature Ratio," *49th Aerospace Sciences Meeting*, Orlando, Florida, AIAA Paper #2011-597.

[36] Emerson, B., Lundrigan, J., O'Connor, J., Noble, D. and Lieuwen, T., "Convective and Absolute Instabilities in Reacting Bluff Body Wakes," *Proceedings of ASME Turbo Expo 2011*, Vancouver, Canada, ASME paper GT2011-45330.

[37] Lovett, J., Brogan, T., Philippona, D., Keil, B., Thompson T., "Development Needs for Advanced Afterburner Designs," *40th AIAA/ASME/SAE/ASEE Joint Propulsion Conference and Exhibit*, 2004. AIAA Paper No. 2004-4192.

[38] Lovett, J., Cross, C., Lubarsky, E. and Zinn, B. T., "Mechanisms Controlling Bluff Body-stabilized Flames with Closely-Coupled Fuel Injection," *Proceedings of ASME Turbo Expo 2011*, Vancouver, Canada, ASME paper GT2011-46676.

[39] Lee, J.G. and Santavicca, D.A., "Experimental Diagnostics for the Study of Combustion Instabilities in Lean Premixed Combustors," *Journal of Propulsion and Power*, **19** (5) p.735-750.

[40] Morrell, R., Seitzman, J., Wilensky, M., Lee, J., Lubarsky, E., and Zinn, B., "Interpretation of Optical Flame Emissions for Sensors in Liquid-Fueled Combustion," *39th AIAA Aerospace Sciences Meeting and Exhibit*, Reno, Nevada, January 2001, AIAA Paper 2001-0787.

[41] Najm, H., Paul, P., Mueller, C., and Wyckoff, P., "On the Adequacy of Certain Experimental Observables as Measurements of Flame Burning Rate," *Combustion and Flame*, v. **113**, pp.312-332, 1998.

[42] Nori, V., "Modeling and Analysis of Chemiluminescence Sensing for Syngas, Methane and Jet-A Combustion," Ph.D. Thesis, Georgia Institute of Technology, 2008.

[43] Clark, T. and Bittker, D., "A study of the Radiation from Laminar and Turbulent Open Propane-air Flames as a Function of Flame Area, Equivalence Ratio, and Fuel Flow Rate," NACA RM E54F29, 1954.

[44] Muruganandam, T., Kim, B, Morrell, M., Nori, V., Patel, M., Romig, B., Seitzman, J., "Optical equivalence ratio sensors for gas turbine combustors," *Proceedings of the Combustion Institute*, **30**, pp. 1601-1609, 2005.

[45] Cross, C., Lubarsky, E., Shcherbik, D., Bonner, K., Klusmeyer, A., Zinn, B.T. and Lovett, J., "Determination of Equivalence Ratio and Oscillatory Heat Release Distributions in Non-premixed Bluff Body-stabilized Flames using Chemiluminescence Imaging," *Proceedings of ASME Turbo Expo 2011*, Vancouver, Canada, ASME paper GT2011-45579.

[46] Shanbhogue, S. "Dynamics of Perturbed Exothermic Bluff-Body Flow-Fields," Ph.D. Thesis, Georgia Institute of Technology, 2008.

[47] Becker, J. and Hassa, C., "Breakup and Atomization of a Kerosene Jet in Crossflow at Elevated Pressure," *Atomization and Sprays*, **11**, pp. 49-67, 2002.

[48] Fureby, C., "A Computational Study of Combustion Instabilities due to Vortex Shedding," *Proceedings of the Combustion Institute*, **28**, pp. 783-791, 2000.

[49] Roby, R. J., Reaney, J .E. and Johnsson, E. L., "Detection of Temperature and Equivalence Ratio in Turbulent Premixed Flames Using Chemiluminescence," *Proceedings of the 1998 Int. Joint Power Generation Conference*, **Vol. 1**, 1998, 593-602.

[50] Turns, S., *An Introduction to Combustion*, McGraw-Hill, 2000.

[51] Porumbel, I., "Large Eddy Simulation of Bluff Body Stabilized Premixed and Partially Premixed Combustion," Ph.D. Thesis, Georgia Institute of Technology, 2006.

[52] Ahlborn, B., Lefrancois, B., King, D., "The Clockwork of Vortex Shedding," *Physics Essays*, **11**, Number 1, 1998.

[53] Smith, A. and Menon, S., private communication

[54] Batchelor, G. K., *An Introduction to Fluid Dynamics*, 1st Edition, Cambridge University Press, 1967.

[55] Lord Rayleigh, *The Theory of Sound*, Volume II, 2nd Edition (Revised), Dover, New York, 1945.

[56] Beer, J. M., and Chigier, N.A., *Combustion Aerodynamics*, Fuel and Energy Science Series, Elsevier Science Ltd., 1972.

[57] Shair, F., Grove, A., Petersen, E., and Acrivos, A., "The effect of confining walls on the stability of the steady wake behind a circular cylinder," *Journal of Fluid Mechanics*, **17**, pp. 546-550, 1963.

[58] Juniper, M., "The effect of confinement on the stability of two-dimensional shear flows," *Journal of Fluid Mechanics*, **565**, pp. 171-195, 2006.